

**Development of direct joining process of metals and
polymers via additively fabricated anchor layer by
laser induced in-situ reaction**

2020

Kim Seung-Gwang

Contents

1. Background	6
1.1. Multi-material structure	6
1.2. Characteristics of metal/polymer direct joining	8
1.2.1. <i>Surface wetting</i>	8
1.2.2. <i>Chemical bond</i>	9
1.2.3. <i>Mechanical interlocking</i>	11
1.2.4. <i>Stress singularity</i>	11
1.3. Metal/polymer direct joining through mechanical interlocking	12
1.3.1. <i>Metal surface modifying process</i>	13
1.3.2. <i>Joining processes and metal/polymer joint characteristics</i>	14
1.4. Metal/polymer direct joining via an additively manufactured anchor layer	17
1.5. Purpose of this research	18
References	19
2. Effects of surface treatments on the wettability of metal surface	23
2.1. Introduction	23
2.2. Experimental method	23
2.3. Results	25
2.3.1. <i>Change in the contact angle</i>	25
2.3.2. <i>Change in surface conditions</i>	26
2.4. Discussion	28
2.5. Summary	29
References	30
3. Manufacturing process of an anchor layer through laser-induced in-situ reaction for joining Al alloy and PA6 substrates.	31
3.1. Introduction	31
3.2. Experimental methods	31

3.3. Results	34
3.3.1. <i>Characterization of the anchor layer</i>	34
3.3.2. <i>Characteristics of Al/PA6 lap joints</i>	37
3.4. Discussion	40
3.4.1. <i>Characterization of anchor layer</i>	40
3.4.2. <i>Mechanical behaviors of Al/PA6 lap joints</i>	40
3.5. Summary	42
References	42
4. Influence of joining thermal history during hot-pressing on the mechanical behaviors of the Al/PA6 lap joints	44
4.1. Introduction	44
4.2. Experimental methods	44
4.2.1. <i>Al/PA6 lap joint fabrication by hot-pressing</i>	44
4.2.2. <i>Mechanical behaviors of Al/PA6 lap joint</i>	46
4.2.3. <i>Change in PA6 characteristics</i>	46
4.3. Results	47
4.3.1. <i>Mechanical behaviors of Al/PA6 lap joints</i>	47
4.3.2. <i>Change in the PA6 characteristics</i>	49
4.4. Discussion	51
4.5. Summary	54
References	55
5. Effect of the molar ratio of C powder in Al-Ti-C powder blend on the structure and microstructure of the anchor layer for joining an Al alloy and Polyamide-6	56
5.1. Introduction	56
5.2. Experimental methods	56
5.3. Results	58
5.3.1. <i>Characterization of the anchor layers</i>	58
5.3.2. <i>Mechanical properties of Al/PA6 lap joints</i>	64

5.4. Discussion	66
5.4.1. <i>Morphology and microstructure of the anchor layer</i>	66
5.4.2. <i>Mechanical behaviors of Al/PA6 joint via the anchor layer</i>	69
5.5. Summary	71
Reference	71
6. Structural control of anchor layer by changing laser conditions for enhancing Al/PA6 lap joint strength	72
6.1. Introduction	72
6.2. Experimental methods	72
6.3. Results	76
6.3.1. <i>Characteristics of the anchor layers</i>	76
6.3.2. <i>Mechanical behaviors of Al/PA6 lap joints</i>	80
6.4. Discussion	82
6.4.1. <i>Characteristics of the anchor layers</i>	82
6.4.2. <i>Mechanical behaviors of Al/PA6 lap joints</i>	84
6.5. Summary	86
References	86
7. Summary	87
References	90
Appendix A. Preliminary experiments for producing the anchor layer on Al substrate	92
Appendix B. Non-equilibrium solidification – Scheil solidification	107
【Articles related to this research and related chapters】	111
【Acknowledgements】	112

1. Background

1.1. Multi-material structure

Carbon dioxide (CO₂) gas is one of the main green-house gases that causes global warming around the world. Automobiles are responsible for about 12% of CO₂ emission in entire EU CO₂ emission [1.1]. The fuel efficiency of vehicles must be improved to reduce the CO₂ emission. **Figure 1.1** shows actual fuel efficiency in US reported in 2019 and future fuel efficiency targets of key vehicle markets [1.2, 1.3]. EU, China, Canada and US are planning to increase the fuel efficiency around 2~3 km/l from 2020 to 2025. US needs rapid increase in a fuel efficiency to achieve the target of 17 km/l in 2020 because the actual fuel efficiency in 2019 of US was about 11 km/l.

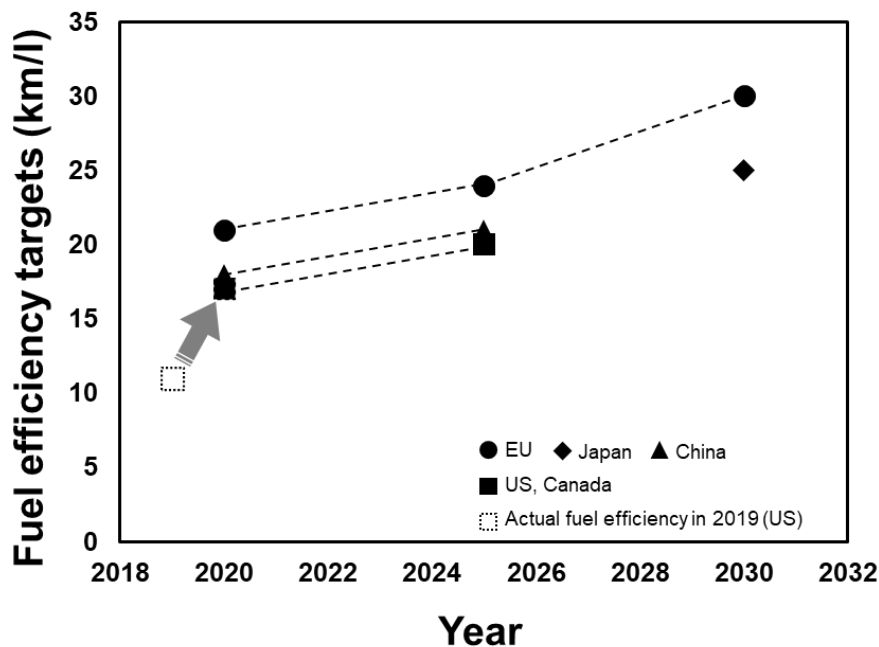


Fig. 1.1 Change in fuel efficiency targets in each country with year and actual fuel efficiency in US in 2019 [1.2, 1.3].

Reducing the body weight of automobiles is one of the most promising ways to increase the fuel efficiency. Lightweight vehicle bodies require a lower amount of energy to move regardless of the propulsion system because frictional force decreases with a decrease in the mass. It can be also accelerated and decelerated easily because acceleration is expressed by an equation of force divided by the mass [1.4]. Many researches have been carried out to investigate the effect of car body weight reduction on the fuel efficiency. Isenstadt et al. reported that 10% reduction of vehicle body weight improves 5.1% of the fuel efficiency [1.4] and Cheah et al. insisted that 10% reduction of car body weight increases the fuel efficiency by 6.9% [1.5]. The multi-material

structure, which is composed of high tensile strength steel (HTSS), light metals, and polymers, has been adopted to an automobile body to decrease the vehicle body weight. **Figure 1.2** shows an example of the vehicle body built based on the multi-material structure concept [1.6]. The body weight of vehicles could be reduced about 30% when carbon fiber reinforced plastics (CRPPs) are adopted to automotive components with steels [1.7]. There is a case which successfully reduced the body weight around 100 kg by using the CFRP and Al alloy together in the body structure [1.8]. The multi-material structure includes joint parts between metals and polymers. Joining dissimilar materials is a key technology for the practical application and design for the multi-material structure.

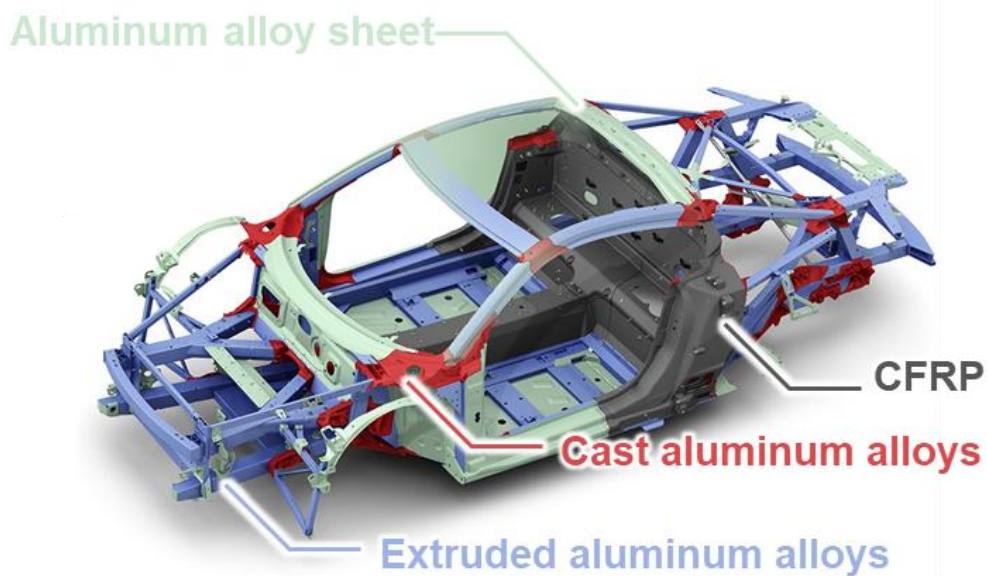
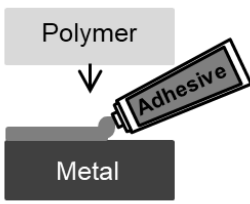
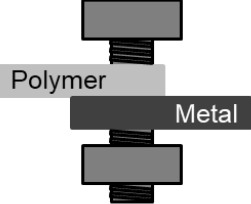
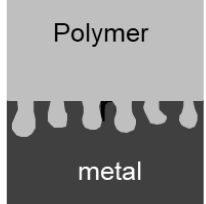


Fig. 1.2 An example of vehicle body built by multi-material structure concept [1.6].

Suzuki et al. [1.9] reviewed various joining technology for joining metals and polymers. **Table 1.1** summarizes metal/polymer joining methods and associated advantages and disadvantages. Adhesive, mechanical fastener, and thermal joining are the representative joining methods. All the joining methods have several advantages and disadvantages. For example, the adhesives distribute stress over the entire bonded interface. However, the adhesives could degrade with high temperature and humid conditions [1.10] and require much processing time for curing. The mechanical fasteners indicate high joint strength and durability, however, stress concentration and increase in the body weight and the number of components are the main issue. The thermal joining is a direct joining method which does not use the adhesives and mechanical fasteners. The thermal joining is possible when a polymer material is melted and contact with a metal surface. The method utilizes mechanical interlocking which acts when the liquid polymer interlocked with asperities (e.g. dimples, grooves, and protrusions) on the metal surface. The formation of chemical

bonding at the interface formed during the thermal joining process is often responsible for the adhesion. Stress anisotropy is the main issue with this method. The joint strength decreases when a stress is applied perpendicular to the interface [1.11]. Thus, it cannot be concluded that which method is the best among general joining methods. However, it is important to solve the disadvantages of each method to extend the scope of application. The present study focuses on solving disadvantages of the thermal joining.

Table 1.1 Metal polymer joining methods and comparison [1.9].

	Adhesive	Mechanical fastener	Thermal joining
Schematic illustration			
Joint strength	○	○	× Insufficient strength
Durability	× Degradation over time	○	○
Stress contribution	○	× Stress singularity	○
Cost	○	× More parts required	○
Processing time	× Long processing time	○	○
Bonding after molding	○	○	× Need to melt the polymer

1.2. Characteristics of metal/polymer direct joining

Several well-known factors which influence the joint strength of directly joined metal/polymer hybrid structure are reviewed here.

1.2.1. Surface wetting

Wetting the surface of a metal by a polymer is the most essential because a penetration of the polymer into asperities formed on the metal substrate and the formation of chemical bonding does not occur without an intimate contact between the metal and polymer. **Figure 1.3** illustrates the relationship among the surface tension of the liquid (γ_L), solid (γ_S) and the surface tension between the liquid and solid (γ_{LS}). The wettability (A) between the liquid and solid substrate is given by following Young's equation.

$$\gamma_S - \gamma_{LS} = \gamma_L \cos \theta \quad (1.1)$$

where θ is the contact angle and used as a measure for indicating the wettability. Low contact angle indicates good wettability. The contact angle value of 90° is usually a criterion for a wetting

or non-wetting condition. The work of adhesion (W) is defined as a required work to separate the liquid and solid from the interface.

$$W = \gamma_S + \gamma_L - \gamma_{LS} \quad (1.2)$$

$\gamma_S + \gamma_L$ indicates the tensions of new surfaces created by separating the solid metal and liquid polymer and γ_{LS} indicates the surface tension arising on the metal/polymer interface. More energy is needed to separate the liquid polymer from the solid metal surface by an increase in the work of adhesion. Substituting Eq. (1.1) into Eq. (1.2), the following equation is obtained.

$$W = \gamma_L(1 + \cos \theta) \quad (1.3)$$

The work of adhesion increases with increasing γ_L and decreasing the contact angle. γ_L is a unique value for each liquid, while the contact angle is affected not only the combinations of solids and liquids, but also the characteristics of the solid surfaces including the morphology and functional group [1.12]. In summary, the low contact angle is favorable to join metals with polymers easily and obtain high joint strength.

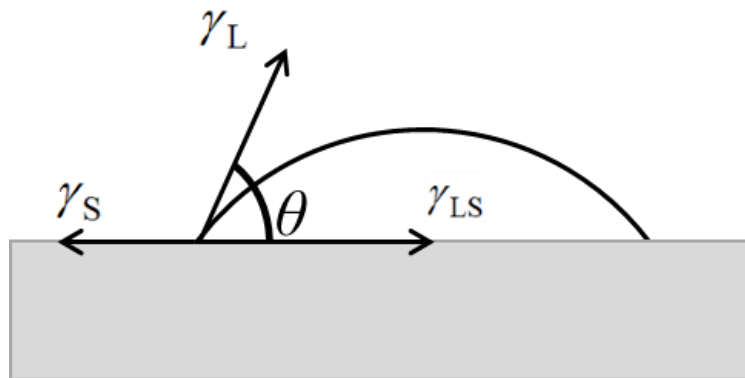


Fig. 1.3 Schematic illustration of a liquid drop on a solid sheet showing contact determined by the balance among the surface tensions.

1.2.2. Chemical bond

There are two kinds of bond, primary and secondary bonds. Metallic bond, covalent bond, and ionic bond are the primary bonds. Van der Waal's force is the most basic secondary bonds. The primary bond is stronger than the secondary bond in nature [1.13]. However, the primary bond basically does not act between metals and polymers. Therefore, the secondary bond largely contributes the adhesion between metals and polymers [1.14].

The metallic bond and covalent bond act mainly in metal and polymer materials, respectively. Traditionally, it was thought that these materials cannot be welded because they have different types of bond in nature [1.14]. However, it has been found that some polymer materials can be welded to metals. Katayama et al. [1.15] demonstrated the weldability between a

polyethylene terephthalate (PET) and a stainless-steel plate. Cr oxide and an intimate contact of atoms were formed at the interface of the PET/steel joint structures. Arkhurst et al. [1.16] welded a carbon fiber reinforced plastic (CFRP) with a Mg alloy by hot-pressing at the temperature higher than the melting point of the polymer matrix. The matrix for the CFRP was thermoplastic polyurethane, which contains C=O functional group. It was found that Mg oxide was formed along with the Mg alloy/CFRP interface, resulting in high joint strength. Kondoh et al. [1.17] joined a pure Ti substrate with polyamide66 (PA66), polystyrene (PS) and PET substrates by hot-pressing. The PA66 and PET substrates were able to be joined with the Ti substrate in the case that the joining temperature increased close to the melting temperature of each polymer material as indicated in Fig. 1.4 (a). It was found that Ti oxide was formed along with the Ti/polymer interface. In constant, the PS substrate was not joined with the Ti substrate. The structural formulas of the used polymers are shown in Fig. 1.4 (b). The authors insisted that the PA66 and PET contains C=O/C-O functional groups, which facilitated the formation of the Ti oxide.

Isoyama et al. [1.12] summarized adhesion characteristics between polymer and Al surface. The adhesion force between the Al surface and polymer can be divided into hydrogen bonding and Van der Waal's force. Van der Waal's force is also divided into dipole-induced dipole interaction and dispersion bond. The hydrogen bond and dispersion force are the strongest and weakest secondary bond, respectively. The hydrogen bond is formed when OH group on the Al surface interacts with O atom in polymer.

It seems that functional groups in the polymers play an important role in the joinability between metals and polymers.

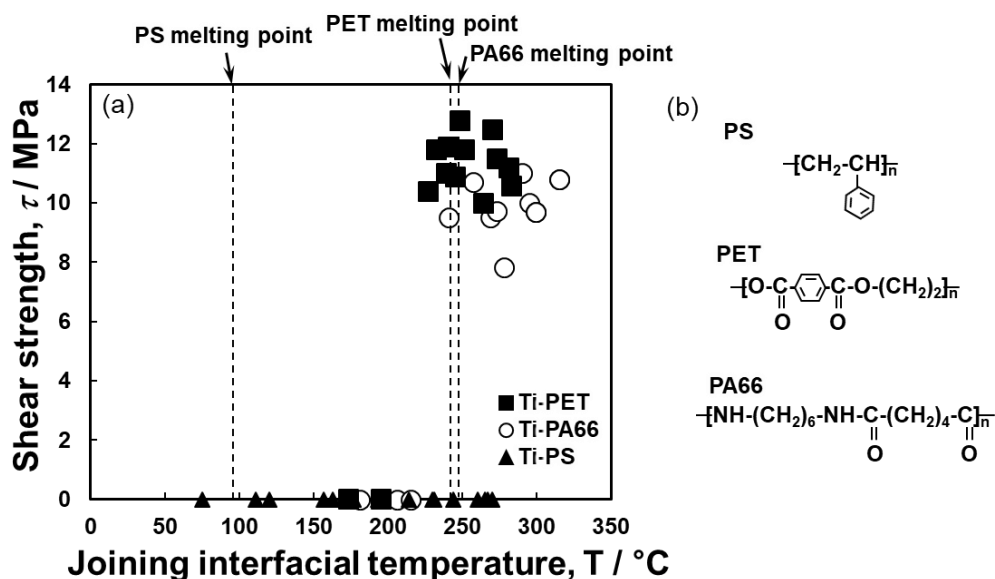


Fig. 1.4 (a) Change in lap shear strength of Ti/polymers lap joints formed by hot-pressing as a function of joining interfacial temperature and (b) chemical structural formula of each polymer [1.17].

1.2.3. Mechanical interlocking

Mechanical interlocking functions properly only when the polymer in liquid phase interlocks with the asperities. Mechanical interlocking almost always contributes to adhesion between polymers and metals. It is believed that adhesion is possible only by mechanical interlocking when chemical bonding does not act [1.14]. According to Kondoh et al [1.17], the PS substrate was not able to be joined with aluminum substrate. However, Taki et al. [1.18] joined Al substrates with polybutylene terephthalate (PBT), acrylonitrile butadiene styrene (ABS) and PS substrates by injection molded joining process. The Al substrate was textured by laser ablation before the joining process. Groove morphology formed on the metal surface facilitates mechanical interlocking with all types of polymers, resulting in the high joint strength. Schricker et al. [1.19] also demonstrated that polycarbonate (PC) was not joined with a steel substrate with smooth surface, but could be joined with the surface textured metal by laser. In addition, the joint strength of a stainless-steel/polyamide-6 (PA6) hybrid structure greatly improved with the surface grooves. Obviously, polymer materials which include unfavorable functional group for forming chemical bonding with a metal surface can be joined with the metal if mechanical interlocking is adopted.

1.2.4. Stress singularity

One of the problems for joining metals and polymers is a stress singularity generated at the interface edge. The large difference in the mechanical characteristics between metals and polymers (e.g. Poisson's ratio and Young' modulus) is the main reason for the stress singularity. The value of the singularity is theoretically infinite [1.20]. This interface edge of the metal and polymer joint often becomes the origin of failure, therefore, it is important to reduce the singularity to improve the metal/polymer joint strength.

Suzuki et al. [1.21] carried out experiments and a computational analysis to reduce the stress singularity of Al/epoxy resin joints by introducing interpenetrate phase layer (IPL) at the interface of the Al and epoxy resin. An open porous layer was formed on the Al surface, followed by an infiltration of the epoxy resin into the porous layer. The Al and epoxy resin three-dimensionally interlocked each other at the porous layer and formed the IPL. The joint strength increased with an increase in the thickness of the IPL as shown in **Fig. 1.5**. The IPL which indicates the medium mechanical properties between the Al and epoxy resin reduced the singular stress (von Mises stress), resulting in increasing in the joint strength.

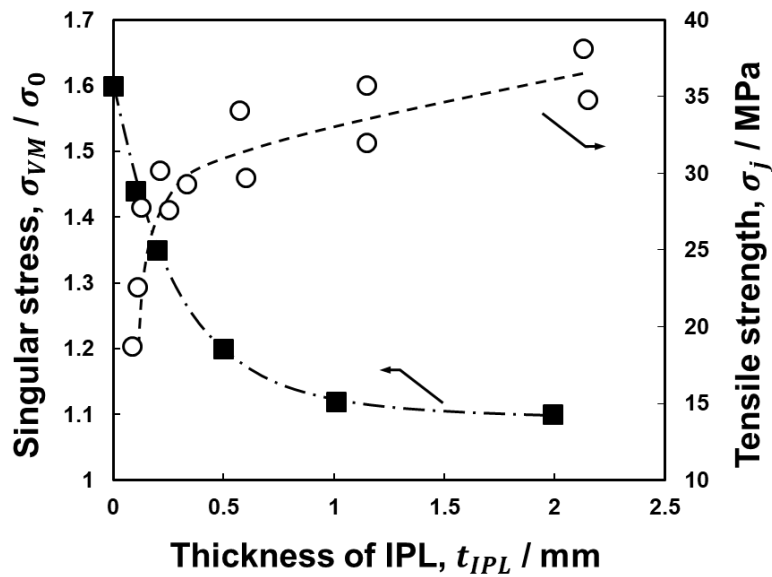


Fig. 1.5 Effect of thickness of the interpenetrating phase layer (IPL) on the singular stress and tensile strength of Al/epoxy joint via the IPL [1.21].

1.3. Metal/polymer direct joining through mechanical interlocking

Plastics can be divided into two groups, thermoplastics and thermosettings. The main difference between the thermoplastics and thermosettings is that the thermoplastics can be melted again at high temperature whereas the thermosettings cannot. The thermoplastics are getting attention as a matrixes of a fiber reinforced polymer [1.22]. According to Jones [1.23], the thermoplastics are classified into two groups, semi-crystalline and amorphous thermoplastics. The amorphous thermoplastics consist of chain molecules without periodicity. The thermoplastics which have the repeated molecule chain units are the semi-crystalline thermoplastics. The semi-crystalline thermoplastics consist of amorphous and crystalline phases. The direct joining through mechanical interlocking often carried out with the thermoplastics because it associates with polymer melting process.

The mechanical interlocking, which is also called anchor effect or hooking, is a critical factor for the direct joining between metals and polymers as mentioned in section 1.2.4. The intrusive and protrusive morphology on the metal surface facilitate the transmission of an applied external force along the surface [1.24]. The joint strength significantly depends on the presence of the undercut [1.25], which is defined as a space formed by the removal or deposition of the material on the surface. In short, distributing the external force through the surface by forming the undercut on the surface is a critical point for the mechanical interlocking.

The metal/polymer direct joining process utilizing the mechanical interlocking involves metal surface modifying and joining processes. Previous researches were briefly introduced in this section.

1.3.1. Metal surface modifying process

The surface morphology of a metal surface is responsible for changing in the joint strength of the metal/polymer hybrid structure. The schematic illustration and an example modified surface are shown in Fig. 1.6. Laser surface texturing [1.11, 1.18, 1.26-1.31] and chemical etching [1.25, 1.32-1.36] are used to fabricate pores or grooves on the metal surface. Sand blasting [1.37-1.40] is also used to form the rough metal surface. Rodriguez-vidal et al. [1.28] modified a metal surface using laser ablation. Grooves were formed and molten metal material was re-casted around the grooves during the laser ablation process. They changed the number density, depth, and width of grooves and height of the re-casted structure by changing the number of the laser scanning. The aspect ratio of grooves, height of the re-casted structure and number density of the grooves indicated a positive correlation with the joint strength. Nagato et al. [1.34] controlled the depth and diameter of dimples by electrochemical process. The joint strength increased as the depth and diameter of the dimple increased. Kleffel et al. [1.25] modified a metal surface by electrochemical method. Tensile strength of the metal/polymer joint was

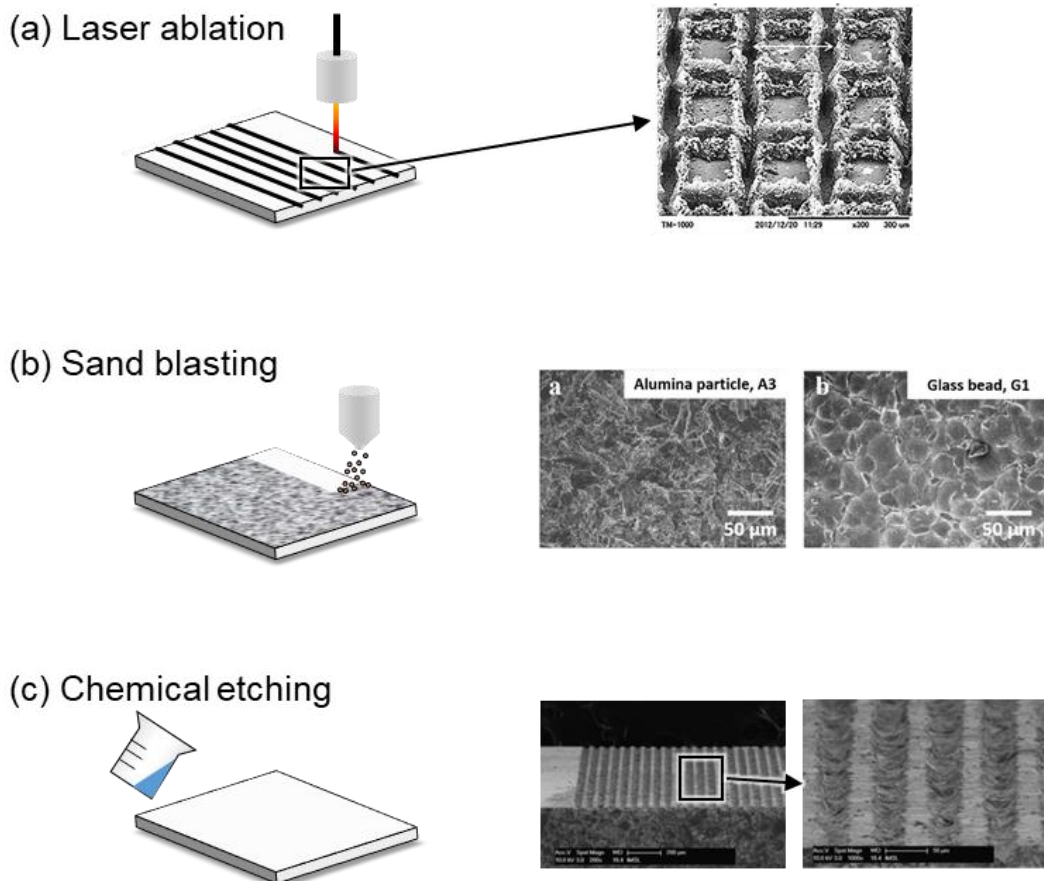


Fig. 1.6 Schematic illustrations of surface treatment processes for modifying metal surfaces and their example images of surface structures; (a) laser ablation [1.18], (b) sand blasting [1.37], and (c) chemical etching [1.32].

measured, and roughness parameters were not enough to explain the joint strength perpendicular to the joining surface. The presence of the undercut was responsible for the high joint strength. Kajihara et al. [1.37] and Lucchetta et al. [1.39] modified a metal surface by sand blasting and found that the roughness parameter related with the depth showed a positive correlation with the joint strength. Li et al. [1.40] treated a metal surface by sand blasting and found that the metal surface with homogeneously distributed many large holes was beneficial for increasing the joint strength. These studies measured the morphology of the metal surface quantitatively and demonstrated that the joint strength significantly depending on the morphology of the metal surface.

1.3.2. *Joining processes and metal/polymer joint characteristics*

Many kinds of joining processes have been carried out for joining metals and polymers. Injection molded direct joining, laser assisted welding, ultrasonic welding, friction (spot) stir welding, resistance spot welding, and hot-pressing are the representative thermal joining process. Schematic illustrations of the metal/polymer joining process are shown in **Fig. 1.7**.

Schematic illustration of the injection molded direct joining process is shown in **Fig. 1.7 (a)**. The injection molded direct joining is based on the injection molding technique. A surface modified metal is put in a mold, followed by the injection molding of a polymer. Taki et al. [1.18] produced laser-textured Al/polymer lap joints by the injection molded direct joining. The joint strength increased with increasing the temperature of nozzle and mold. The viscosity of the polymer decreased with increasing the temperature, resulting in the enhanced penetration of polymer into the grooves. Kimura et al. [1.33] joined Al and polymers by injection molded direct joining. The Al substrate was textured by laser before the joining process. The joint strength increased with increasing the molding pressure and decreasing the injection speed. The infiltration of the polymer improved due to the high pressure. Viscous resistance decreased with a decrease in the injection speed.

Figure 1.7 (b) shows schematic illustration of the ultrasonic welding process. Balle et al. [1.41] reviewed the ultrasonic welding process and investigated the effects of process parameters on the joint characteristics and possible joining mechanism. The ultrasonic welding process is characterized by low energy input, low temperature, and short welding time. The ultrasonic welding process is suitable for welding CFRPs and Al alloys. The direction of oscillation, welding force and oscillation amplitude were optimized for increasing the joint strength. The carbon fiber bundles without the polymer matrix were able to be welded to the Al surface. The interface of the CFRP/Al joint welded by the ultrasonic process showed that the Al and carbon fibers were interlocked, and the polymer was displaced out from the interface. It was thought that the interlocking of the Al and carbon fibers is the main reason for the weldability of

the Al/CFRP by the ultrasonic process. Yeh et al. [1.13] utilized the ultrasonic technique to fabricate an Al/ABS hybrid joint. A laser was used for texturing the Al surface before joining. Surface grooves facilitated interlocking with the ABS polymer, which made it possible to join the metal and polymer. The joint strength increased with an increase in the mold temperature during the joining process.

The laser welding is characterized by high power input at high speed in short time. The schematic illustration is shown in Fig. 1.7 (c). The stacked metal/polymer substrates are irradiated

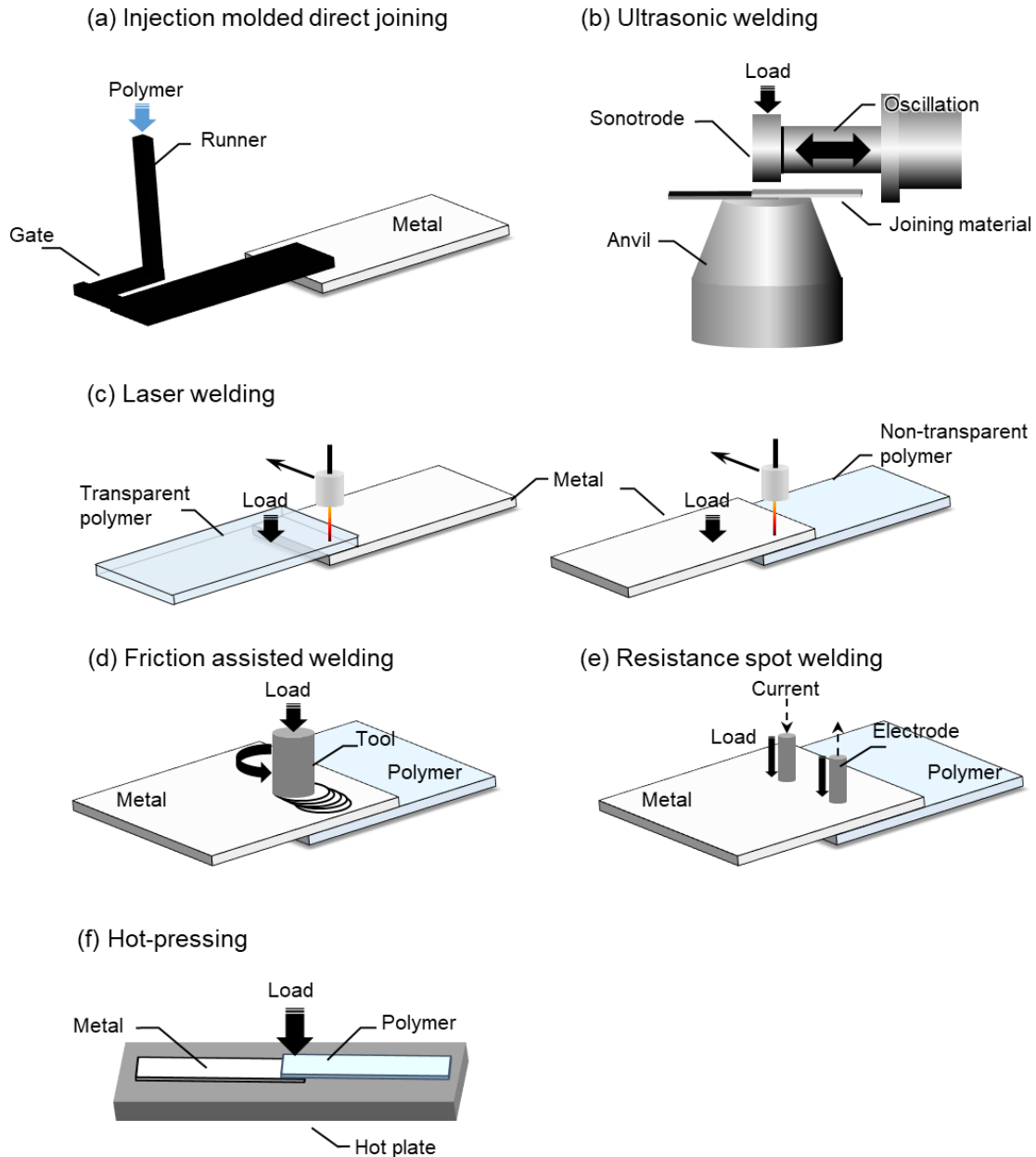


Fig. 1.7 Schematic illustrations of metal/polymer joining process; (a) injection molded direct joining [1.33], (b) ultrasonic welding [1.40], (c) laser welding, (d) friction assisted welding, (e) resistance spot welding and (f) hot-pressing.

by the laser. In the case of the polymer with high transparency, the metal surface can be heated by laser irradiating on the polymer side. In the case of the polymer with low transparency, the polymer is heated by thermal conduction from the metal substrate irradiated with the laser. Katayama et al. [1.17] firstly developed the metal/polymer laser direct welding. Stainless-steel and PET substrates were used as joining materials. Transmission electron microscopes (TEM) demonstrated that tight bond in atomic level was formed. Bubbles were formed around the metal/polymer interface. It was thought that the molten polymer expands rapidly due to the generation of the bubbles, resulting in penetrating the molten polymer into the asperities on the metal substrate. The authors insisted that both mechanical interlocking and chemical bonding contributed the joint strength. Lambiase et al. [1.42] investigated the effects of process parameters of the laser spot welding on the mechanical behavior of a laser-textured Al/polyetheretherketone (PEEK) hybrid joint. Laser power and laser heating time were adjusted. The metal/polymer interface joining temperature increased with an increase in the laser power and heating time. However, the PEEK degraded by longer heating time, resulting in the reduced joint strength. Higher laser power with short welding time was favorable for high joint strength.

The friction assisted welding is schematically illustrated in **Fig. 1.7 (d)**. When the welded region is spot, the processes are called friction spot welding. Amancio-Filho et al. [1.43] demonstrated the feasibility of the friction assisted welding. The friction assisted welding is characterized by operation simplicity and short joining cycles. Metals and polymers are stacked together, followed by rotating a tool on the metal to generate friction heat. The mechanical interlocking between two materials is achieved during the friction process. It is thought mechanical interlocking and chemical bonding are contributing factors for the friction assisted welding. Goushegir et al. [1.44] examined the effect of process parameters on the mechanical performance of an Al/CFRP (polyphenylene sulfide matrix, PPS) joint. The joining pressure, joining time, sleeve plunge depth, and rotating speed were controlled as the process parameters. The joining time, rotating speed, and joining pressure significantly affected the joined area because heat input and flow of molten polymer is influenced by these parameters. The rotating speed was the most critical process parameter.

Schematic illustration of the resistance spot welding is shown in **Fig. 1.7 (e)**. Nagatsuka et al. [1.45] attempted to join stainless-steel and CFRP (PA6, acid-modified polypropylene (PP), and PPS matrix) substrates by the resistance spot welding. The joint strength showed correlations with welding current and welding time. Local heat generated by current pass through the metal substrate melted polymer matrix, resulting in chemical bonding between the metal and polymer. The CFRP with PPS matrix was not able to be joined because of the absence of a polar functional group in the polymer.

The hot-pressing is the simplest thermal joining process. The schematic illustration is

indicated in **Fig. 1.7 (f)**. A polymer substrate is put on a metal substrate placed on a hot-plate and pressurized while heating the hot-plate. The joining process is finished by taking out the joint from the hot plate. Arkhurst et al. [1.16] and Kondoh et al. [1.17] fabricated metal/polymer joints by hot-pressing. The metal and polymer were joined when the hot plate was heated around the melting temperature. They found that metal oxide was generated at the interface of the metal and polymer. It was also found that functional groups in the polymer were an important factor for the joinability.

1.4. Metal/polymer direct joining via an additively manufactured anchor layer

The conventional surface modifying processes were briefly reviewed in section 1.3.1. Many researchers utilized the grooves or pores for joining metals and polymers. There are several disadvantages with these processes. Schematic illustration of metal/polymer joints via the pores is shown in **Fig. 1.8 (a)**. These processes fabricate the pores or grooves on the metal surface by removing material. In this case, the tensile strength (perpendicular to the joint interface) is low compared to the shear strength (parallel to the joined surface) since the absence of the undercuts parallel to the joint interface [1.11]. Moreover, when the metal/polymer joint via the pores generated on the metal surface, the stress concentrates on the root of polymer penetrating pores due to the geometrical feature. As a result, the joint strength determined by the strength of polymer which is lower than that of metal. Also, a high pressure needs to be applied during joining processes to penetrate the polymer into the pores.

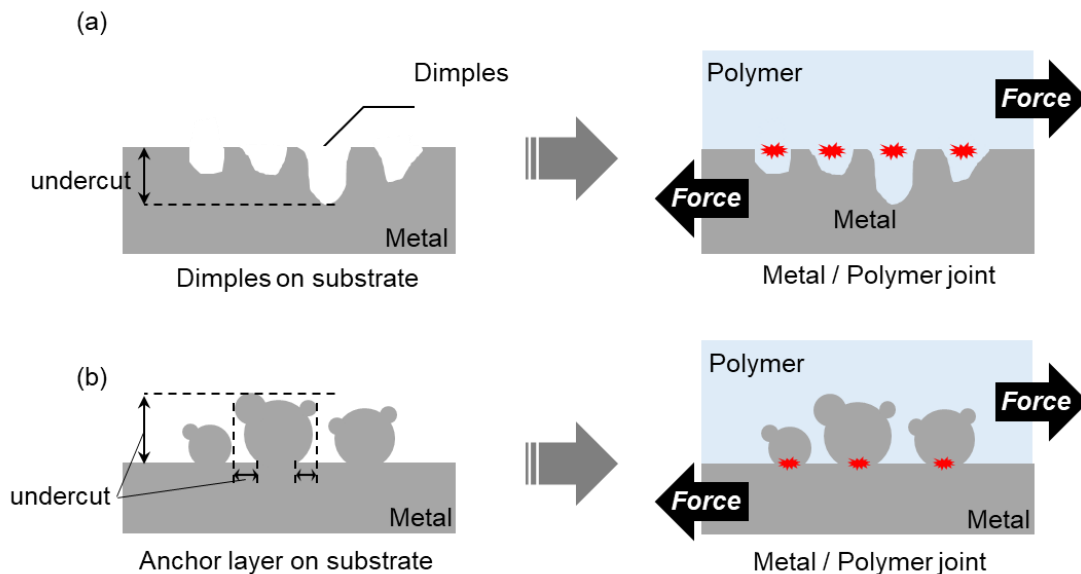


Fig. 1.8 Schematic illustrations of metal/polymer joints formed via (a) dimples and (b) additively manufactured anchor layer.

Recently, a novel route to fabricate the metal/polymer hybrid structure was developed. The schematic illustration of the joining method is shown in **Fig. 1.9**. A powder blend is staked on the metal surface, followed by a single track laser irradiation. A metallic layer is additively manufactured on the metal surface, which is called as an anchor layer. The anchor layer interlocks with the polymer as inducing the anchor effect, and the metal and polymer is joined via this anchor layer. The anchor layer has protrusive morphology. The anchor layer can be fabricated rapidly and locally at a target area on the metal surface. It is thought that the protrusive morphology has several advantages for joining metals and polymers. Schematic illustration of metal/polymer joint via the anchor layer is indicated in **Fig. 1.8 (b)**. For example, it is expected that the joining pressure during the process will significantly decrease because high stress will arise on the top of the protrusive structures and promote the interpenetration of the polymer with the anchor layer. In addition, the stress concentration arises on the root of the protrusive structures which indicate higher strength compared with the polymer, leading to high joint strength. Reducing the joint strength anisotropy is also expected because the undercut in the direction parallel to the joint interface is formed easily.

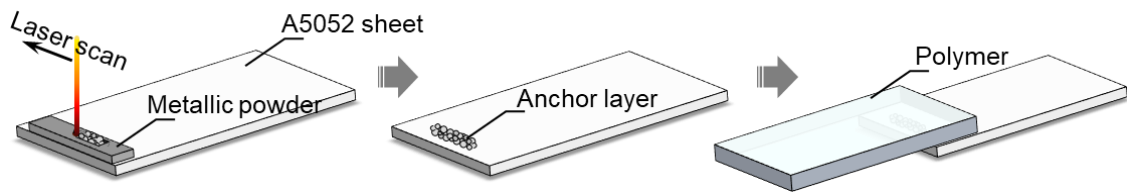


Fig. 1.9 Schematic illustration of anchor layer forming process.

1.5. Purpose of this research

In previous studies, metals and polymers were often joined via the dimples or grooves formed on the metal surface. As mentioned in section 1.3.4, the anchor layer which shows protrusive morphology will be beneficial in terms of the joint strength and easiness of joining process. However, the process for fabricating this kind of anchor layer has never been researched before. The main purpose of this study is to develop a process for additively fabricating the anchor layer on the Al substrate to strongly join metals and polymers. The effect of the anchor layer fabricating process conditions on the structure and microstructure of the anchor layer and the mechanical properties of the Al/polymer joint via the anchor layer were investigated. In addition, the optimal joining process during hot-pressing and the structural design hints of the anchor layer for enhancing the joint strength were suggested.

The present thesis is composed of 7 chapters.

The social background for the necessity of the multi-material structure and previous researches about joining metals and polymers were reviewed in Chapter 1.

The effects of surface treatments on the wettability of metal surface is investigated in Chapter 2.

The anchor layer is fabricated on an Al alloy (A5052) surface with Al-Ti-C, Al-Ti and Al powders. The fabricated anchor layers are characterized and mechanical behaviors of the Al/PA6 joint via each anchor layer are analyzed in Chapter 3.

The influence of temperature history during hot-press joining on the mechanical behaviors of the Al/PA6 joints is investigated in Chapter 4.

The C powder composition in the Al-Ti-C powder mixture was controlled. Change in the morphology and microstructure of the anchor layers and mechanical behaviors is examined in Chapter 5.

The laser energy input is controlled by changing in the laser scan speed and power. Change in the morphology and microstructure of the anchor layers and joint strength is investigated in Chapter 6.

The results obtained in this study are summarized and future works are stated in Chapter 7.

References

- [1.1] An official website of the European Union, “Reducing CO2 emissions from passenger cars - before 2020”. https://ec.europa.eu/clima/policies/transport/vehicles/cars_en, (accessed 2020-4-20).
- [1.2] Hula, A., French, R., Bunker, A., Rojeck, T. The 2019 EPA Automotive trends report: Greenhouse Gas Emissions, Fuel Economy, and Technology since 1975. United states environmental protection agency. 2020.
- [1.3] Yang, Z., Rutherford, D. Japan 2030 fuel economy standards. The international council on clean transportation. 2019.
- [1.4] Isenstadt, A., German, J., Bubna, P., Wiseman, M., Venkatakrisnan, U., Abbasov, L., Guillen, P., Moroz, N., Richman, D., Kolwich, G. Lightweighting technology development and trends in US passenger vehicles. International Council on Clean Transportation working paper. 2016, 25.
- [1.5] Cheah, L. W. Cars on a diet: the material and energy impacts of passenger vehicle weight reduction in the US. Doctoral dissertation, Massachusetts Institute of Technology. 2010.
- [1.6] Audi technology portal, “New Audi Space Frame with high proportions of aluminum and CFRP”. <https://www.audi-technology-portal.de/en/body/aluminium-bodies/new-audi-space-frame-with-high-proportions-of-aluminum-and-cfrp>, (accessed 2020-4-20).
- [1.7] Takahashi, R. Ryousanshakeiryouka no tameno CFRTTP kaihatsu ~Kentoujikou to sono kangaekata~. S&T Gijutsusemina. 2011.
- [1.8] LEXUS (2009), Press information 2009 LEXUS LFA.

- [1.9] Suzuki, A. Joining between metals and polymers via additively manufactured porous layer for components of vehicles. *Material stage*. 2019, 19(2), 16-21.
- [1.10] Tomita, Y., Shohji, I., Koyama, S., Shimizu, S. Degradation behaviors of adhesion strength of structural adhesive for weld-bonding under high temperature and humidity conditions. *Procedia engineering*. 2017, 184, 231-237.
- [1.11] Yeh, R. Y., Hsu, R. Q. Development of ultrasonic direct joining of thermoplastic to laser structured metal. *International Journal of Adhesion and Adhesives*. 2016, 65, 28-32.
- [1.12] Isoyama, E., Uchiyama, T. Surface properties of aluminum and its bonding characteristics. *The Japan Institute of Light Metals*. 1985, 35(3), 176-187.
- [1.13] Callister, W. D., Rethwisch, D. G. *Materials science and engineering*. NY: John wiley & sons. 2011.
- [1.14] Savage, W. *Joining of advanced materials*. Elsevier. 2013.
- [1.15] Katayama, S., Kawahito, Y. Laser direct joining of metal and plastic. *Scripta materialia*. 2008, 59(12), 1247-1250.
- [1.16] Arkhurst, B. M., Kim, J. H., Lee, M. Y. Hot metal pressing joining of carbon fiber reinforced plastic to AZ31 Mg alloy and the effect of the oxide surface layer on joint strength. *Applied Surface Science*. 2019, 477, 241-256.
- [1.17] Kondoh, K., Umeda, J. CO bond enhancing direct bonding strength between plastic and pure titanium. *Materials Letters*. 2018, 211, 331-334.
- [1.18] Taki, K., Nakamura, S., Takayama, T., Nemoto, A., Ito, H. Direct joining of a laser-ablated metal surface and polymers by precise injection molding. *Microsystem Technologies*. 2016, 22(1), 31-38.
- [1.19] Schricker, K., Samfaß, L., Grätzel, M., Ecke, G., Bergmann, J. P. Bonding mechanisms in laser-assisted joining of metal-polymer composites. *Journal of Advanced Joining Processes*. 2020, 1, 100008.
- [1.20] Ryoji, Y. *Mechanics of interface*. Baifukan. 1993.
- [1.21] Suzuki, A., Arai, Y., Takata, N., Kobashi, M. Effect of layer thickness on bonding strength of Al/epoxy resin joints via interpenetrating phase layer. *Journal of Materials Processing Technology*. 2018, 254, 338-345.
- [1.22] Yan, X., Imai, Y., Shimamoto, D., Hotta, Y. Relationship study between crystal structure and thermal/mechanical properties of polyamide 6 reinforced and unreinforced by carbon fiber from macro and local view. *Polymer*. 2014, 55(23), 6186-6194.
- [1.23] Jones, I. Laser welding of plastics. In *Handbook of Laser Welding Technologies*. Woodhead Publishing. 2013.
- [1.24] Karbhari, V. M. (Ed.). *Rehabilitation of Metallic Civil Infrastructure Using Fiber Reinforced Polymer (FRP) Composites: Types Properties and Testing Methods*. Elsevier. 2014.

- [1.25] Kleffel, T., Drummer, D. Investigating the suitability of roughness parameters to assess the bond strength of polymer-metal hybrid structures with mechanical adhesion. *Composites Part B: Engineering*. 2017, 117, 20-25.
- [1.26] Byskov-Nielsen, J., Boll, J. V., Holm, A. H., Højsholt, R., Balling, P. Ultra-high-strength micro-mechanical interlocking by injection molding into laser-structured surfaces. *International journal of adhesion and adhesives*. 2010, 30(6), 485-488.
- [1.27] Roesner, A., Scheik, S., Olowinsky, A., Gillner, A., Reisgen, U., Schleser, M. Laser assisted joining of plastic metal hybrids. *Physics Procedia*. 2011, 12, 370-377.
- [1.28] Rodríguez-Vidal, E., Sanz, C., Lambarri, J., Quintana, I. Experimental investigation into metal micro-patterning by laser on polymer-metal hybrid joining. *Optics & Laser Technology*. 2018, 104, 73-82.
- [1.29] Lambiase, F., Paoletti, A. Friction assisted joining of titanium and polyetheretherketone (PEEK) sheets. *Thin-Walled Structures*. 2018, 130, 254-261.
- [1.30] Jiao, J., Jia, S., Xu, Z., Ye, Y., Sheng, L., Zhang, W. Laser direct joining of CFRTP and aluminium alloy with a hybrid surface pre-treating method. *Composites Part B: Engineering*. 2019, 173, 106911.
- [1.31] Zhao, S., Kimura, F., Kadoya, S., Kajihara, Y. Experimental analysis on mechanical interlocking of metal-polymer direct joining. *Precision Engineering*. 2020, 61, 120-125.
- [1.32] Kim, W. S., Yun, I. H., Lee, J. J., Jung, H. T. Evaluation of mechanical interlock effect on adhesion strength of polymer-metal interfaces using micro-patterned surface topography. *International Journal of Adhesion and Adhesives*. 2010, 30(6), 408-417.
- [1.33] Kimura, F., Kadoya, S., Kajihara, Y. Effects of molding conditions on injection molded direct joining using a metal with nano-structured surface. *Precision Engineering*. 2016, 45, 203-208.
- [1.34] Nagato, K., Yamaguchi, T., Nakao, M. Anchoring and chemical-bonding effects of anodic alumina microstructure on adhesion strength. *CIRP Annals*. 2018, 67(1), 595-598.
- [1.35] Kimura, F., Yamaguchi, E., Horie, N., Suzuki, G., Kajihara, Y. Formation of boehmite crystals on microblasted aluminum surface to enhance performance of metal-polymer direct joining. *Materials Letters*. 2020, 260, 126963.
- [1.36] Aliasghari, S., Skeldon, P., Zhou, X., Hashimoto, T. Effect of an anodizing pre-treatment on AA 5052 alloy/polypropylene joining by friction stir spot welding. *Materials Science and Engineering: B*. 2019, 245, 107-112.
- [1.37] Kajihara, Y., Tamura, Y., Kimura, F., Suzuki, G., Nakura, N., Yamaguchi, E. Joining strength dependence on molding conditions and surface textures in blast-assisted metal-polymer direct joining. *CIRP Annals*. 2018, 67(1), 591-594.

- [1.38] Goushegir, S. M., Dos Santos, J. F., Amancio-Filho, S. T. Friction spot joining of aluminum AA2024/carbon-fiber reinforced poly (phenylene sulfide) composite single lap joints: microstructure and mechanical performance. *Materials & Design (1980-2015)*. 2014, 54, 196-206.
- [1.39] Lucchetta, G., Marinello, F., Bariani, P. F. Aluminum sheet surface roughness correlation with adhesion in polymer metal hybrid overmolding. *CIRP annals*. 2011, 60(1), 559-562.
- [1.40] Li, X., Liu, F., Gong, N., Yang, C., Wang, B. Surface topography induced high injection joining strength of polymer-metal composite and fracture mechanism. *Composite Structures*. 2018, 184, 545-553.
- [1.41] Balle, F., Wagner, G., Eifler, D. Ultrasonic metal welding of aluminium sheets to carbon fibre reinforced thermoplastic composites. *Advanced Engineering Materials*. 2009, 11(1-2), 35-39.
- [1.42] Lambiase, F., Genna, S. Experimental analysis of laser assisted joining of Al-Mg aluminium alloy with polyetheretherketone (PEEK). *International Journal of Adhesion and Adhesives*. 2018, 84, 265-274.
- [1.43] Amancio-Filho, S. T., Bueno, C., Dos Santos, J. F., Huber, N., Hage Jr, E. On the feasibility of friction spot joining in magnesium/fiber-reinforced polymer composite hybrid structures. *Materials Science and Engineering: A*. 2011, 528(10-11), 3841-3848.
- [1.44] Goushegir, S. M., Dos Santos, J. F., Amancio-Filho, S. T. Influence of process parameters on mechanical performance and bonding area of AA2024/carbon-fiber-reinforced poly (phenylene sulfide) friction spot single lap joints. *Materials & Design*. 2015, 83, 431-442.
- [1.45] Nagatsuka, K., Xiao, B., Wu, L., Nakata, K., Saeki, S., Kitamoto, Y., Iwamoto, Y. Resistance spot welding of metal/carbon-fibre-reinforced plastics and applying silane coupling treatment. *Science and Technology of Welding and Joining*. 2018, 23(3), 181-186.

2. Effects of surface treatments on the wettability of metal surface

2.1. Introduction

The wettability is a critical factor to form chemical bonding and mechanical interlocking at the interface between metals and polymers as mentioned in section 1.2.4. The surface tension of liquid (γ_L) is a unique value for each liquid. It is necessary to increase the surface tension of solid (γ_S) or decrease the surface tension of liquid/solid interface (γ_{LS}) for increasing the wettability according to Eq. (1.2). Normally, organic impurities originating from the processing oil and atmosphere are adhered to surfaces of metal substrates [2.1]. The impurities decrease the surface tension of solid, resulting in low wettability between liquid polymers and solid metals.

It is well known that the plasma surface treatment can remove the organic impurities adhered on the metal surface. The process is environment-friendly because no waste liquid is generated after the treatment [2.2]. Recently, an atmospheric pressure plasma processing has attracted attention as a surface treatment method. The atmospheric pressure plasma process can be applied with a simple apparatus for short processing time due to absence of a vacuuming process [2.1].

The purpose of this chapter is investigating the effects of surface treatments and associated surface conditions on the wettability between liquids (water and epoxy resin) and an Al substrate. Various surface treatments including ethanol wiping, sand papering, and atmospheric plasma treatment are used. The wettability was evaluated by measuring the contact angle. Scanning electron microscopy (SEM) was used to observe the change in the surface morphology after the sand papering. X-ray photoelectron spectroscopy (XPS) was used to analysis the changes in the chemical conditions after all surface treatments.

2.2. Experimental method

The surface treatments on an Al alloy substrate (A5052) were conducted prior to measuring the contact angle. The surface treatments are summarized in **Table 2.1**. The sand papering was carried out with #220, 550, and 1200 SiC papers. The photography image of the atmospheric plasma treatment device is shown in **Fig. 2.1**. N₂ (0.5 %) + Air (99.5 %) gas mixture was flowed into the plasma head at a rate of 5 L/min and electrically discharge for generating a plasma. It was released through the rectangular exit with dimensions of 20 mm × 0.5 mm (length × width) located under the plasma head. The Al substrate was located on the conveyer belt. Speed of the conveyer belt (S) was fixed at 0.3 mm/s. Plasma treatment time (t) was controlled by the number of scan time (N) and calculated as follow.

$$t = N \cdot 0.5(\text{width of the plasma exit})/S \quad (2.1)$$

Table 2.1 Surface treatment for measuring the change in the contact angle.

Surface treatment	Sample number
As received	1
Ethanol wiping	2
Sand papering + ethanol wiping	3
Plasma treating (1.7s)	4
Sand papering + ethanol wiping + plasma treating (1.7s)	5
Sand papering + ethanol wiping + plasma treating (3.0s)	6

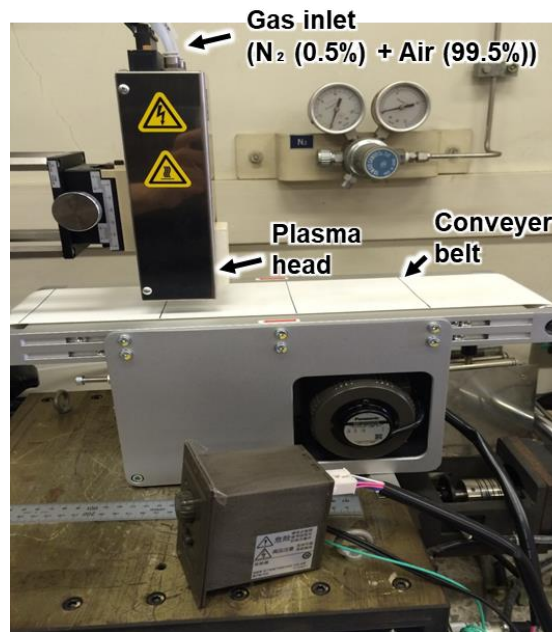


Fig. 2.1 Photo image of atmospheric pressure plasma treatment device.

The surface morphology of the Al substrate before and after sand papering was observed using the SEM. The XPS was conducted for investigating the change in chemical binding state of the Al surface after the surface treatments. The XPS measurement was carried out in a vacuum of 5×10^{-7} Pa. The take-off angle of the XPS apparatus was 0° and Al K α (1486.6 eV) was used as the X-ray source. The measurement mode was a twin anode. To prevent contamination of the XPS equipment, the analysis with as-received Al substrate was not carried out.

Figure 2.2 (a) shows the photography image showing an apparatus for measuring the contact angle (θ) by sessile-drop method. An example of captured sessile drop image by the CCD camera is shown in **Fig. 2.2 (b)**. Water and epoxy resin were used as liquids to measure the contact angle. To unify the size of the droplets, the same volume of the liquids was dropped on the Al substrate. **Figure 2.3** shows an example of time dependent change in the contact angle between the Al substrate and epoxy. The contact angle was measured 2 s after dropping the liquids. The average contact angle obtained from 5 measurements was calculated.

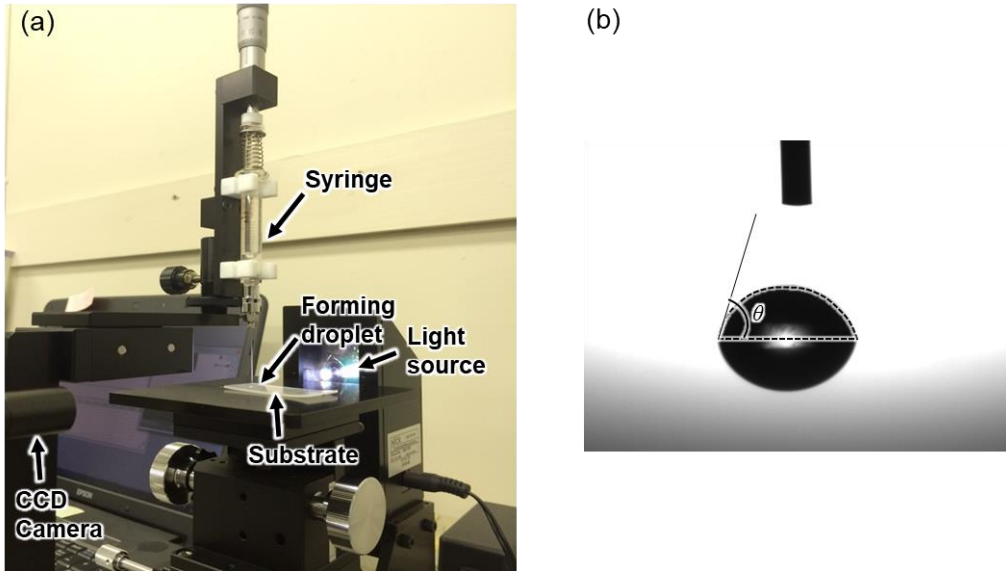


Fig. 2.2 (a) Contact angle measuring device and (b) representative sessile drop image to measure contact angle.

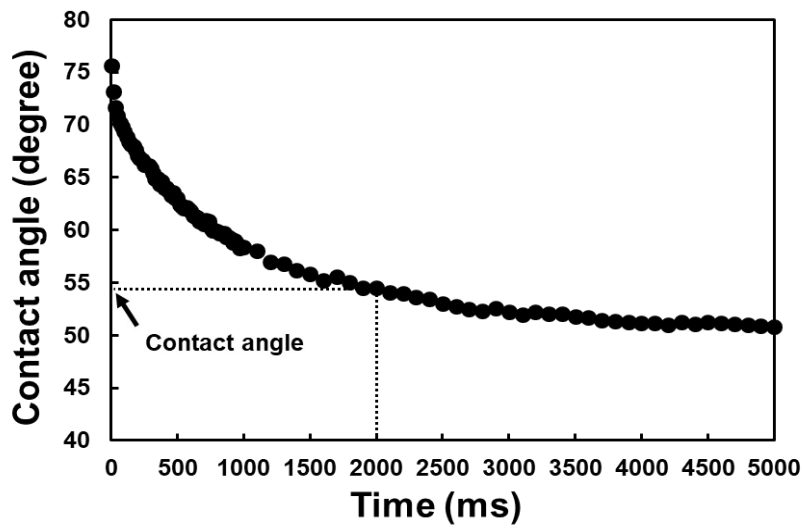


Fig. 2.3 An example of time dependent change in the contact angle.

2.3. Results

2.3.1. Change in the contact angle

The changes in the contact angles of water and epoxy resin on the Al substrate with different surface treatments are shown in **Fig. 2.4**. All of surface treatments affected the contact angle.

The contact angle between water and the as-received Al substrate was about 95° , which

means the wettability was poor (No. 1). The contact angle with water after ethanol wiping (No. 2) and sand papering + ethanol wiping (No. 3) was about 81 and 63°, respectively. Ethanol wiping and sand papering improved the wettability between water and the Al substrate. Plasma treatment alone (No. 4) drastically improved the wettability. The combination of the sand papering, ethanol wiping, and plasma treatment (No. 5) was effective for improving the wettability compared with the plasma treatment alone. The contact angle gradually decreased with an increase in the plasma treatment time (No. 5 and 6).

In the case of epoxy resin, the wettability with the as-received Al substrate was relatively good (approximately 54°). The wettability was improved after the ethanol wiping (No. 2) and sand papering + ethanol wiping (No. 3). The atmospheric plasma treatment (No. 4) also decreased the contact angle to almost the same value as sand papering and the ethanol wiping. The sand papering and ethanol wiping before the plasma treatment hardly affected the wettability compared with the plasma treatment alone (No. 4 ~ 6).

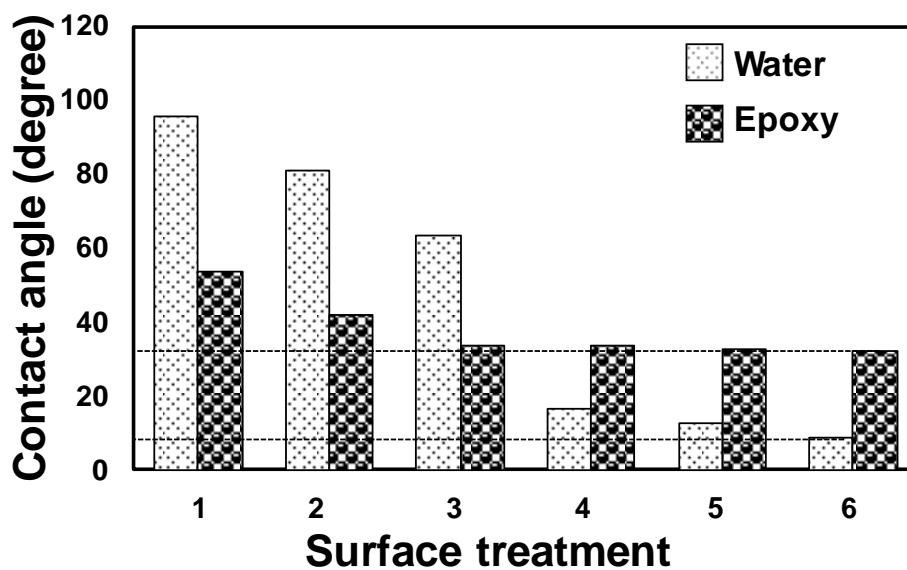


Fig. 2.4 Contact angle of liquid drop on the Al substrate with various surface treatment

2.3.2. Change in surface conditions

Figure 2.5 (a, b) shows the surface morphology of (a) the as-received Al substrate and (b) the specimen after sand papering and ethanol wiping. It was observed that the surface was roughened by sand papering.

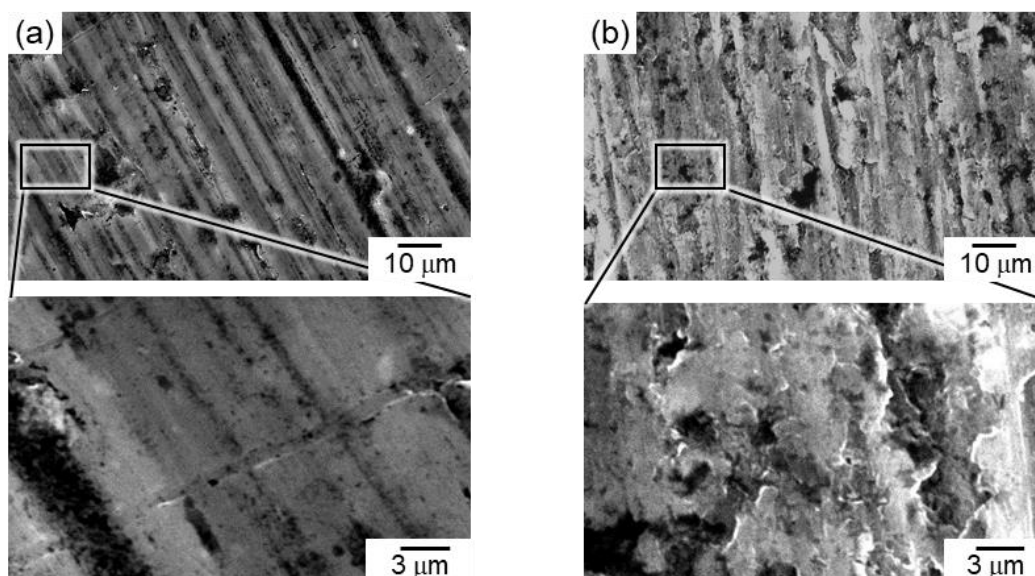


Fig. 2.5 SEM images showing the surface of the A1050 substrate: (a) as-received specimen and (b) specimen after sand papering and ethanol wiping.

Wide XPS profiles of ethanol treated, sand papered + ethanol wiped, and plasma treated (3s) Al surface are shown in **Fig. 2.6**. Al 2s, Al 2p, O 1s, and C 1s peaks were the most intensive peaks. It appears that the intensities of O 1s and C 1s peaks of the plasma-treated specimen were higher and lower, respectively, than those of ethanol treated and sand papered specimens. The C 1s and Al 2p peak regions were magnified and shown in **Fig. 2.7 (a)** and **(b)**. Four kinds of C binding energy peaks were included in the C 1s peaks in the ethanol wiped and sand papered + ethanol

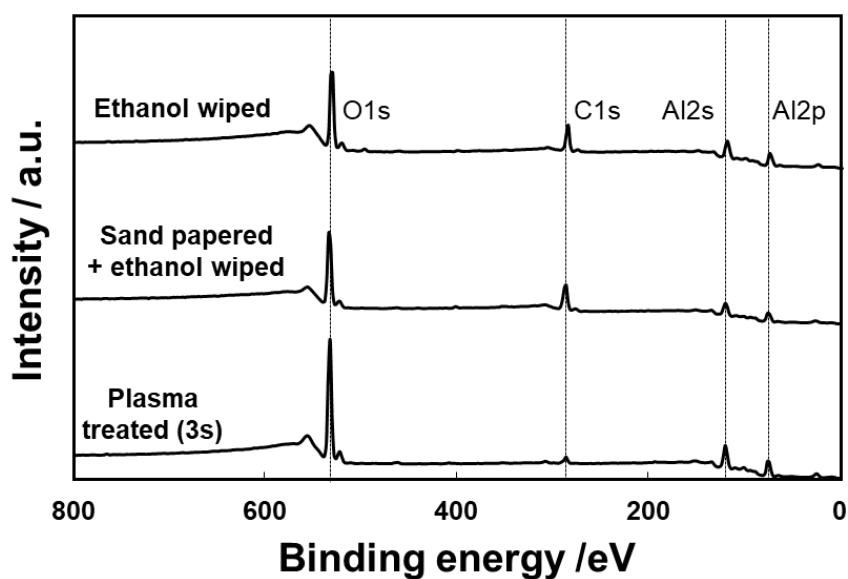


Fig. 2.6 Wide XPS profile of the ethanol wiped, sand papered + ethanol wiped, and plasma-treated (3s) Al substrate.

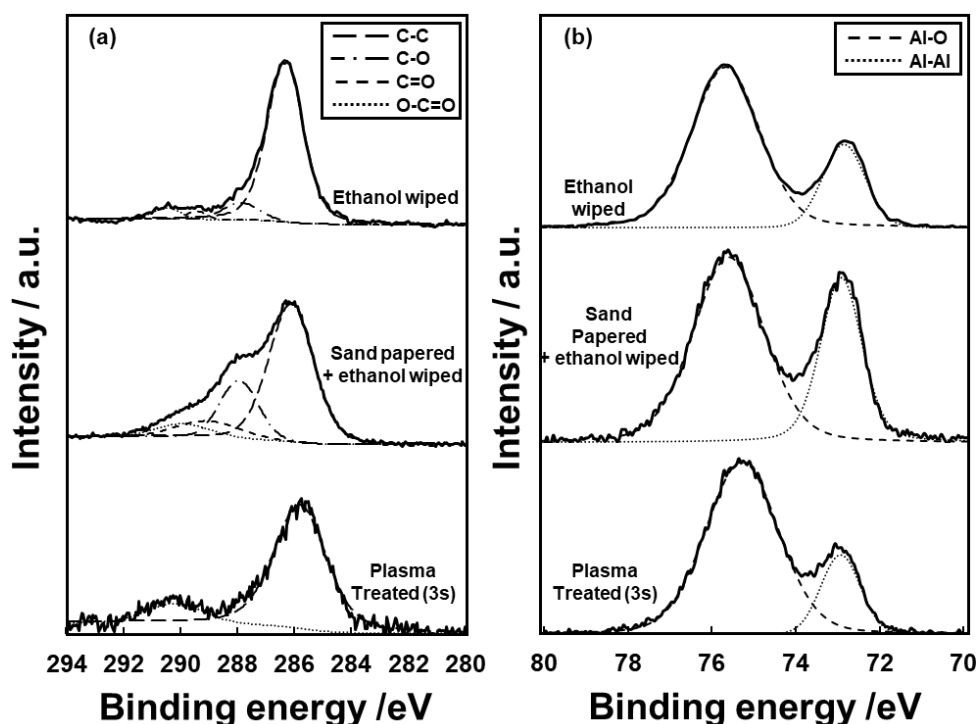


Fig. 2.7 XPS profile of (a) C1s and (b) Al2p binding energy peaks of ethanol treated, sand papered + ethanol treated, and plasma-treated (3s) Al substrate.

wiped specimens, while only two kinds of C binding energy peaks were included in the C 1s peak in the plasma-treated specimen. The C=O and C-O peaks were not observed from the plasma-treated specimen. Al-O and Al-Al binding energy peaks were observed in the Al 2p peaks in all the specimens. The Al-O binding energy peak was derived from Al_2O_3 or AlOOH .

2.4. Discussion

The C and Al-O binding energy peaks in **Fig. 2.7** are considered as organic impurities and Al oxide on the Al substrate, which can affect the wettability between the liquids and the Al substrate. To compare relative elemental composition on the Al substrate surface after each treatment, the integral intensity of the C binding energy peaks area and Al-O binding energy peak were divided by the integral intensity of the Al-Al binding energy peak and shown in **Fig. 2.8**. It was revealed that Al oxide increased after the atmospheric plasma treatment, which was in accordance with other reports [2.1, 2.3]. It is considered that activated oxygen species supplied from the plasma head contributed to the surface oxidation [2.3]. The surface energy of the Al surface might increase due to O atoms in the Al oxide. The O atoms in the Al oxide might also form hydrogen bonding with liquids, in turn decreased the surface energy at the interface of liquid/solid. Another important finding was that the amount of carbon decreased significantly, which demonstrates the excellent cleaning ability of the plasma treatment. The activated oxygen species reacted with the impurities and formed volatile chemical compound such as CO_2 and H_2O

[2.4]. The decrease in the surface contaminants increased the surface energy of Al substrate. In short, it is thought that the improvement of wettability after the plasma treatment stems from the surface cleaning and formation of Al oxides [2.1].

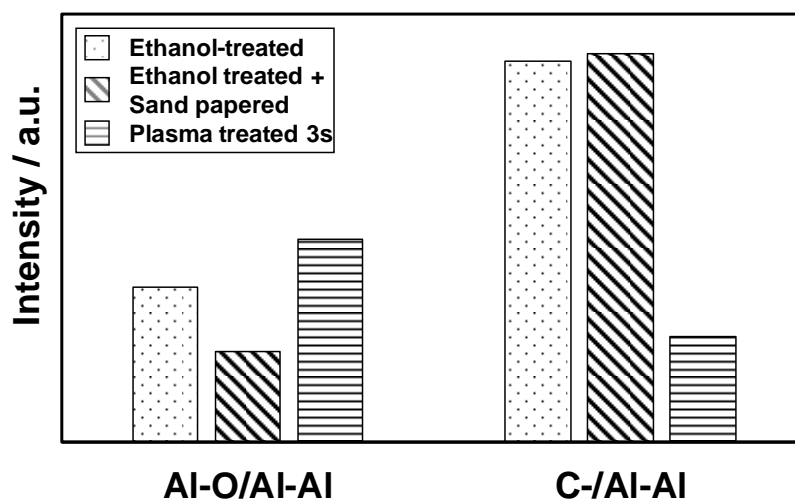


Fig. 2.8 Intensity of Al-O and C- bonding peaks area divided by Al-Al peak area with various surface treatments.

The wettability of water and epoxy resin with the Al surface increased after ethanol wiping and sand papering. It is thought that ethanol wiping removed significant amount of the surface contaminants, which might result in increasing the surface tension of Al substrate and decreasing the surface tension between the Al substrate and liquids. The sand papered + ethanol wiped Al substrate indicated almost the same amount of C binding energy peak, therefore, different mechanism worked for increasing the wettability. It is thought that roughening the surface increased the surface area and increased the surface energy of the solid. As a result, the wettability improved.

2.5. Summary

- The wettability of Al substrate increased by ethanol wiping, sand papering, and atmospheric plasma treatment.
- The ethanol wiping increased the wettability by reducing organic impurities on the surface. The sand papering increased roughness of the Al substrate, and the wettability increased. The atmospheric plasma treatment showed a significant effect on the wettability.
- The XPS analysis revealed that impurities were remarkably removed, and Al oxide was increased by the plasma treatment. As a result, the wettability between liquid phases and the Al substrate increased.

References

- [2.1] Bónová, L., Zahoranová, A., Kováčik, D., Zahoran, M., Mičušík, M., Černák, M. Atmospheric pressure plasma treatment of flat aluminum surface. *Applied Surface Science*. 2015, 331, 79-86.
- [2.2] Li, H., Belkind, A., Jansen, F., Orban, Z. An in situ XPS study of oxygen plasma cleaning of aluminum surfaces. *Surface and Coatings Technology*. 1997, 92(3), 171-177.
- [2.3] Kim, M. C., Song, D. K., Shin, H. S., Baeg, S. H., Kim, G. S., Boo, J. H., Han, J. G., Yang, S. H. Surface modification for hydrophilic property of stainless steel treated by atmospheric-pressure plasma jet. *Surface and coatings Technology*. 2003, 171(1-3), 312-316.
- [2.4] Li, H., Belkind, A., Jansen, F., Orban, Z. An in situ XPS study of oxygen plasma cleaning of aluminum surfaces. *Surface and Coatings Technology*. 1997, 92(3), 171-177.

3. Manufacturing process of an anchor layer through laser-induced in-situ reaction for joining Al alloy and PA6 substrates.

3.1. Introduction

It is necessary to establish a method for producing the anchor layer on the Al substrate. One potential route to fabricate the anchor layer is utilizing powder metallurgical process. Omura et al. [3.1] fabricated TiC dispersed Al matrix composite through a powder metallurgical process using the combustion reactions of Ti-C and Al-Ti systems. Al molar ratio in the Al-Ti-C powder mixture was controlled while Ti/C molar ratio was fixed at 0.95. A porous material was obtained when the Al molar ratio was 1.0. Kobashi et al. [3.2] produced porous material utilizing combustion foaming process between Al and Ti powder. The effects of Al/Ti molar ratio and exothermic agent on the morphology of the porous material were investigated. When these reactions were induced on Al substrate, the anchor layer which has porous morphology is expected to be additively manufactured because the reaction heat will be used for bonding the anchor layer with the substrate. In this chapter, combustion reactions for Al-Ti-C and Al-Ti systems were used to fabricate the anchor layer on an Al alloy (A5052) substrate. Al powder alone was also used for comparison. Laser was utilized as a heat source because laser can locally heat the powder while minimizing heat affection to the substrate. The produced anchor layers were characterized regarding structure, microstructure, and constituent chemical compounds. The Al substrate with the anchor layer was joined with a PA6 substrate by hot-pressing. Mechanical behaviors of the Al/PA6 lap joints were studied using joint strength and fractography. An appropriate powder for fabricating anchor layer exhibiting strong joint with polymers was discussed using above results.

3.2. Experimental methods

Three kinds of starting powders were blended using Al (< 45 μm , purity 99.99%), Ti (< 45 μm , purity 99.9%), and C (\approx 5 nm, purity 98%) powders. Al-Ti (molar ratio of 1:1) and Al-Ti-C (molar ratio of 1:1:1) powders were wet mixed with ethanol. The reason why these powders and compositions were selected is stated in the Appendix A. For comparison, Al powder alone was also wet stirred with ethanol to standardize conditions. Each starting powder was located without compaction on the Al substrate in a rectangular shape. The length, width, and height of the bedded powder mixture were about 15 mm, 5mm, and 50 μm , respectively. The dimension of the Al substrate was 50 mm \times 20 mm \times 1 mm. The laser pulse frequency, wavelength, beam diameter on the work plane and pulse length were adjusted to be 1 kHz, 970 nm, 1.2 mm and 0.7 ms, respectively. Laser power and scan speed were 400 W and 40 mm/s, respectively. The laser scanned for 10 mm on the bedded powder in atmospheric circumstance. Unreacted powders were

removed by ultrasonic cleaning with water. The anchor layer was observed with the SEM from the laser irradiation direction (top-view). The area of each anchor layer was quantified by image analysis.

The anchor layer was cured in the epoxy resin. The cured samples were cut along the laser scanning direction to expose cross-section of the anchor layer. The cross-sectioned sample was polished using # 320, 800, 1200 and 2400 emery papers and buffed with 6 and 3 μm diamonds slurries, followed by platinum deposition for preventing the charge-up. The cross-sectioned anchor layer was observed using the SEM (back scattered electron mode). X-ray diffraction (XRD) analysis was carried out with Cu-K α radiation at 40 mA and 40 kV for identifying constituent chemical compounds of the anchor layer. The scanning rate was a speed of 4 $^\circ/\text{min}$ in the range of $2\theta = 30^\circ \sim 90^\circ$. Energy dispersive X-ray spectroscopy (EDS) analysis was carried out with the cross-sectioned anchor layer to obtain elemental distribution of Al, Ti and C. The anchor layer produced with Al-Ti-C powder was chemically etched using 20% NaOH aqueous solution. Vinod kumar et al. [3.3] fabricated Al-Ti-C alloy by casting. The Al matrix was dissolved by NaOH aqueous solution leaving chemical products from Al-Ti-C reaction. After etching, the anchor layer was observed with the SEM.

A pre-molded PA6 substrate was used as polymer material for fabricating Al/polymer lap joint samples via the anchor layers fabricated with the Al-Ti-C, Al-Ti, and Al starting powders. The dimension of PA6 substrate was 50 mm \times 20 mm \times 3 mm. The Al and PA6 substrates were joined using a hydraulic hot press. The joining process is schematically described in Fig. 3.1 (a). The Al substrate with the anchor layer was put on the hot plate heated at 215 $^\circ\text{C}$, which was below the melting point of PA6 (220 $^\circ\text{C}$). The PA6 substrate was put on the Al substrate so as to sandwich the anchor layer. Pressure of 1.8 MPa was adopted to infiltrate the polymer into the anchor layer while keeping the hot plate temperature at 215 $^\circ\text{C}$. The hot plate was cooled down

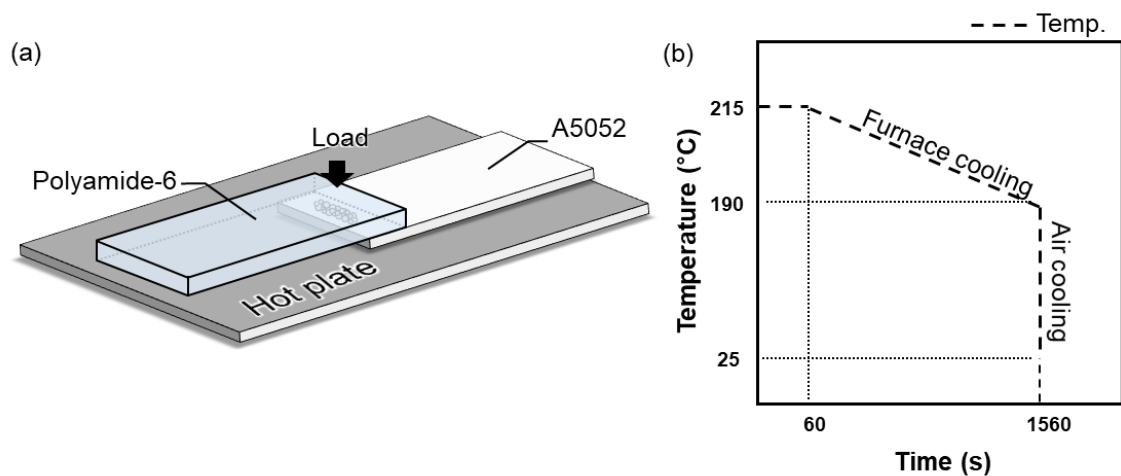


Fig. 3.1 (a) Schematically illustrated process for fabricating Al/PA6 lap joint and (b) joining temperature history.

to 190 °C while applying the pressure, followed by air cooling without pressure. Temperature history adopted to the Al/PA6 lap joint samples is shown in **Fig. 3.1 (b)**.

An Al/PA6 lap joint via the Al-Ti-C anchor layer was cross-sectioned and observed by an optical microscopy to ascertain the mechanical interlocking between the anchor layer and PA6. **Figure 3.2** shows the photo image of the anchor layer fabricated Al substrate and an Al/PA6 lap joint.

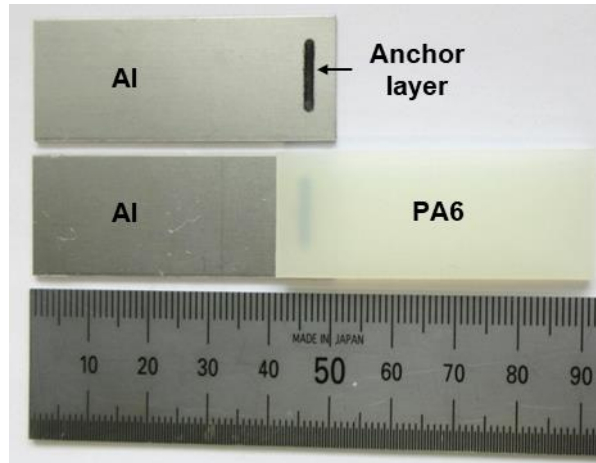


Fig. 3.2 Photography image of an anchor layer on the Al substrate and an Al/PA6 lap joint.

Lap shear tests were carried out to measure the joint strength using a universal testing machine. The tests were carried out at room temperature (25 °C) with a crosshead speed of 1 mm/min. The dimension of fabricated Al/PA6 lap joint for the shear test is indicated in **Fig. 3.3**. Alignment pads were used to align the center axis of the jig during the shear test. The ultimate shear force (joint strength) was measured from force-stroke curves. Three lap joint samples via each type of the anchor layer were tested to obtain average ultimate shear force. After the lap

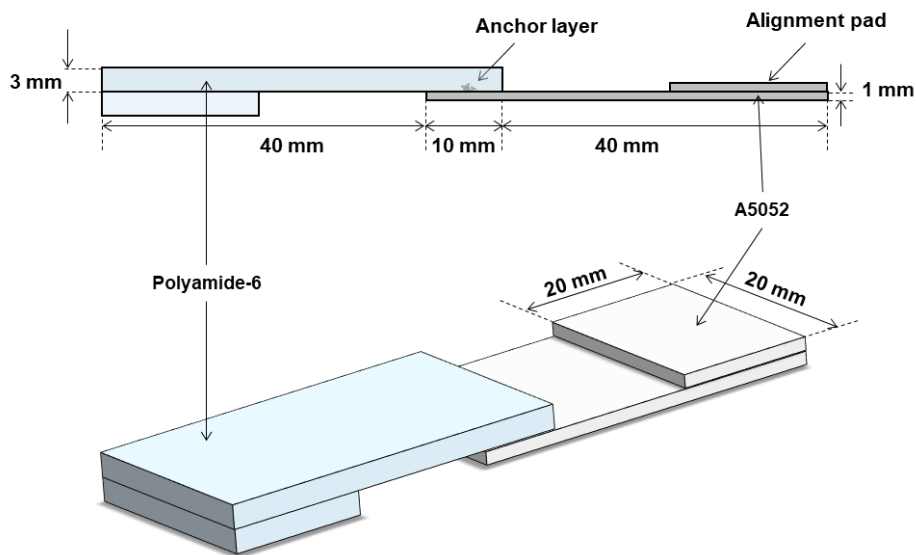


Fig. 3.3 Schematically illustrated Al/PA6 lap joint for shear tests.

shear tests, fracture surfaces on Al alloy side were deposited with platinum and observed with the SEM.

3.3. Results

3.3.1. Characterization of the anchor layer

Representative SEM images of the anchor layers formed with different starting powder are shown in **Fig. 3.4**. When the Al powder was used, granular protrusions with 200 ~ 600 μm size were produced on the Al substrate. The magnified image of the protrusion indicated that its surface was smooth. On the cross-sectioned anchor layer, the microstructure was homogeneous. The anchor layer and Al substrate were well-bonded.

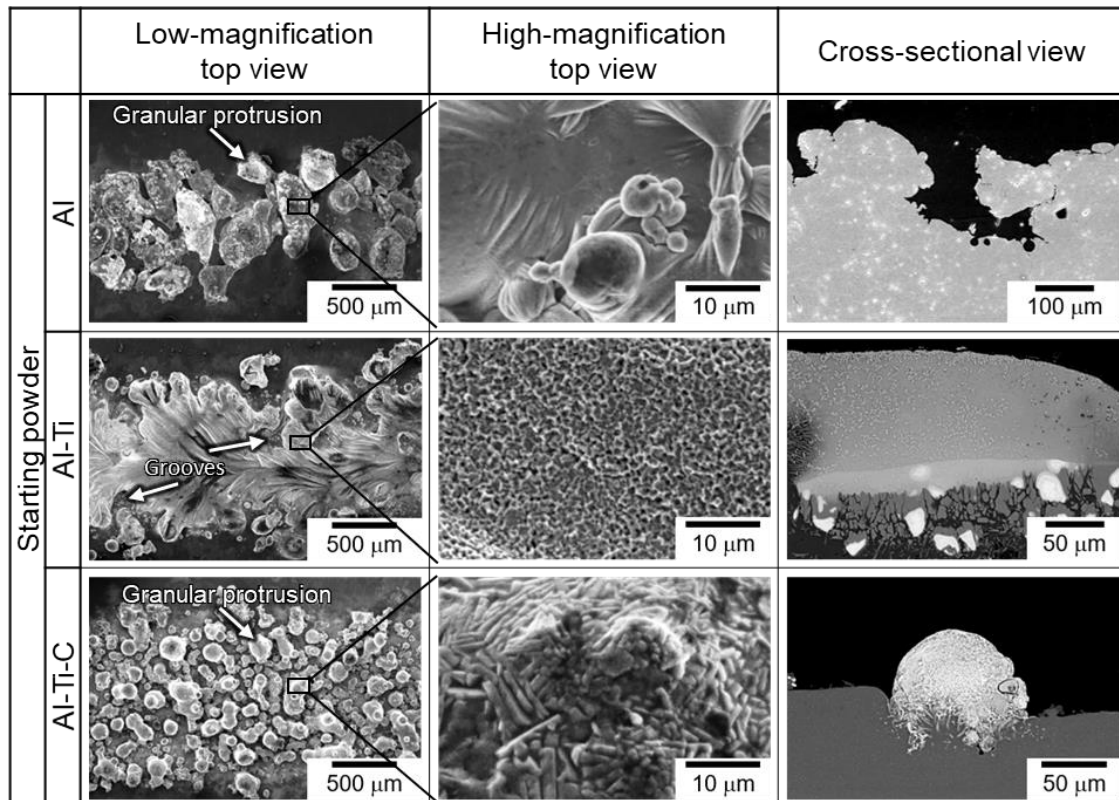


Fig. 3.4. SEM micrographs of top-view and cross-sectioned anchor layer formed with different starting powders.

A dense layer was produced on the laser irradiated region when the Al-Ti starting powder was used. In the dense layer, groove-like structures were formed as indicated by the white arrows. The magnified surface of the dense layer indicated that rough surface was generated on the dense layer. Various phases with different contrast was formed and the dense layer was well-bonded with the Al substrate as indicated in the cross-sectional view of the anchor layer.

When the Al-Ti-C powder was used, many granular protrusions with < 400 μm size were generated on the Al substrate. High-magnification image of the anchor layer shows that the

surface of the granular protrusion was rough. The cross-section view of the anchor layer shows that small grains with bright contrast dispersed in the granular protrusions. The grains were also formed below the interface between the granular protrusion and Al substrate, suggesting that the granular protrusions were firmly bonded with the Al substrate.

Figure 3.5 shows the XRD profiles of the Al-Ti and Al-Ti-C anchor layers. The final products of the Al-Ti combustion reaction from the Al-Ti powder with equimolar composition are Al-Ti phases [3.4]. Al and TiC phases are the final product from the Al-Ti-C powder reaction [3.1]. α -Ti and Al-Ti phases (Al_3Ti , AlTi, and AlTi_3) were confirmed in the case of the Al-Ti anchor layer. The TiN phase peaks were also detected, which was originated from Ti-N (N_2 from air) reaction. The α -Al, Al_3Ti , and TiC phases were detected in the case of the Al-Ti-C anchor layer.

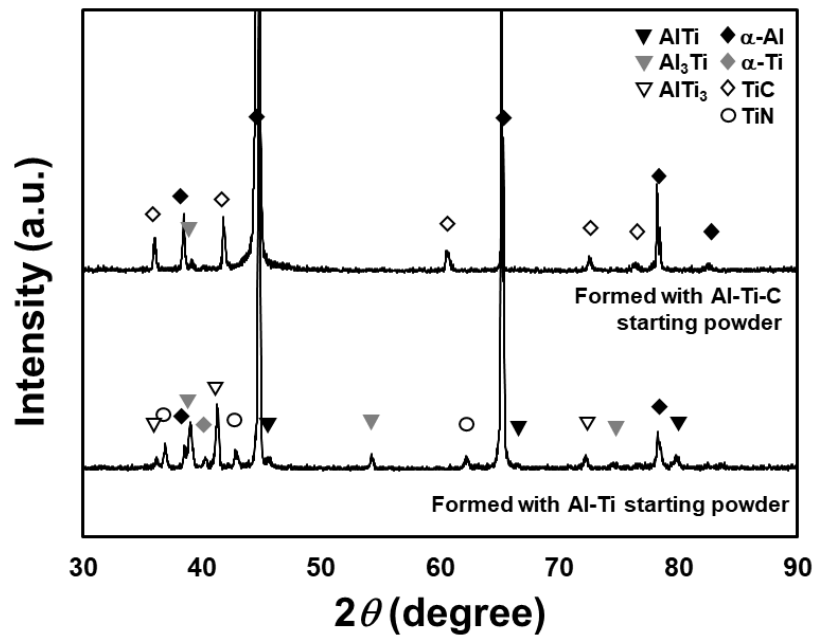


Fig. 3.5 XRD profiles of anchor layers formed with different starting powders.

Figure 3.6 shows the SEM micrographs and element maps (Al and Ti elements) of the cross-sectioned Al-Ti anchor layer. In the magnified SEM image, the phase in the bottom region with brightest contrast was α -Ti since only Ti element was detected. The α -Ti phases were encompassed by an Al-rich Al-Ti compound, which is regarded as Al_3Ti judged from the XRD profile. The Al_3Ti phase was elongated in a downward direction in the figure, i.e., toward the substrate. Ti-rich phases were found in the upper region. These phases were regarded as AlTi or AlTi_3 judged from XRD results. The Al-Ti anchor layer consisted of α -Ti and several Al-Ti compounds.

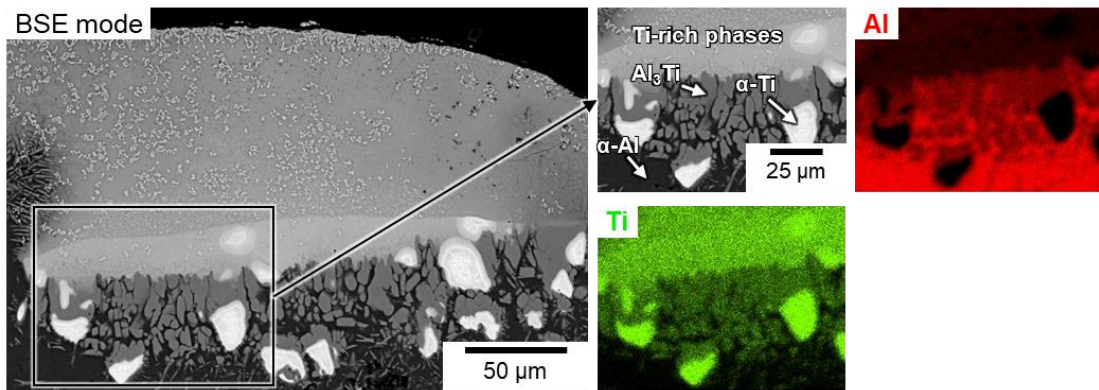


Fig. 3.6 SEM micrographs and EDS element maps of Al and Ti in cross-sectioned Al-Ti anchor layer.

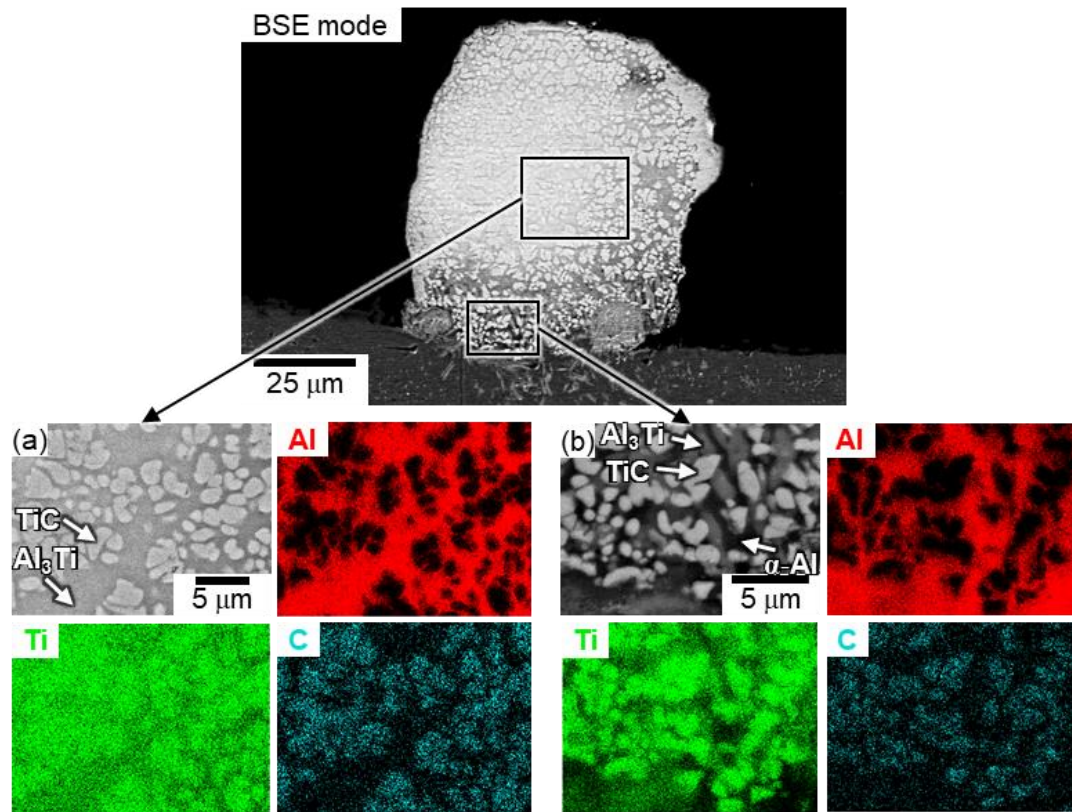


Fig. 3.7 SEM micrographs and EDS element maps of Al, Ti, and C in cross-sectioned Al-Ti-C anchor layer: (a) middle region and (b) region near the substrate.

Representative SEM micrograph and elements maps (Al, Ti, and C) of the cross-sectioned Al-Ti-C anchor layer is shown in **Fig. 3.7**. In the granular protrusion, the middle region and the region near the substrate were magnified in **Fig. 3.7 (a)** and **(b)**. As indicated in **Fig. 3.7 (a)**, two phases were observed in the middle region. The phase with brightest contrast was TiC because the C and Ti elements were detected. The TiC phase was encompassed by an Al-Ti

compound, which was Al_3Ti judged from the XRD result. As shown in **Fig. 3.7 (b)**, three phases were observed in the near substrate region. The brightest phase was TiC phase because the C and Ti elements were detected. The Al and Ti elements were detected in the phase with middle contrast, which was regarded as the Al_3Ti phase judged from the XRD result. The TiC and Al_3Ti phases were formed in the granular protrusion and around the interface between the Al substrate and granular protrusion. The phase with darkest contrast was $\alpha\text{-Al}$ because only Al element was detected. The Al-Ti-C anchor layer consisted of the $\alpha\text{-Al}$, Al_3Ti and TiC phases.

Figure 3.8 shows the Al-Ti-C anchor layer after etching with NaOH aqueous solution. A severely etched granular protrusion is shown in **Fig. 3.8 (a)**. The granular shape was maintained even after etching treatment. The surface of the etched protrusion was magnified in **Fig. 3.8 (b)**. The surface was porous structure, indicating that chemical compounds produced by powder reaction were connected to one another forming a skeleton structure in the granular protrusion.

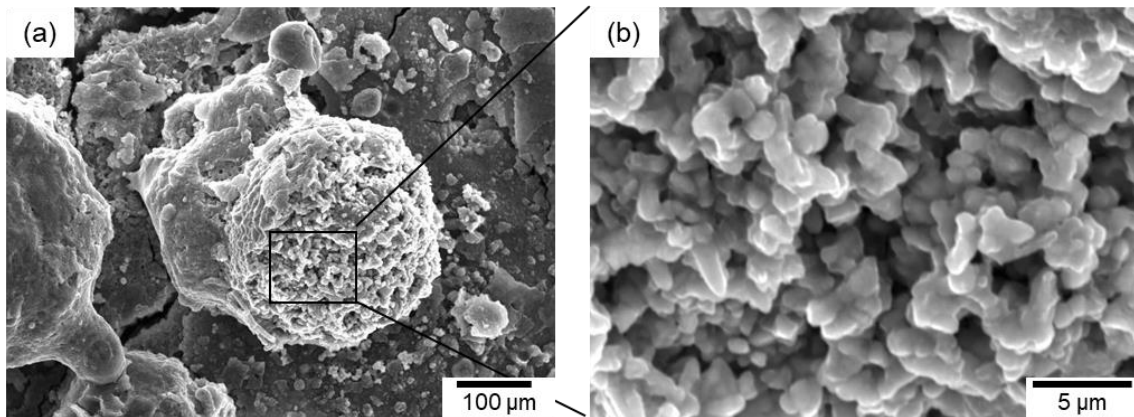


Fig. 3.8 SEM micrographs of (a) low and (b) high magnification granular protrusion etched with NaOH solution.

3.3.2. Characteristics of Al/PA6 lap joints

Representative cross-sectional view of an Al/PA6 lap joint is shown in **Fig. 3.9**. The joint was the Al-Ti-C anchor layer. Granular protrusions were observed and interlocked with PA6. No gaps were found at the interface between the anchor layer and PA6 substrate, indicating that PA6 well infiltrated into the anchor layer.

Representative shear force - stroke curves obtained from the lap shear tests of Al/PA6 joints via each anchor layer are shown in **Fig. 3.10 (a)**. The average ultimate shear force and stress of Al/PA6 lap joint is indicated in **Fig. 3.10 (b)**. To obtain the average ultimate shear stress, the average ultimate shear force was divided by the areas of Al-Ti-C, Al-Ti, and Al anchor layers, which were 17.9, 14.4, and 9.21 mm^2 , respectively. Error bars represent the difference between minimum and maximum values of three tests for each joint. When the Al/PA6 lap joint was formed via the anchor layer produced with Al powder, the ultimate shear force was the lowest and the

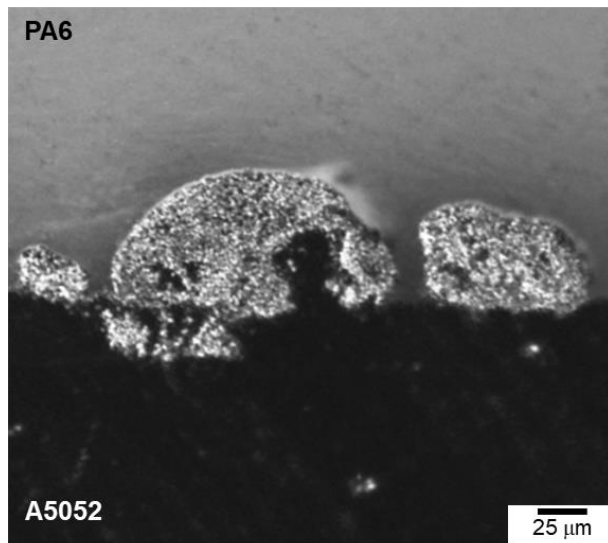


Fig. 3.9 Optical microscopy image of the cross-sectioned Al/PA6 lap joint via the Al-Ti-C anchor layer.

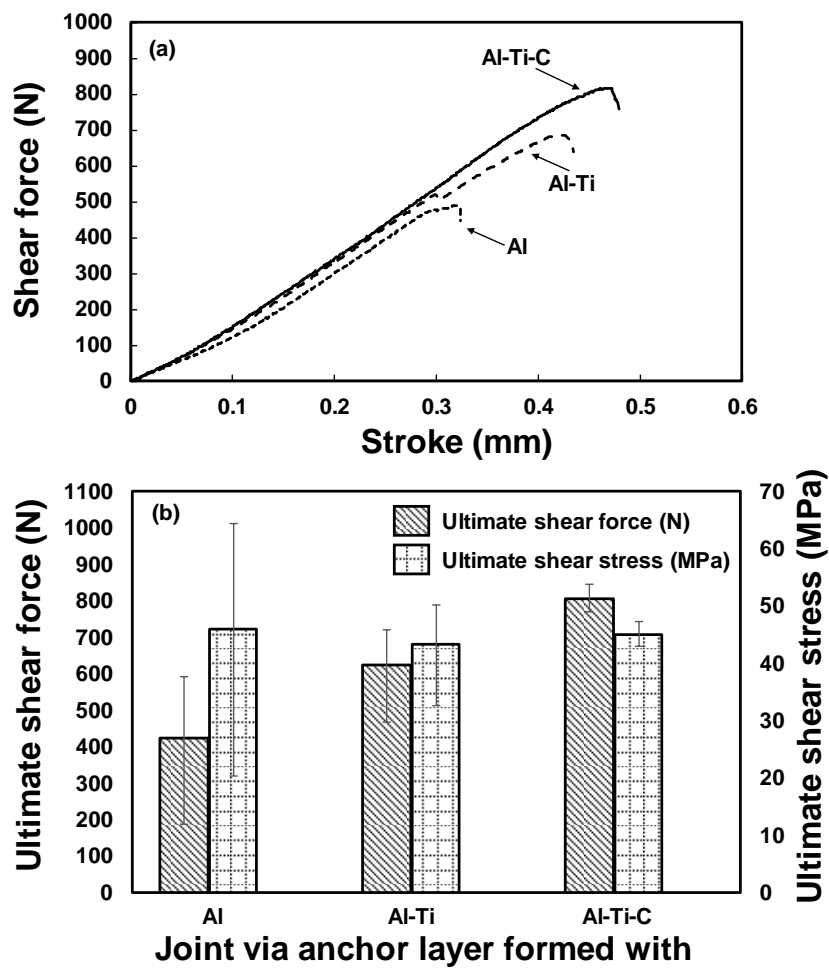


Fig. 3.10 (a) representative shear force-stroke curves and (b) average ultimate shear force of Al/PA6 lap joints formed via each anchor layer.

range of the error bar was the highest. When the joint was fabricated via the Al-Ti-C anchor layer, the ultimate shear force increased significantly and the range of error bar was the lowest. In the case of the ultimate shear stress, almost same value was obtained from all kinds of anchor layers. These results indicated that Al/PA6 lap joint fabricated via the Al-Ti-C anchor layer shows high joint strength and reliable mechanical property.

Figure 3.11 shows SEM images indicating the top-view of the anchor layer before joining and the corresponding fracture surface on Al substrate side after the lap shear tests. When the anchor layer produced with Al powder was used for joining with the PA6 substrate, most of the protrusions fractured. The granular protrusions remained on the Al surface were plastically deformed (indicted by white arrows in the SEM image after shear test) in the same direction in which the PA6 substrate was pulled (black arrow in white box). PA6 did not remain on the fracture surface, which indicates that the anchor layer was not strong enough to hold PA6 on the substrate.

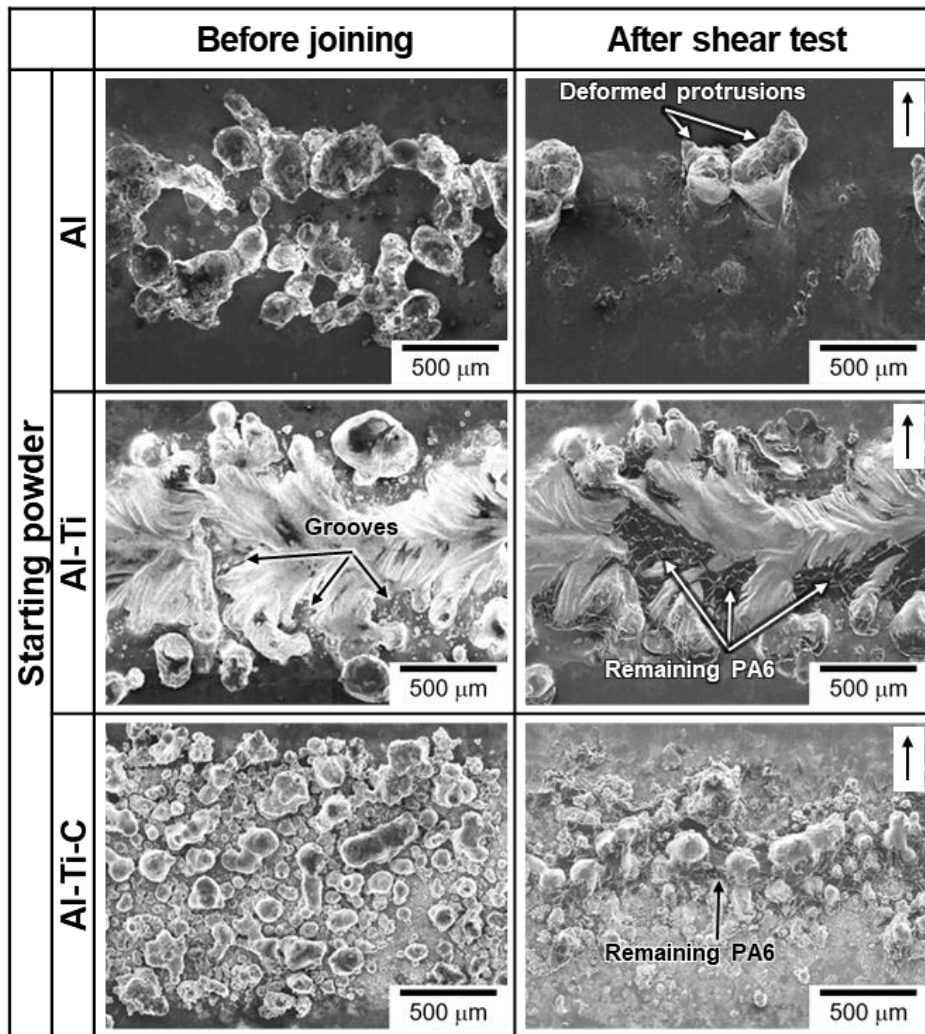


Fig. 3.11. SEM micrographs of the anchor layers before joining and corresponding fracture surfaces (the direction of applied force is indicated in the white box).

When the Al-Ti anchor layer was used, the dense layer remained on the Al substrate. On the fracture surface, PA6 remained (indicated by white arrows in the SEM image after shear test) in the groove-like structures (indicated by black arrows in the SEM image before joining). However, PA6 did not remain on the surface of the dense layer.

In the case of the Al-Ti-C anchor layer, the granular protrusions remained on the Al substrate. PA6 remained among granular protrusions (indicated by black arrow in the SEM image after shear test), indicating PA6 and granular protrusions well interlocked each other.

3.4. Discussion

3.4.1. Characterization of anchor layer

When the Al powder was used, large granular protrusions were produced along with the laser-irradiated region on the Al substrate (**Fig. 3.4**). It was reported that so-called balling phenomenon of molten metals occurs on metal substrates during laser irradiation under specific laser condition because of shrinking tendency and poor wettability between the substrate and molten metal [3.5]. The balling phenomenon could cause the formation of granular protrusions with Al powder in the present study.

The dense layer was formed when the Al-Ti starting powder was used (**Fig. 3.4**). Yang et al. [3.6] demonstrated that wettability between the ceramic substrate and liquid metal was improved by interfacial chemical reaction. The formation of elongated Al-rich phase toward the Al substrate region demonstrated the Al-rich phase was formed by reaction between the Ti powder and Al substrate (**Fig. 3.6**). The interfacial reaction between the Ti powder and Al substrate improved wettability between the anchor layer and Al substrate and preferentially generated dense layer rather than the granular protrusions.

The addition of C powder significantly changed the constituent phase and morphology of the anchor layer. In addition to the Al-Ti intermetallic compound (Al_3Ti), the TiC phase was newly formed and thought to be responsible for the change in the morphology of the anchor layer. The TiC phase formed the skeleton structure in the granular protrusion (**Fig. 3.8**). However, the reason why the TiC phase had connected each other as the skeleton structure rather than dispersed as particles required to be investigated. The Al_3Ti and TiC phases were produced not only in the granular protrusions and below the interface between the granular protrusion and Al substrate (**Fig. 3.7**). The granular protrusion and Al substrate were firmly bonded, which stems from the interfacial reaction between molten powders and the Al substrate.

3.4.2. Mechanical behaviors of Al/PA6 lap joints

The anchor layer produced with Al powder indicated metallic bonding with the Al substrate and homogeneous microstructure was observed (**Fig. 3.4**). The joint strength was the

lowest in the joints in this study (**Fig. 3.10**). When external shear force was adopted to the Al/PA6 lap joint, the anchor layer could not resist it. The poor mechanical strength of the granular protrusion resulted in the deformation and fracture of the granular protrusions.

When the Al and PA6 substrates were joined via the Al-Ti anchor layer, the joint strength was improved (**Fig. 3.10**). The PA6 remained in the groove-like structure, indicating that the anchor effect acted in the groove-like structure. The anchor layer remained on the Al substrate after the lap shear test, which was derived from the formation of Al-Ti chemical compounds around the interface (**Fig. 3.6**). Al-Ti intermetallic compounds indicate higher strength and elastic modulus compare to pure Al [3.7]. The anchor layer was able to resist higher external shear force, resulting in higher joint strength.

In the case of the Al/PA6 lap joint via the Al-Ti-C anchor layer exhibited the highest joint strength (**Fig. 3.10**). The high joint strength was derived from the homogeneously distributed granular protrusions. A number of granular protrusions interlock with PA6 and exhibited the anchor effect. The TiC and Al₃Ti phases were observed at the interface between the granular protrusions and Al substrate (**Fig. 3.7 (b)**), which allowed the anchor layer to resist high external shear force without failure, contributing to higher joint strength.

The joint strength difference between maximum and minimum value was relatively low in the Al/PA6 lap joint via the Al-Ti-C anchor layer. It is considered that the homogeneously distributed granular protrusions were responsible for the high reliability. It can be seen that the granular protrusions in the anchor layer produced with Al powder were not distributed homogeneously (**Fig. 3.4** and **3.11**). The groove-like structures in the Al-Ti anchor layer were randomly formed (**Fig. 3.4** and **3.11**). It is thought that these randomly formed structures in the anchor layers were responsible for the large difference between maximum and minimum joint strength.

Seong et al. [3.8] carried out experiments with adhesively bonded Al/CFRP lap joints to investigate the effects of the configurations of the lap joints, such as adherend thickness, overlap length, and bonding pressure, on the joint strength. The joint strength in [MPa] unit and failure load in [N] unit were used to evaluate the mechanical behavior of the joints. The joint strength in [MPa] unit was derived by dividing the failure force [N] by the overlap area [mm²]. **Figure 3.12** shows changes in the joint strength and failure load with the overlap length. The joint strength decreased with increasing the overlap length. The failure force is not linearly proportional to the overlap length. These facts suggest that the same area needs to be used for comparison with different kinds of anchor layers. The ultimate shear stress values of the joints via the Al, Al-Ti, and Al-Ti-C anchor layers were almost same. Consider that the area of the Al-Ti-C anchor layer was the largest, the Al-Ti-C anchor layer exhibited the highest efficiency. It is thought that the external stress was efficiently distributed through the Al-Ti-C anchor layer. Therefore, it is the

most suitable for joining with the polymer substrate. The ultimate shear stress of the Al/PA6 joint was approximately 45 MPa. Consider that automobile company requires more than 20 MPa in shear strength [3.9], the joining metal and polymer via the anchor layer in this study is thought to be efficient.

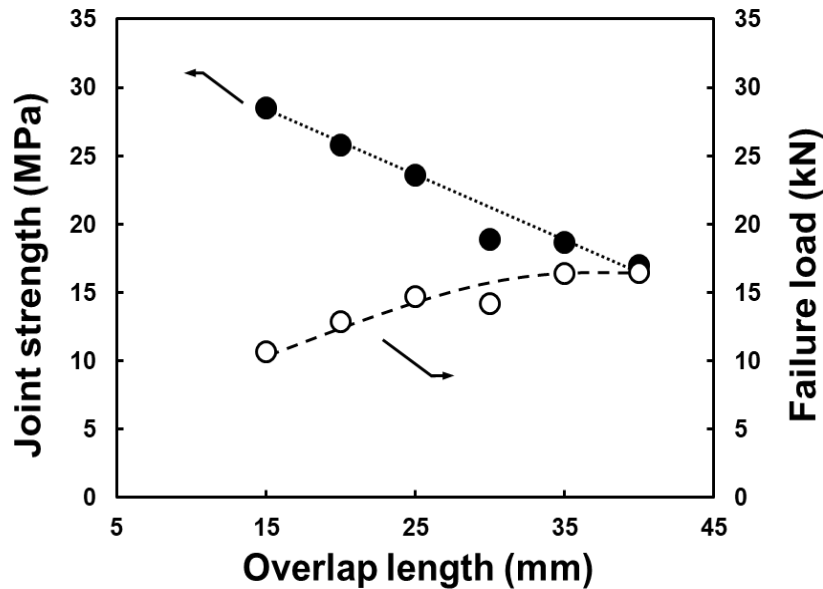


Fig. 3.12. Changes in the joint strength and failure load with overlap length of adhesively bonded Al/CFRP joints [3.8].

3.5. Summary

- The anchor layer produced with Al-Ti-C starting powder consisted of homogeneously distributed granular protrusions.
- Al_3Ti and TiC phases were detected in the granular protrusions and around the interface between the granular protrusions and Al substrate.
- When the Al and PA6 substrates were joined via the Al-Ti-C anchor layer the joint strength was the highest. Homogeneously distributed granular protrusions in the anchor layer interlocked with PA6.
- The Al_3Ti and TiC phases reinforced granular protrusions and allowed the anchor layer resist high external shear force. These chemical products formed in the granular protrusions prevented the deformation of the anchor layer, resulting in high joint strength.

References

- [3.1] Omura, N., Kobashi, M., Choh, T., Kanetake, N. Synthesis of TiC Particle Reinforced Aluminum Composite by Reactive Infiltration Process. Japan Institute of Metals and Materials. 2002, 66(12), 1317-1324.

- [3.2] Kobashi, M., Inoguchi, N., Kanetake, N. Effect of elemental powder blending ratio on combustion foaming behavior of porous Al–Ti intermetallics and Al₃Ti/Al composites. *Intermetallics*. 2010, 18(5), 1039-1045.
- [3.3] Kumar, G. V., Murty, B. S., Chakraborty, M. Development of Al–Ti–C grain refiners and study of their grain refining efficiency on Al and Al–7Si alloy. *Journal of Alloys and Compounds*. 2005, 396(1-2), 143-150.
- [3.4] Kobashi, M., Miyake, S., Kanetake, N. Hierarchical open cellular porous TiAl manufactured by space holder process. *Intermetallics*. 2013, 42, 32-34.
- [3.5] Li, R., Liu, J., Shi, Y., Wang, L., Jiang, W. Balling behavior of stainless steel and nickel powder during selective laser melting process. *The International Journal of Advanced Manufacturing Technology*. 2012, 59(9-12), 1025-1035.
- [3.6] Yang, J., Huang, J., Ye, Z., Chen, S., Ji, R., Zhao, Y. Influence of interfacial reaction on reactive wettability of molten Ag-Cu-X wt.% Ti filler metal on SiC ceramic substrate and mechanism analysis. *Applied Surface Science*. 2018, 436, 768-778.
- [3.7] Ward-Close, C. M., Minor, R., Doorbar, P. J. Intermetallic-matrix composites—a review. *Intermetallics*. 1996, 4(3), 217-229.
- [3.8] Seong, M. S., Kim, T. H., Nguyen, K. H., Kweon, J. H., Choi, J. H. A parametric study on the failure of bonded single-lap joints of carbon composite and aluminum. *Composite structures*. 2008, 86(1-3), 135-145.
- [3.9] Kimura, F., Yamaguchi, E., Horie, N., Suzuki, G., Kajihara, Y. Formation of boehmite crystals on microblasted aluminum surface to enhance performance of metal–polymer direct joining. *Materials Letters*. 2020, 260, 126963.

4. Influence of joining thermal history during hot-pressing on the mechanical behaviors of the Al/PA6 lap joints

4.1. Introduction

Many studies used semi-crystalline polymers as joining materials as mentioned in sections 1.3.1 and 1.3.2. The mechanical properties of semi-crystalline polymers are determined by crystalline characteristics. Polymer fabrication processes greatly influence the crystalline properties. Fornes et al. [4.1] studied crystallization behaviors using PA6 bulk specimens produced by injection molding. The crystal structure and degree of crystallinity were different in core and skin regions of the injection molded specimens because the cooling rate was differed by the core (higher cooling rate) and skin region (slow cooling rate). Tensile tests were carried out with various PA6 films (α -, γ - and β -PA6) by Miri et al. [4.2]. The α -PA6 and γ -PA6 are the crystalline phases of PA6 and the β -PA6 is the amorphous phase of PA6. The α -PA6 indicated the highest yield stress, while β -PA6 showed the lowest yield stress. Yang et al. [4.3] fabricated PEEK specimens by 3D printing process. It was reported that the elastic modulus and tensile strength rose with an increase in the degree of crystallinity. The degree of crystallinity is determined by the ratio of the amorphous and crystalline phases. These findings can also be adopted in the field of metal/polymer joining process involving high temperature for melting the polymer. When the molten polymer contacts with dimples or protrusions on the metal surface and solidifies, thermal conditions such as the temperature of the metal substrate and the cooling rate of the system influence on the crystalline properties of the polymer in the vicinity of metal.

In this study, the Al and PA6 substrates were joined by hot-pressing. The influence of joining thermal history on the crystalline properties of the PA6 and mechanical properties of Al/PA6 lap joint was investigated. The joining thermal history was controlled by changing the cooling rate (furnace cooling and air cooling) and the joining complete temperature. The changes in the degree of crystallinity and crystal phases according to the joining thermal histories were investigated using differential scanning calorimetry (DCS) and the XRD analysis. The mechanical properties of the Al/PA6 lap joints through different thermal histories were evaluated by the lap shear tests and discussed based on the above analyses and the fractography.

4.2. Experimental methods

4.2.1. Al/PA6 lap joint fabrication by hot-pressing

The process for producing the anchor layer was same as that explained in section 3.2. The anchor layer was fabricated with the Al-Ti-C powder blend with molar ratio of 1:1:1.

The Al and PA6 substrates were joined using a hot press. The PA6 substrate was dried in a vacuum chamber at 120 °C prior to the joining process. **Figure 4.1 (a)** indicates schematic

illustration of the hydraulic hot press machine. The machine composed of upper plate, sample stage, load sensor and hydraulic ram. The upper plate and the sample stage can be heated. Pressure is adopted by rising the hydraulic ram and the load is measured with the load sensor. **Figure 4.1 (b)** shows schematically illustrated joining process for fabricating the Al/PA6 lap joint. The sample stage was heated to 215 °C prior to the joining process. The preset temperature (215 °C) was chosen since the PA6 substrate collapsed badly when joined at the melting point of PA6 (220 °C). The Al substrate with the anchor layer and PA6 substrate were set on the heated sample stage as indicated in **Fig. 4.1 (b)**. The Al and PA6 substrates were pressured at 0.5 MPa, which was lower controllable pressure of the machine used in this study. The joining process using the anchor layer is available even at low pressure. After applying the pressure for 1 min (Pre-heating), it was cooled to desired temperatures (215, 210, 190, and 150 °C) while maintaining the pressure (furnace cooling). The desired temperature is defined as joining complete temperature (T_{JC}) in this study. When the temperature reached T_{JC} , the Al/PA6 lap joint was taken out from the machine and air-cooled to room temperature (25 °C). Same joint dimension as indicated in **Fig. 3.3** was used in this study.

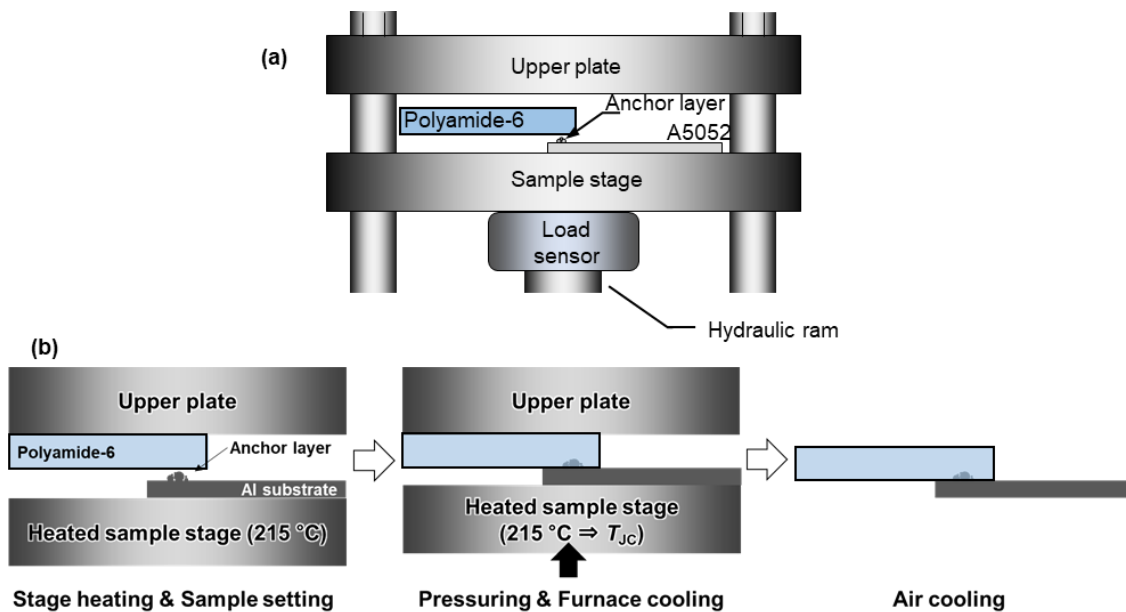


Fig. 4.1 Schematic illustration of the (a) hot-pressing machine and (b) the process for fabricating Al/PA6 lap joint.

The joining thermal history is described in **Fig. 4.2**. A thermocouple was used to record the change in the interfacial temperature between Al and PA6 substrate. The rates of furnace and air cooling were approximately 2 and 90 °C/min, respectively.

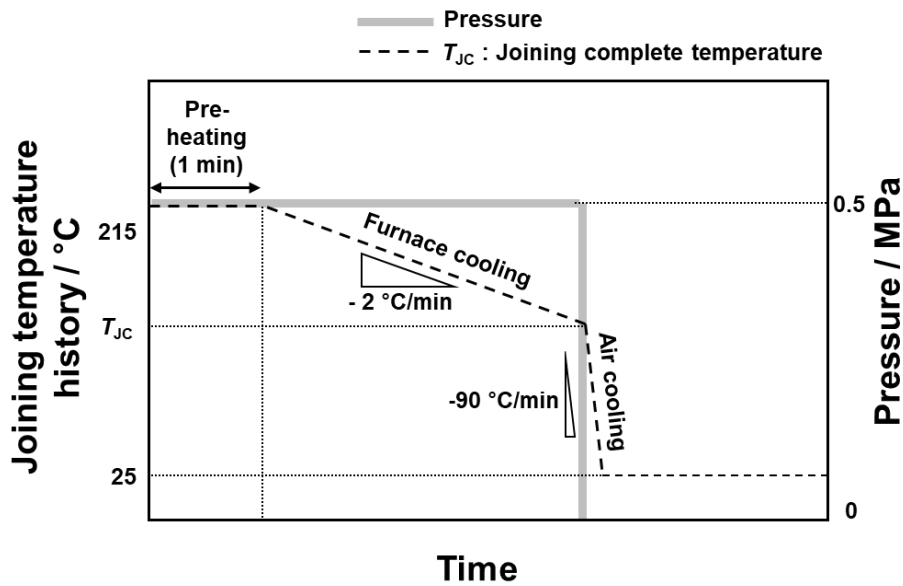


Fig. 4.2 Joining thermal history during the joining process.

4.2.2. Mechanical behaviors of Al/PA6 lap joint

Joint strength was measured as same method as explained in section 3.2. Four Al/PA6 lap joint samples were used to calculate average ultimate shear force for each T_{JC} . The average ultimate shear stress for each T_{JC} was not calculated since the anchor layer was fabricated with the Al-Ti-C powder only. Fracture surfaces on the Al substrate side were observed using the SEM. The shear test of a joint produced at T_{JC} of 190 °C was interrupted before the test piece was ruptured. The interrupted joint was cross sectioned to observe the crack propagation paths using the SEM.

4.2.3. Change in PA6 characteristics

PA6 films (30 μm in thickness) were used to examine the influence of joining thermal history on the crystal structures, degree of crystallinity, and Vickers hardness. The thin films were used since it was difficult to directly cut off PA6 from the PA6 substrate which underwent the thermal history applied for the joining process. The same temperature history as the process for fabricating joints mentioned in section 4.2.1 was applied to the PA6 films (about 6 mg). The crystal structures of the PA6 film were examined using the XRD. The scan was conducted at a rate of 1 $^{\circ}/\text{min}$ in the 2θ range of 10 - 30 $^{\circ}$ with Cu-K α radiation run with 40 kV and 40 mA. In general, γ - and α - (α_1 and α_2) forms of sharp peaks and β -form of a broad peak (amorphous) are observed in the PA6. DSC measurements were conducted to examine the degree of crystallinity of the PA6 films. The PA6 films were heated from 25 to 240 °C with a rate of 10 $^{\circ}\text{C}/\text{min}$ to obtain heating curves. The heating curves were used to obtain the heat of fusion (ΔH_f). The heating curves were integrated from 170 to 230 °C for calculating the ΔH_f . The ΔH_f was divided by the

heat of fusion of pure crystalline form (ΔH_f^0) to obtain the degree of crystallinity (X_c). According to Fornes et al. [4.1], ΔH_f^0 values of γ - and α -forms were 239 and 241 J/g, respectively.

$$X_c = \frac{\Delta H_f}{\Delta H_f^0} \times 100 \quad (5.1)$$

To investigate the change in mechanical characteristic of PA6, Vickers hardness tests were conducted with the PA6 films which underwent the thermal history applied for the process for fabricating joints mentioned in section 4.2.1. The indentation loading time and load were 15 s and 100 gf, respectively. The average value was calculated for each T_{JC} after the Vickers hardness tests were conducted for three times.

The effect of cooling rate on the crystallization behaviors was investigated using the DSC. As-received PA6 films (6 mg) were put in the DSC apparatus and heated to 240 °C. The PA6 films were maintained at 240 °C more than 300 s for stabilizing DSC scan curve. After the scan curve was stabilized, the films were cooled to 25 °C at rates of 2, 20, and 40 °C/min. The crystallization starts below the melting point of PA6 and the heat is generated during the crystallization. The generated heat was divided by the mass of PA6 to obtain enthalpy of crystallization.

4.3. Results

4.3.1. Mechanical behaviors of Al/PA6 lap joints

Representative shear force – stroke curves of joints are shown in **Fig. 4.3 (a)**. Each curve showed a yielding point (indicated the by the black arrows) which was consistent with the ultimate shear force. **Figure 4.3 (b)** shows the average ultimate shear force as a function of T_{JC} . Error bars indicate the difference between the minimum and maximum values. The ultimate shear force was

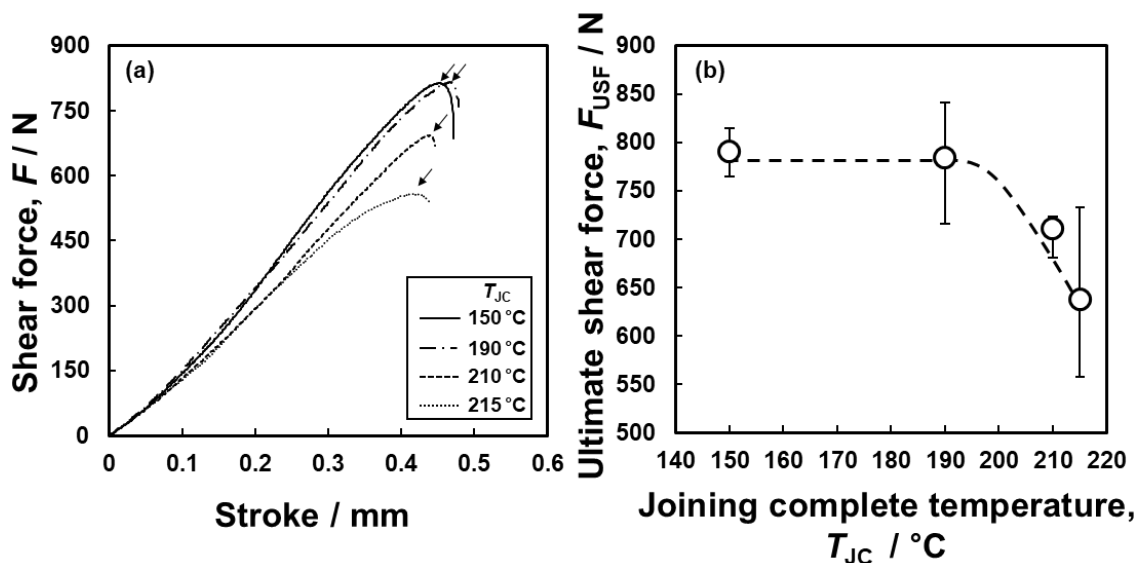


Fig. 4.3 (a) Shear force – stroke curves of Al/PA6 lap joints and (b) ultimate shear force as a function of T_{JC} .

almost constant when T_{JC} was in the range of 150 ~ 190 °C and declined with increasing T_{JC} from 190 to 215 °C.

The SEM micrograph showing the cross-section of the interrupted Al/PA6 lap joint before rupture is indicated in **Fig. 4.4**. Granular protrusions and crack paths were observed. The crack propagated at the interface between PA6 and the top of the granular protrusion. The crack was also observed in PA6 near the interface between the Al and PA6 substrates, which suggests that mechanical behaviors of Al/PA6 lap joint are closely related to the PA6 in the vicinity of the Al surface.

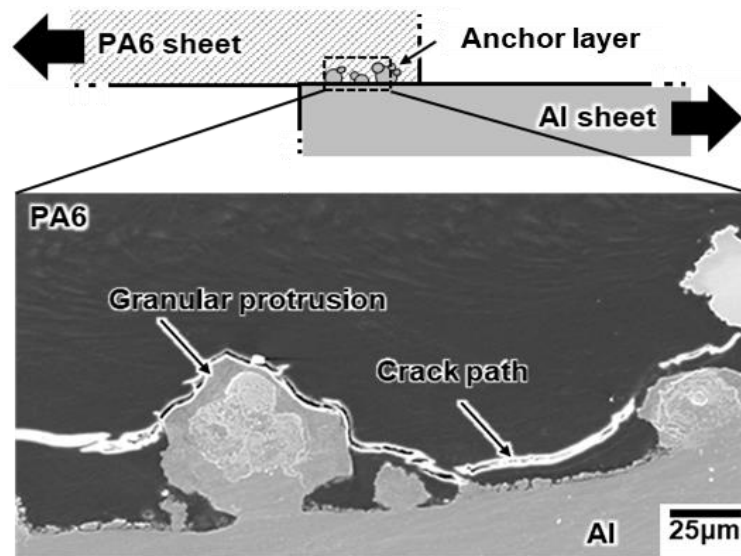


Fig. 4.4 SEM micrograph showing crack paths near the interface between Al and PA6 substrates.

Representative SEM micrographs of fracture surfaces on the Al substrate sides are indicated in **Fig. 4.5**. The PA6 substrates were pulled upward in the images (indicated by the gray arrow). It was observed from the low magnification fracture surfaces that granular protrusions and PA6 interlocked each other and remained on the Al substrate after the lap shear tests under all T_{JC} conditions. The fracture morphologies of PA6 changed with T_{JC} in the high magnification SEM images. In the case of $T_{JC} = 190$ °C, the remained PA6 surface showed the fracture surface resembled the cleavage fracture of metal materials (indicated by the white arrow in the high magnification fracture surface). PA6 hardly exhibited plastic deformation. When T_{JC} was 210 and 215 °C, PA6 severely deformed to the direction of the applied force. The so-called ligaments were observed at T_{JC} of 215 °C (indicated by the black arrow in the high magnification fracture surface). The effect of the degree of crystallinity of a PP specimen on the fracture morphology was

investigated by Dasari et al. [4.4]. It was reported that cleavage like fracture surface of the PP indicated brittle fracture.

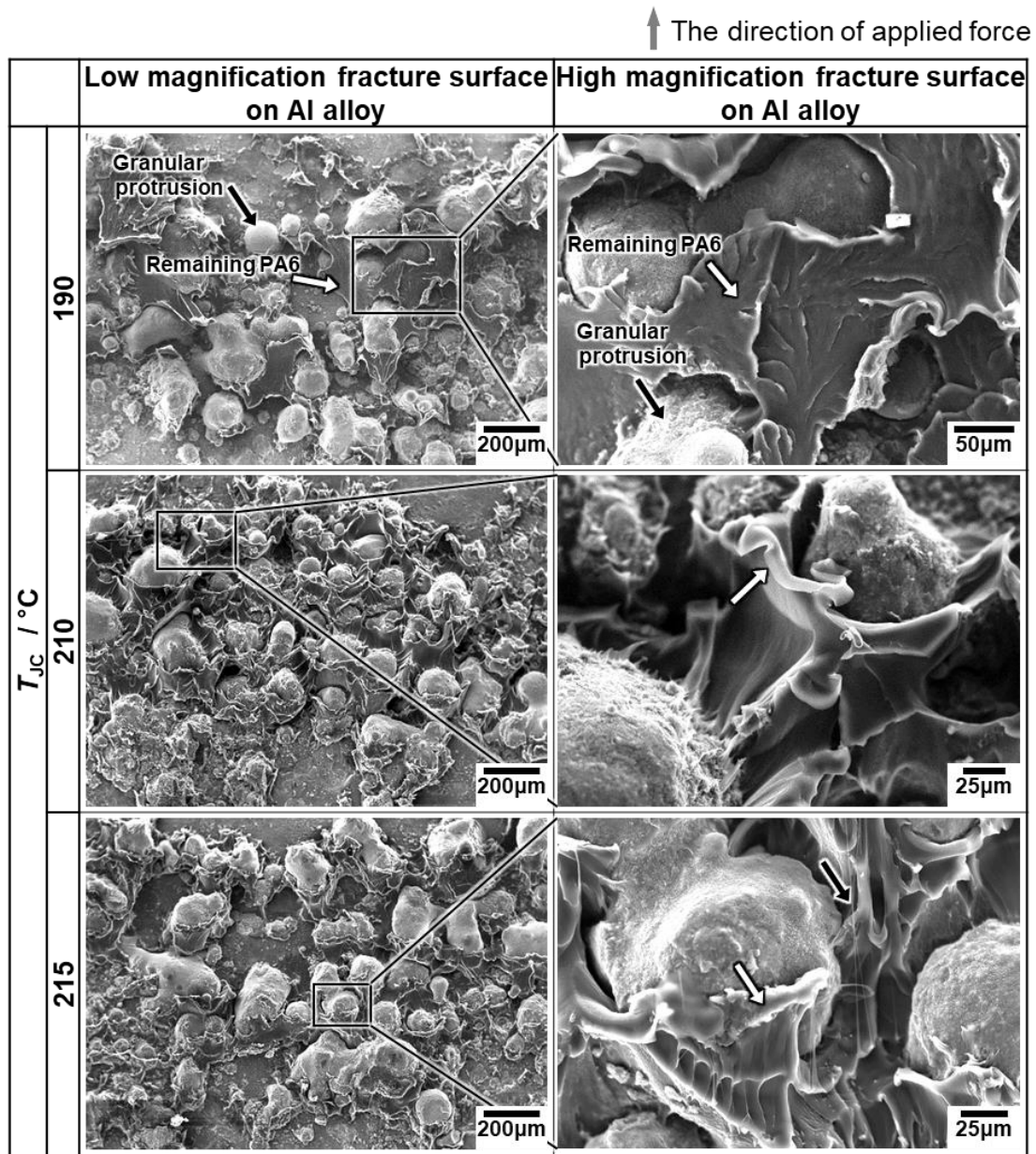


Fig. 4.5 SEM micrographs of the fracture surface of the Al/PA6 lap joints (Al side) formed with different T_{JC} .

4.3.2. Change in the PA6 characteristics

Considering the approximate height of crack paths was around $30 \mu m$ (**Fig. 4.4**), the PA6 film with the thickness of $30 \mu m$ was thin enough to investigate the characteristic changes of PA6 near the metal surface. The XRD profiles of the PA6 films that underwent the same thermal history as the joining process are shown in **Fig. 4.6**. Peaks at $2\theta = 20.4$ and 23.7° were

detected at all T_{JC} conditions. These peaks corresponded to the crystalline phase of PA6 (α -form, α_1 and α_2). The amorphous phase of PA6 (β -form) was detected as a broad peak at all T_{JC} conditions. It was revealed that the γ -form of crystalline PA6 was not detected at all T_{JC} . The PA6 films that underwent the same thermal history with joining process consisted of α -form crystalline phase and β -form amorphous phase.

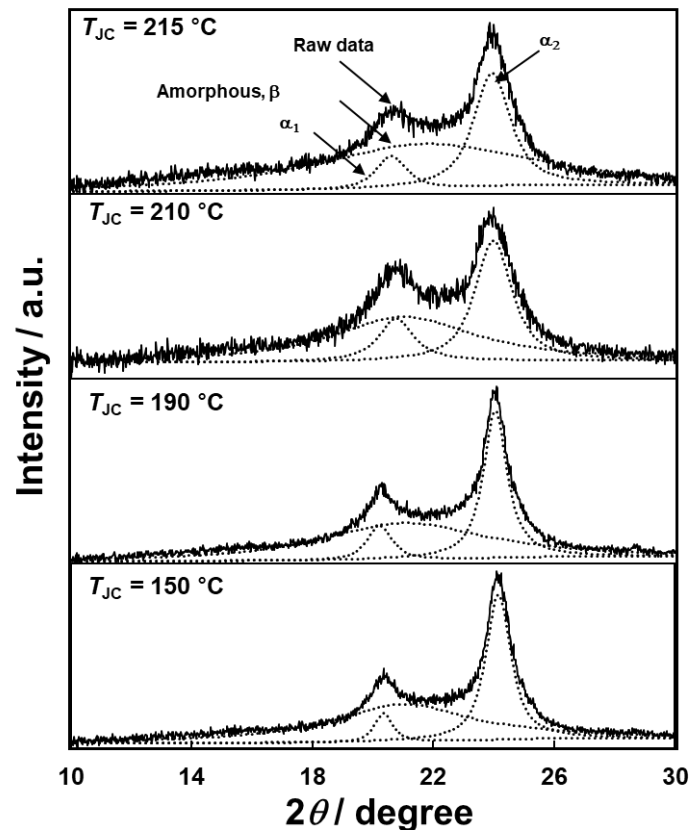


Fig. 4.6 XRD profiles of the PA6 films heated and cooled to different T_{JC} s.

Figure 4.7 (a) shows heating curves of the PA6 films subjected to the same thermal history with the joining process. Endothermic peaks appeared around the melting point of PA6 under all T_{JC} conditions. As the heat of fusion of pure crystalline form (ΔH_f^0), 241 J/g was used because the detected crystalline phase was only α -form (**Fig. 4.6**). **Figure 4.7 (b)** shows the degree of crystallinity as a function of T_{JC} . The degree of crystallinity was almost constant when T_{JC} was in the range of 150 ~ 190 °C and declined with increasing T_{JC} from 190 to 215 °C. It was revealed that the change in the degree of crystallinity was analogous to the change in the joint strength (**Fig. 4.3 (b)**).

Figure 4.8 shows the results of Vickers hardness tests of the PA6 films that underwent the same thermal history as the joining process. The Vickers hardness indicated almost constant value when T_{JC} was in the range of 150 ~ 190 °C and declined with increasing T_{JC} from 190 to

215 °C. The change in the Vickers hardness was analogous to the change in the joint strength (Fig. 4.3 (b)) and the degree of crystallinity (Fig. 4.7 (b)).

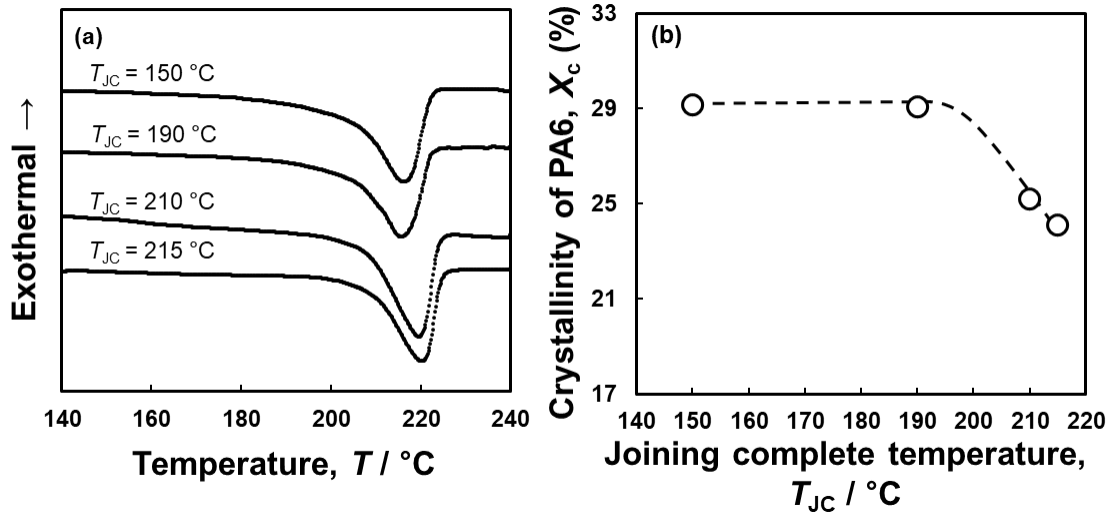


Fig. 4.7 (a) DSC heating curves of the PA6 films heated and cooled to different T_{JC} and (b) change in the degree of crystallinity as a function of T_{JC} .

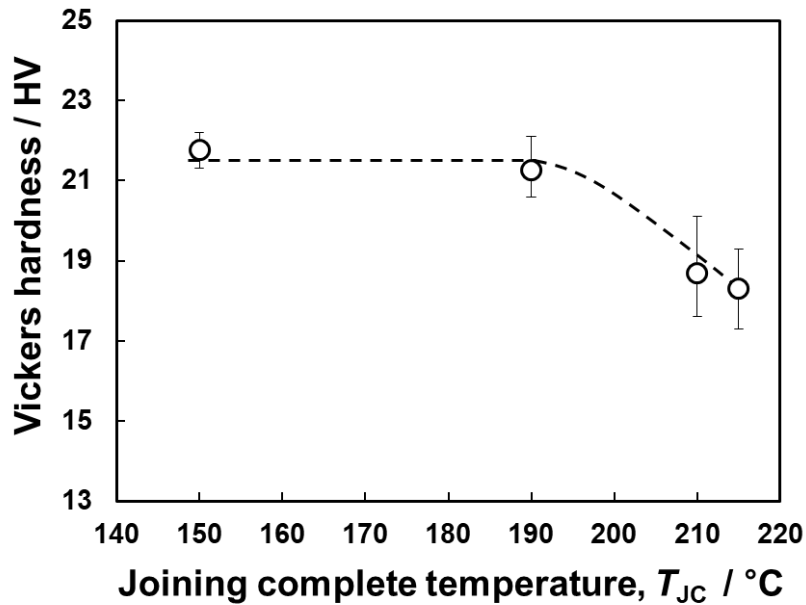


Fig. 4.8 Vickers hardness of the PA6 films heated and cooled to different T_{JC} .

4.4. Discussion

The influence of thermal joining history on the Al/PA6 lap joint strength was investigated. It was revealed that the joint strength, the degree of crystallinity, and the hardness of PA6 was almost constant when T_{JC} was in the range of 150 ~ 190 °C and declined with increasing T_{JC} from 190 to 215 °C (Fig. 4.3 (b), 4.7 (b), and 4.8). Fracture surface indicated that

the PA6 remained on the Al substrate hardly deformed plastically at lower T_{IC} than 190 °C (**Fig. 4.5**). According to Dasari et al. [4.4], the fraction of brittle fracture surface rose, and ligaments decreased with increasing the degree of crystallinity. These findings suggest that the degree of crystallinity of PA6 near the Al/PA6 interface couldn't increase any more when the PA6 was furnace-cooled below 190 °C. The PA6 was strengthened due to the increased degree of crystallinity, resulting in increasing the joint strength. The yielding strengths in the shear force - stroke curves (**Fig. 4.3**) were consistent with the joint strengths. Humbert et al. [4.5] found that the degree of crystallinity and yield stress indicated a linear correlation in the case of polyethylene (PE) semi-crystalline polymer. The increase in the yield strength of PA6 with its degree of crystallinity caused the increase in the joint strength.

The cooling curves of the as-received PA6 films are shown in **Fig. 4.9**. Exothermic peaks appeared under all T_{IC} conditions. The crystallization beginning and ending temperature were different depending on the cooling rate. The crystallization beginning/ending temperatures, and enthalpy of crystallization were obtained from the cooling curves and summarized in **Table 4.1**. It was found that the crystallization beginning/ending temperature and enthalpy of crystallization increased with a decrease in the cooling rate. When the cooling rate was low, the crystallization started and ended at higher temperature compared with higher cooling rate condition. The crystallization was suppressed under the fast cooling rate conditions. These findings were consistent with previous reports. Di Lorenzo et al. [4.6] found that the crystallization beginning temperature of PP decreased in the faster cooling conditions. The degree of crystallinity of PA6 increased under the slow cooling condition according to Pesetskii et al. [4.7].

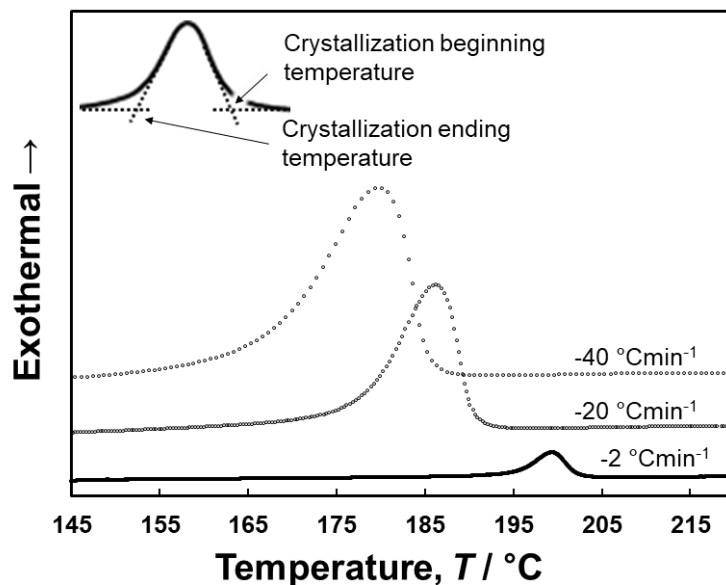


Fig. 4.9 DSC curves measured under the cooling scans of the as-received PA6 films with different cooling rate

Table 4.1 Crystallization beginning/ending temperatures and enthalpy of crystallization obtained using as-received PA6 films with different cooling rate.

	Cooling rate (°C/min)		
	2	20	40
Crystallization beginning temperature (°C)	203	191	186
Crystallization ending temperature (°C)	195	177	167
Enthalpy of crystallization (J/g)	77	60	56

Figure 4.10 shows changes in (a) the crystallization beginning/ending temperatures and (b) the enthalpy of crystallization obtained using as-received PA6 films with different cooling rate. The cooling rate significantly influenced the crystallization behavior of PA6. The same thermal profiles which were used for fabricating Al/PA6 lap joint are indicated in black ($T_{IC} = 150\text{ °C}$) and gray ($T_{IC} = 215\text{ °C}$) arrows. When the Al and PA6 substrates were joined at 215 °C and furnace-cooled to 150 °C ($T_{IC} = 150\text{ °C}$), PA6 near the interface of the PA6 and Al substrate were crystallized sufficiently since it was experienced slow cooling (2 °C/min) below the crystallization ending temperature (black arrows in **Fig. 4.10**). On the other hand, when the Al and PA6 substrates were joined at 215 °C and taken out from the hot sample stage, PA6 could not be crystallized sufficiently because the cooling rate was fast (90 °C/min) (indicated by the gray arrows in **Fig. 4.10**). The change in the cooling rate was responsible for the crystallization behavior of PA6, resulting in the change in the joint strength.

The findings revealed in the present study have a potential to improve the joint strength of metal/semi-crystalline polymer structures. Most of thermal joining processes utilize high temperature above the melting point of polymer for interlocking the molten polymer with dimples or protrusions formed on the metal surface. The joint strength can be improved without providing extra energy by adopting the slow cooling in the joining machine after the joining process. Another possible way is annealing the metal/polymer hybrid structures around the polymer crystallization temperature. It was reported that the joint strength improved by annealing the metal/polymer lap joint [4.8].

Recently, carbon fiber reinforced thermoplastics (CFRTPs) have been introduced for structural components because of its high specific strength and formability. The CFRTPs can be joined with metal substrates by not only adhesive and mechanical fasteners but also thermal process because thermoplastics are used as matrix materials [4.9]. PA6 is one of the matrix materials for the CFRTPs [4.10]. It is considered that the results revealed in this study are applicable for joining CFRTPs consisting of PA6 matrix with metals even though future research is required.

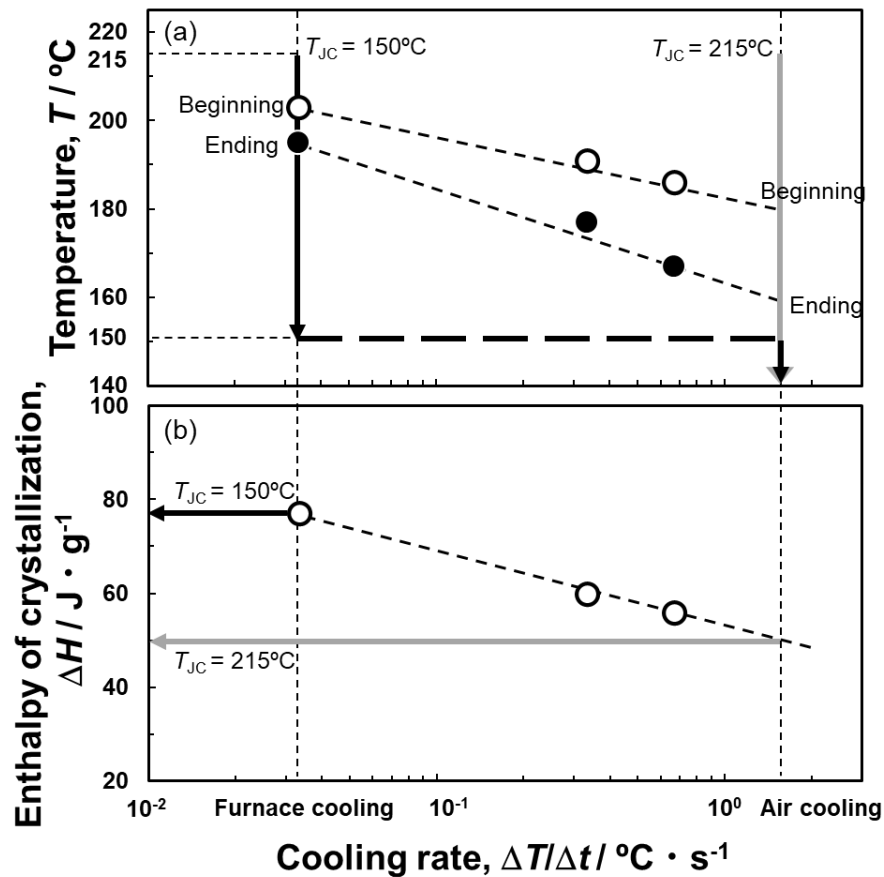


Fig. 4.10 Changes in (a) the crystallization beginning and ending temperatures and (b) enthalpy of crystallization of as-received PA6 film as a function of the cooling rate.

4.5. Summary

- The Al/PA6 lap joint strength, the degree of crystallinity and Vickers hardness of PA6 were constant at T_{JC} below 190 °C and declined as the T_{JC} increased from 190 °C to 215 °C.
- The strength of PA6 near the joint interface increased due to the increase in the degree of crystallinity. As a result, the joint strength increased.
- In the case of the Al/PA6 lap joint fabricated at T_{JC} below 190 °C, the degree of crystallinity of PA6 increased sufficiently because of slow cooling under the crystallization ending temperature.
- The fracture morphology of PA6 remaining on the Al substrate after lap shear test indicated brittle fracture surface at T_{JC} below 190 °C due to its high crystallinity.

References

- [4.1] Fornes, T. D., Paul, D. R. Crystallization behavior of nylon 6 nanocomposites. *Polymer*. 2003, 44(14), 3945-3961.
- [4.2] Miri, V., Persyn, O., Lefebvre, J. M., Seguela, R. Effect of water absorption on the plastic deformation behavior of nylon 6. *European Polymer Journal*. 2009, 45(3), 757-762.
- [4.3] Yang, C., Tian, X., Li, D., Cao, Y., Zhao, F., Shi, C. Influence of thermal processing conditions in 3D printing on the crystallinity and mechanical properties of PEEK material. *Journal of Materials Processing Technology*. 2017, 248, 1-7.
- [4.4] Dasari, A., Rohrmann, J., Misra, R. D. K. Surface microstructural modification and fracture behavior of tensile deformed polypropylene with different percentage crystallinity. *Materials Science and Engineering: A*. 2003, 360(1-2), 237-248.
- [4.5] Humbert, S., Lame, O., Vigier, G. Polyethylene yielding behaviour: What is behind the correlation between yield stress and crystallinity?. *Polymer*. 2009, 50(15), 3755-3761.
- [4.6] Di Lorenzo, M. L., Silvestre, C. Non-isothermal crystallization of polymers. *Progress in Polymer Science*. 1999, 24(6), 917-950.
- [4.7] Pesetskii, S. S., Jurkowski, B., Olkhov, Y. A., Bogdanovich, S. P., Koval, V. N. Influence of a cooling rate on a structure of PA6. *European polymer journal*. 2005, 41(6), 1380-1390.
- [4.8] Xie, Y., Zhang, J., Zhou, T. Large-area mechanical interlocking via nanopores: Ultra-high-strength direct bonding of polymer and metal materials. *Applied Surface Science*. 2019, 492, 558-570.
- [4.9] Nagatsuka, K., Yoshida, S., Tsuchiya, A., Nakata, K. Direct joining of carbon-fiber-reinforced plastic to an aluminum alloy using friction lap joining. *Composites Part B: Engineering*. 2015, 73, 82-88.
- [4.10] Ishikawa, T., Amaoka, K., Masubuchi, Y., Yamamoto, T., Yamanaka, A., Arai, M., Takahashi, J. Overview of automotive structural composites technology developments in Japan. *Composites Science and Technology*. 2018, 155, 221-246.

5. Effect of the molar ratio of C powder in Al-Ti-C powder blend on the structure and microstructure of the anchor layer for joining an Al alloy and Polyamide-6

5.1. Introduction

The anchor layer was fabricated using the Al-Ti (molar ratio of 1:1) and Al-Ti-C (molar ratio of 1:1:1) starting powders in Chapter 3. The anchor layer consisted of a dense layer when the Al-Ti starting powder was used. On the other hand, the anchor layer consisted of many granular protrusions when it was fabricated with the Al-Ti-C starting powder. The TiC phase was generated by the addition of C powder and dramatically changed the morphology of the anchor layer by forming the TiC skeleton structure in granular protrusions. The above results give a potential that the structure of the anchor layer can be controlled by adjusting the C molar ratio. In this chapter, the effect of C molar ratio in the Al-Ti-C starting powder on the microstructure and morphology of the anchor layer was investigated. The morphology of the anchor layer was evaluated quantitatively and discussed based on the microstructure and thermodynamic calculations. Each anchor layer fabricated by the Al-Ti-C starting powders with different C molar ratio was used for joining an Al alloy (A5052) and PA6 substrates. The relationship between the joint strength and morphology was investigated.

5.2. Experimental methods

The process of fabricating anchor layer was same as the process that explained in section 3.2. The molar ratio of Al:Ti:C was set at 1:1: M_C ($M_C = 0, 0.4, 0.6, 0.8, 1.0, \text{ and } 1.5$). After the powder mixing, each starting powder was observed using the SEM. The EDS analysis was conducted to confirm the distribution of Al, Ti and C powders. The top-view of the anchor layer was observed using the SEM. The XRD analysis was conducted for each anchor layer with the same condition as explained in section 3.2.

The cross-section of the anchor layer was observed using the SEM (back scattered electron mode). The method to expose the cross-section of the anchor layer was same as explained in section 3.2. The EDS analysis was conducted on the cross-sectioned anchor layer to obtain element maps of Al, Ti, and C.

The structure of the anchor layer was quantitatively evaluated using the SEM images of top-view and cross-sectioned view of the anchor layer with ImageJ software. **Figure 5.1 (a)** shows the representative entire SEM micrograph showing the anchor layer. The area of each anchor layer was calculated with the entire SEM image of the anchor layer. **Figure 5.1 (b)** shows the representative top-view anchor layer and its binarized image. Projected area fraction of granular protrusions was calculated by dividing white area by total area (black area + white area). Two

images for each anchor layer were used to calculate the area and projected area fraction. Bonding ratio of granular protrusions, which indicates the adhesiveness between the granular protrusions and substrate, was calculated using SEM images of the cross-sectioned anchor layers as indicated in **Fig. 5.1 (c)** by following equation.

$$\text{Bonding ratio} = \frac{\sum_n l_n}{\sum_m W_m} \quad (5.1)$$

where W_m and l_n correspond to the maximum width of each granular protrusion and length of each bonded part of protrusions with the Al substrate, respectively. More than 25 granular protrusions for each anchor layer were used to calculate the bonding ratio.

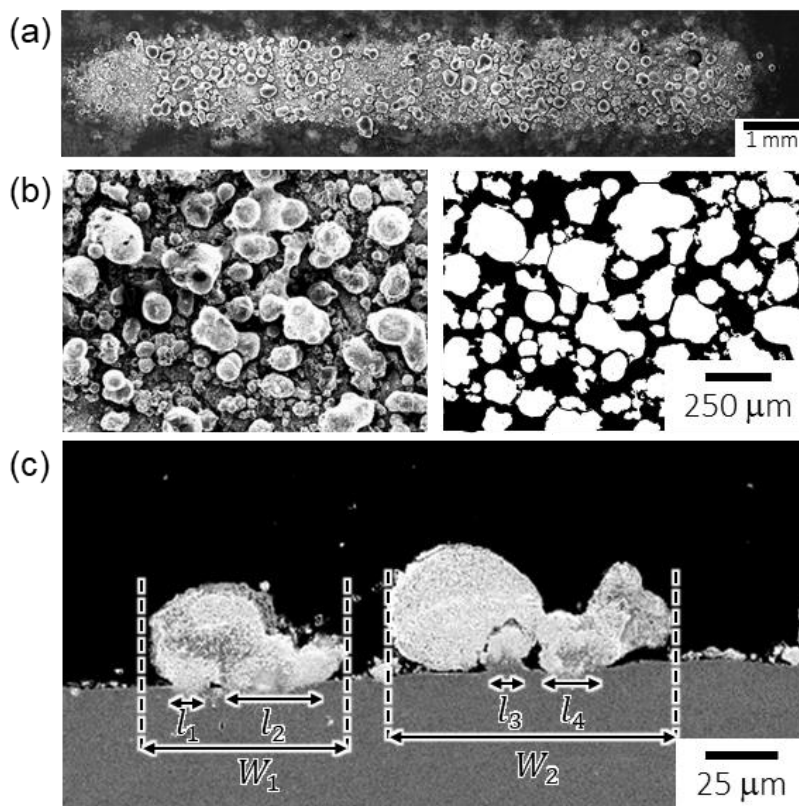


Fig. 5.1 Representative images for quantitative evaluation of the anchor layers: (a) entire SEM micrograph of the anchor layer, (b) top-view anchor layer and binarized image, (c) cross-sectioned anchor layer.

Hot-pressing was used to join the Al and PA6 substrates. The joining process was same as explained in section 4.2.1. In this section, joining complete temperature (T_{JC}) was fixed at 190 °C. Schematic illustration with dimensions of the Al/PA6 lap joint is shown in **Fig. 5.2**. The area where the PA6 and Al substrate overlap became shorter from 10 mm to 4 mm to minimize the influence from the Al substrate part where the anchor layer was not formed on the joint strength. The lap shear testing was carried out as the same method and conditions explained in section 3.2.

Four Al/PA6 lap joint samples were tested to evaluate average ultimate shear force (F_{USF}) for each anchor layer. After the lap shear tests, fracture surfaces on the Al substrate side were observed using the SEM.

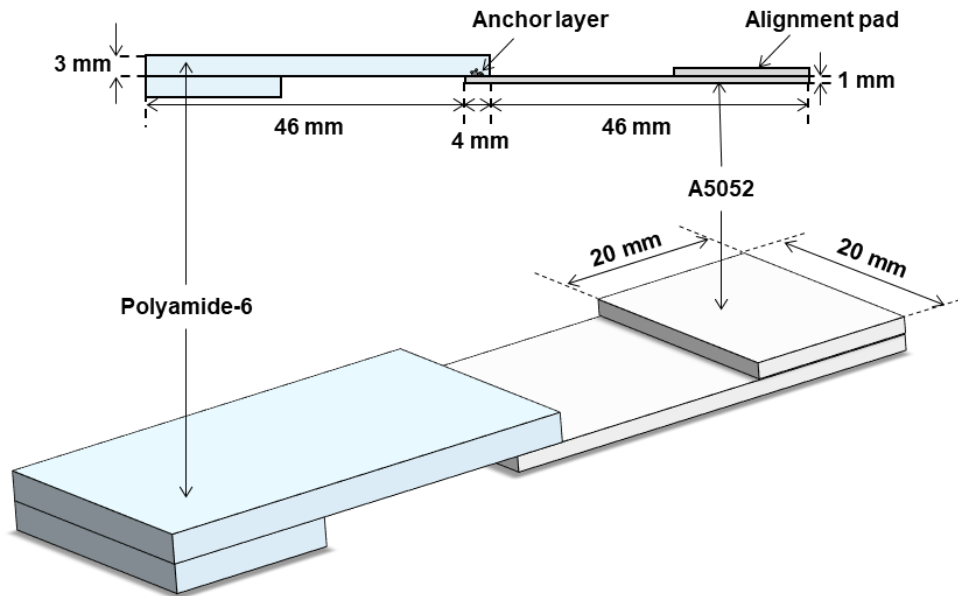


Fig. 5.2 Schematically illustrated Al/PA6 lap joint for shear test.

Thermodynamic equilibrium calculations were carried out for the Al-Ti-C ternary system using a conventional database of PanAluminum [5.1]. The Scheil solidification simulation was carried out to examine the solidification path and component partitioning during the solidification after laser irradiation on Al-Ti-C starting powders. Assumptions of the Scheil simulation are equilibrium at the liquid-solid interface, complete mixing of elements in the liquid phase, and no diffusion in the solid phase [5.2]. The Scheil solidification model can estimate the trend of solidified phases in the case of rapid cooling [5.3]. A detailed explanation about the Scheil simulation is given in the Appendix B.

5.3. Results

5.3.1. Characterization of the anchor layers

Figure 5.3 indicates the SEM micrographs and EDS maps (Al, Ti, and C elements) of starting powders with the C molar ratio (M_C) of 0.4, 0.6, and 1.5. The Al and Ti powders were homogeneously blended in each starting powder. Although the C powder aggregated, the aggregated powder was well distributed in each starting powder.

The representative SEM micrographs showing the top-view of the anchor layers produced with each M_C are shown in **Fig. 5.4**. The morphology of the anchor layer changed significantly depending on M_C . When C powder was not included in the starting powder ($M_C = 0$), the dense layer was produced along with the laser irradiation direction. It was observed that

granular protrusions were produced after the C powder was added ($M_C = 0.4$). However, the granular protrusions were not distributed homogeneously and not formed around the centerline of the laser irradiated region. In the case of $M_C \geq 0.6$, the granular protrusions were distributed homogeneously on the laser irradiated region.

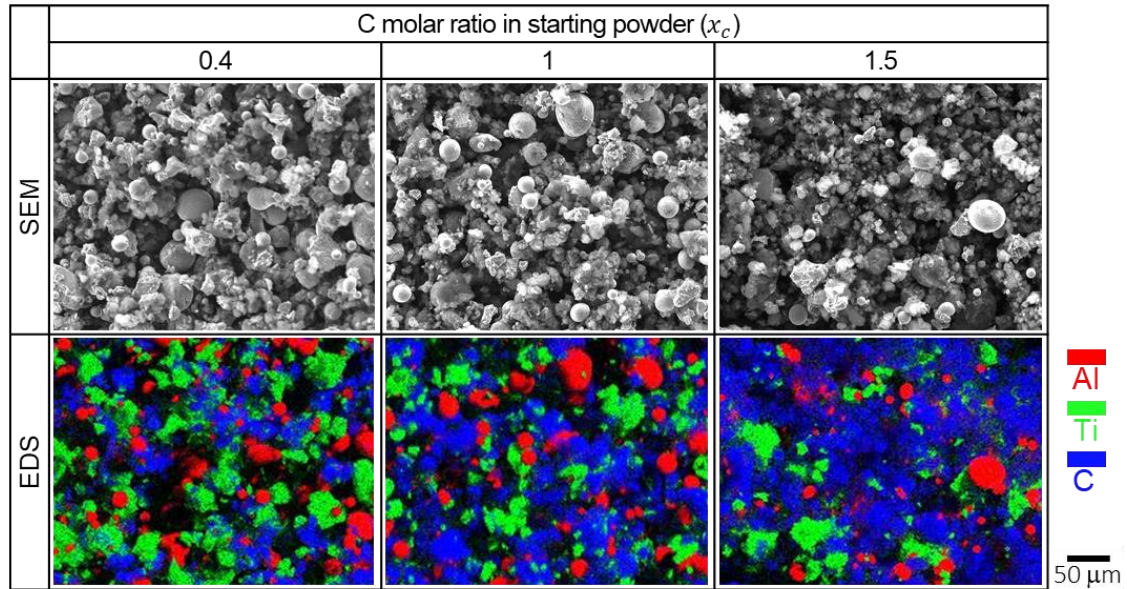


Fig. 5.3 SEM micrographs of starting powders and EDS element maps of Al, Ti, and C elements.

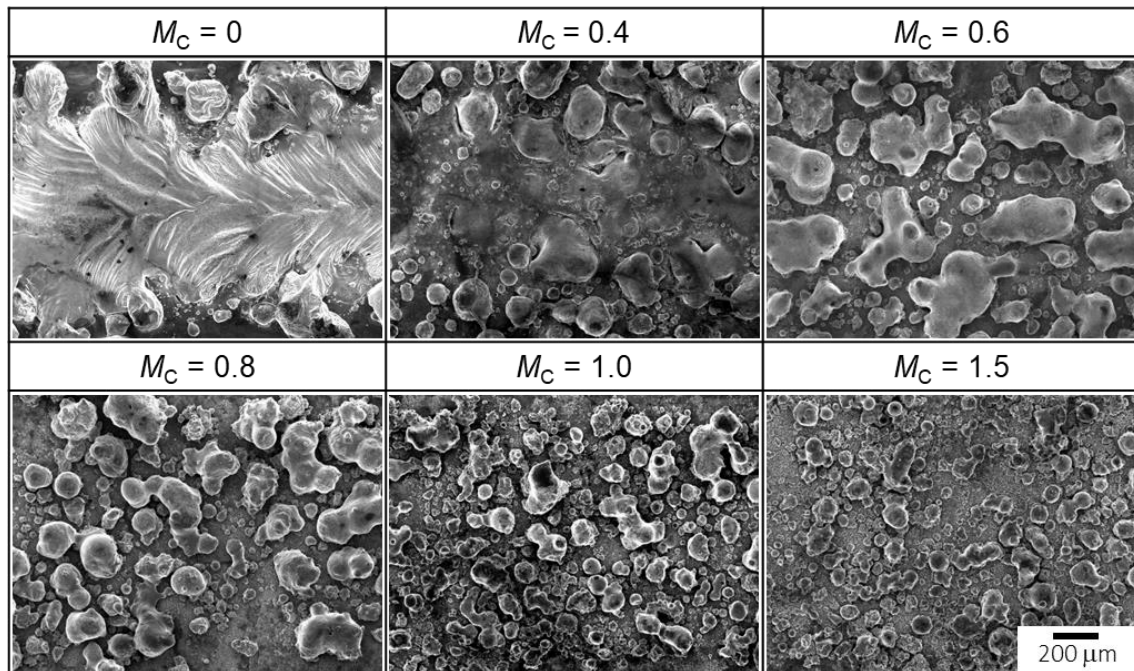


Fig. 5.4 Representative SEM micrographs showing the top-view of the anchor layer produced with each C molar ratio (M_C).

The quantitatively evaluated projected area fraction of the top-view anchor layers as a function of C molar ratio is shown in **Fig. 5.5**. Error bars indicate maximum and minimum values. The projected area fraction increased in the range of $M_C = 0.4 \sim 0.8$ and declined in the range of $M_C = 0.8 \sim 1.5$.

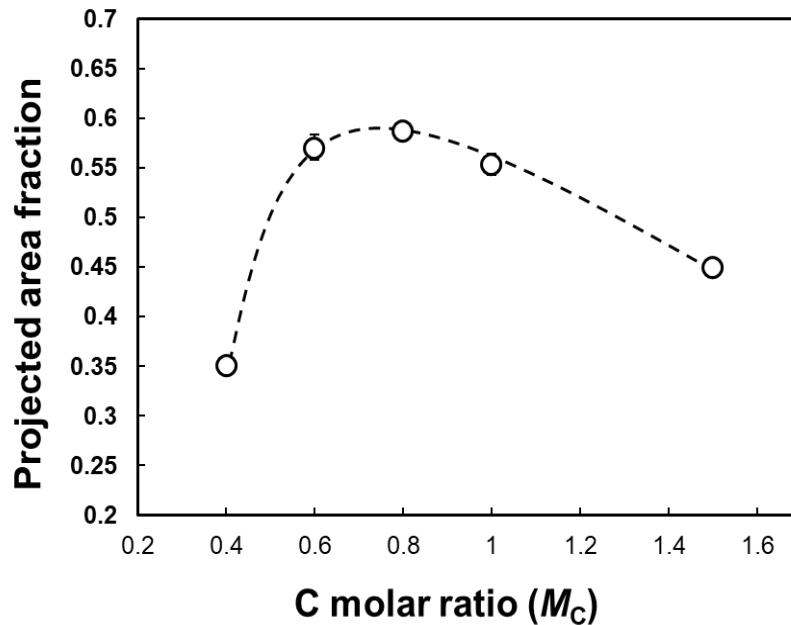


Fig. 5.5 Change in projected area fractions of the anchor layers as a function of C molar ratio (M_C).

The representative SEM micrographs showing the cross-sectioned anchor layers were shown in **Fig. 5.6**. The surfaces of the Al substrates were indicated with dotted lines in the images, which were extrapolated from the surface of the non-laser-irradiated region. In the case of M_C of 0.4, the dense layer was deposited on the Al substrate instead of the granular protrusions. The dense layer consisted of various phases with different contrast. The granular protrusions were produced on the surface of the Al substrate when M_C were 0.6 and 1.0. The granular protrusions were filled with the phase with the brightest contrast. In the case of $M_C = 0.4$ and 0.6, the phase with the brightest contrast was formed below the Al substrate surface line, while it was mainly formed in the granular protrusions in the case of M_C of 1.0.

Figure 5.7 indicates quantitatively evaluated bonding ratio of the granular protrusions as a function of M_C . The bonding ratio indicated a high value of over 0.8 when M_C was in the range of 0.4 ~ 0.6 and sharply decreased when M_C changed from 0.6 to 0.8. The bonding ratio was almost constant at approximately 0.35 when M_C was in the range of 0.8 ~ 1.5.

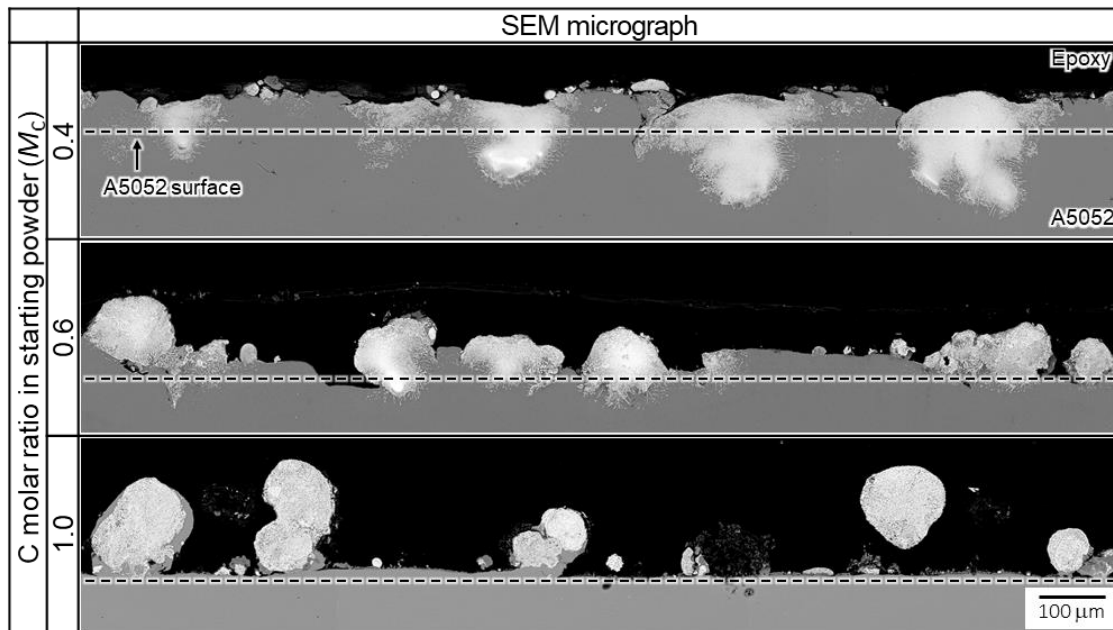


Fig. 5.6 Representative SEM micrographs of the cross-sectioned anchor layer formed with different C molar ratio ($M_C = 0.4, 0.6,$ and 1.0).

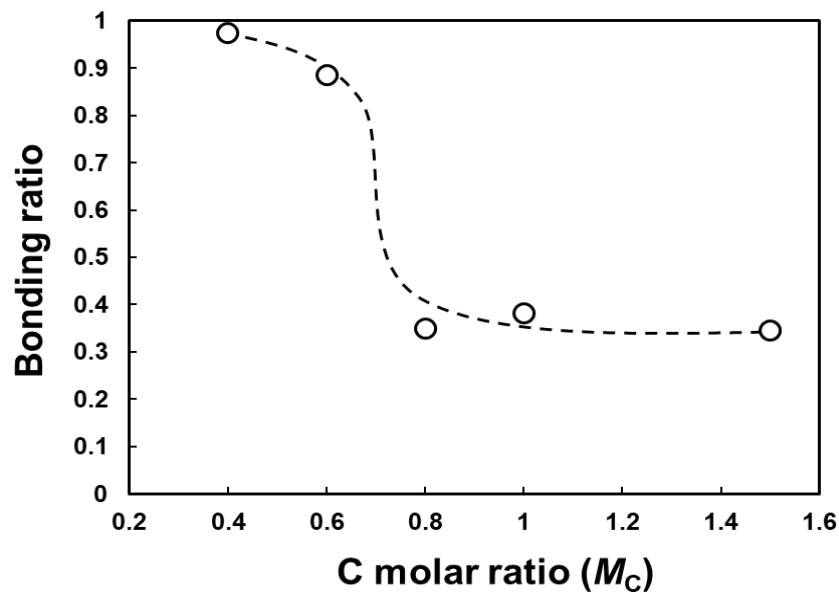


Fig. 5.7 Bonding ratio of the anchor layer as a function of C molar ratio (M_C).

The XRD profiles of the anchor layers fabricated with each starting powder are shown in **Fig. 5.8**. Peaks for TiC, Al₄C₃, Al₃Ti, and α -Al were detected from all the anchor layers. The peaks for the Al₄C₃ and Al₃Ti changed depending on M_C . Peak intensity changes at 31.9° (one of diffraction peaks for Al₄C₃) and 39.2° (one of diffraction peaks for Al₃Ti) as function of C molar ratio are indicated in **Fig. 5.8 (b)** and **(c)**. The peak intensity at 31.9° increased with an increase in M_C , while the peak intensity at 39.2° reduced with an increase in M_C . These results suggested that the Al₃Ti and Al₄C₃ phases were formed preferably in lower and higher M_C , respectively.

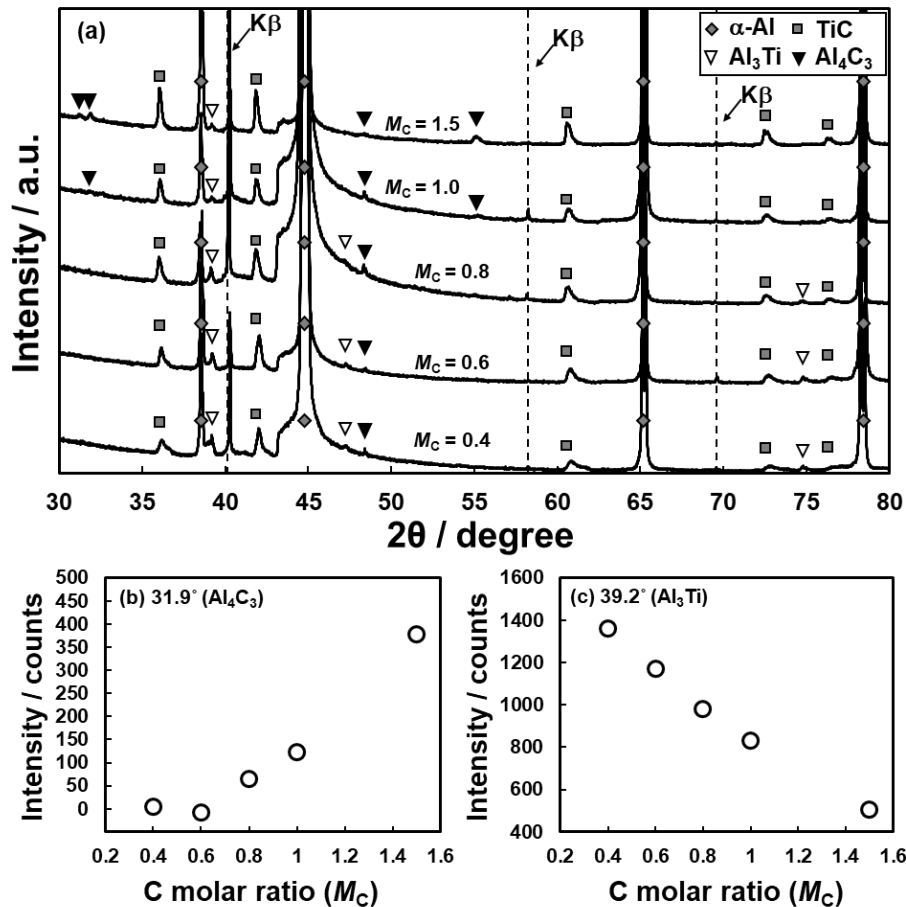


Fig. 5.8 (a) XRD profiles of the anchor layers formed with different C molar ratio (M_C). Changes in peak intensities at (b) Al_4C_3 ($2\theta = 31.9^\circ$) and (c) Al_3Ti ($2\theta = 39.2^\circ$) as a function of C molar ratio (M_C).

Figure 5.9 shows representative SEM images and elements maps (Al and Ti) of the cross-sectioned anchor layer produced with different starting powders ($M_C = 0.6$ and 1.0). The EDS element maps indicated that the Ti element was enriched in the phases with brighter contrasts in the granular protrusions. The Ti-enriched phases were detected below the surface of the Al substrate in the case of $M_C = 0.6$.

The SEM micrographs and elements maps (Al, Ti, and C) in the middle region (surrounded by dotted line in **Fig. 5.9**) of the cross-sectioned anchor layer are shown in **Fig. 5.10**. Two phases were observed when M_C was 0.6 (**Fig. 5.10 (a)**). The phase with brighter contrast containing the Ti and C elements was TiC judged from the XRD result. The TiC phase indicated granular and dendritic morphologies. The darker phase containing the Al and Ti elements was Al_3Ti judged from the XRD results. In the case of $M_C = 1.0$ (**Fig. 5.10 (b)**), three phases were observed. The darkest phase containing only the Al element was α -Al. The other phases were Al_3Ti (middle contrast) and TiC (brightest phase) judged from the XRD and EDS results. The amount of Al_3Ti phase was higher in the case of $M_C = 0.6$ than in the case of $M_C = 1.0$. The SEM

micrographs and elements maps (Al, Ti, and C) in the region near substrate (surrounded by solid line in Fig. 5.9) of the cross-sectioned anchor layer are shown in Fig. 5.11. The Al, TiC, and Al₃Ti phases were observed in both $M_C = 0.6$ (Fig. 5.11 (a)) and 1.0 (Fig. 5.11 (b)). The Al₃Ti phase was elongated to downward direction in the figures (toward the substrate).

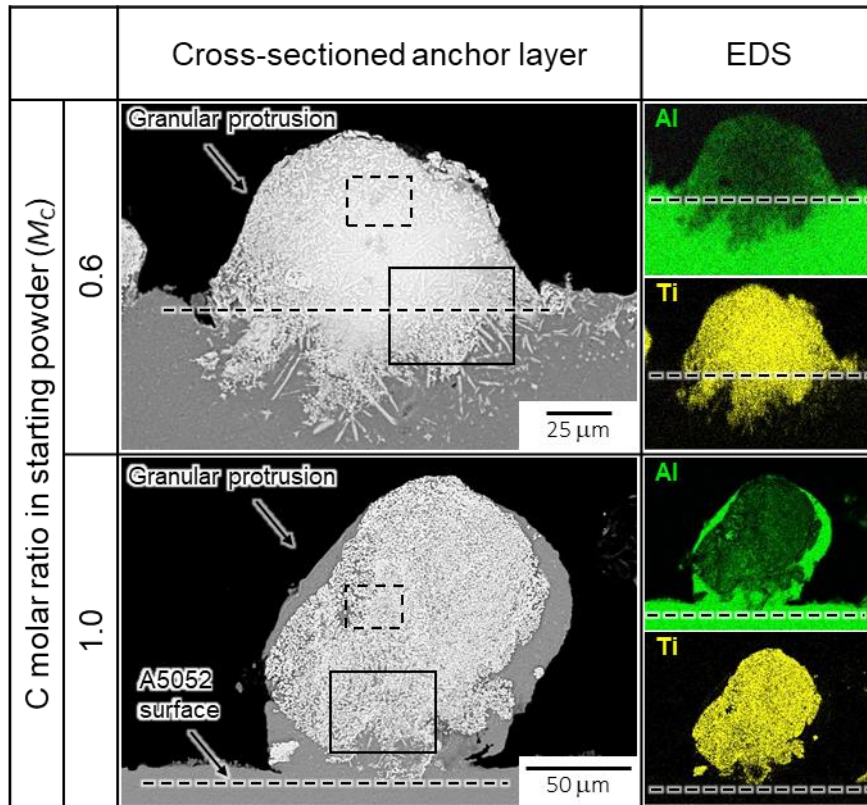


Fig. 5.9 SEM micrographs and Al, Ti element results of cross-sectioned anchor layer formed with different starting powders ($M_C = 0.6$ and 1.0).

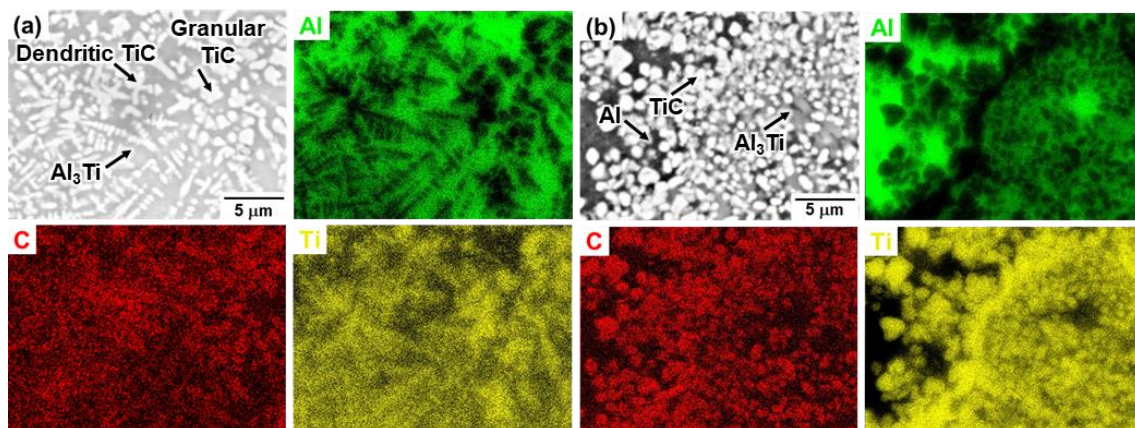


Fig. 5.10 High magnification SEM micrographs and element maps (Al, Ti, and C) in the middle region of the granular protrusions formed with different starting powders ((a) $M_C = 0.6$ and (b) $M_C = 1.0$).

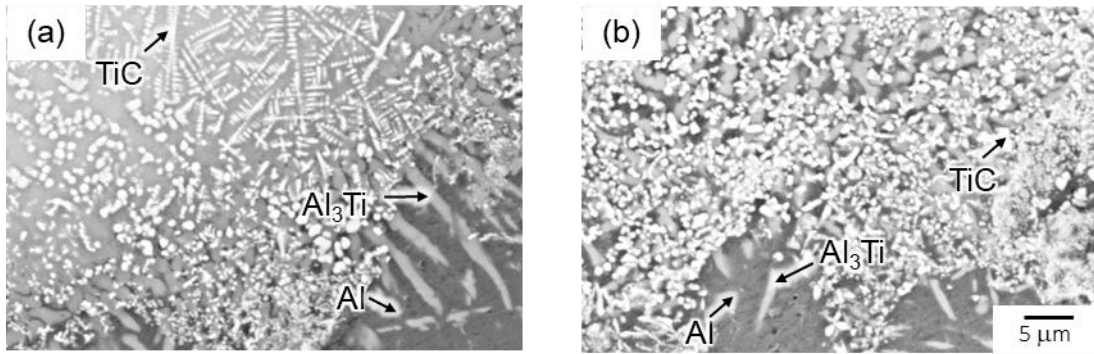


Fig. 5.11 High magnification SEM micrographs in the near substrate region of the granular protrusions formed with different starting powders ((a) $M_C = 0.6$ and (b) $M_C = 1.0$).

5.3.2. Mechanical properties of Al/PA6 lap joints

The changes in the ultimate shear force (F_{USF}) and area of the anchor layer as a function of M_C are shown in **Fig. 5.12**. The F_{USF} indicated the highest and lowest values at $M_C = 0.6$ and 1.5, respectively. The area of the anchor layer indicated almost constant value at $M_C = 0.4$ and 0.6. It slightly decreased when M_C changed from 0.6 to 0.8 and maintained constant value at $M_C = 0.8 \sim 1.5$.

The SEM micrographs of the top-view of the anchor layers and corresponding fracture surfaces for each starting powder after lap shear tests are shown in **Fig. 5.13**. It was observed from the fracture surfaces that the PA6 (indicated by the black arrows) and granular protrusions (indicated by the white arrows) remained on the Al substrate, indicating PA6 and granular protrusions interlocked each other. In the case of $M_C = 0.4$ and 0.6, many granular protrusions remained on the Al substrate. In the case of $M_C = 0.4$, PA6 did not remain around the centerline of the laser-irradiated region where the granular protrusions were hardly formed. In the case of

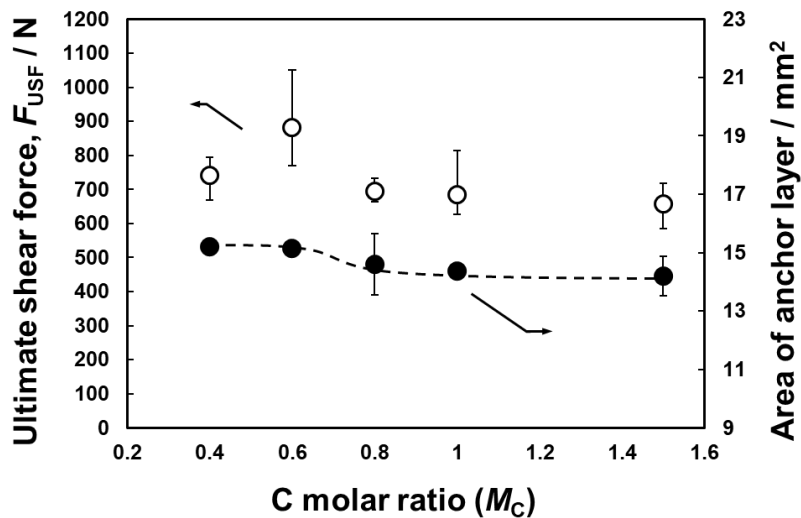


Fig. 5.12 Changes in ultimate shear force (F_{USF}) of Al/PA6 lap joint and entire area of the anchor layers as a function of C molar ratio (M_C).

$M_C \geq 0.8$, many granular protrusions fractured in comparison with the micrographs before the lap shear test.

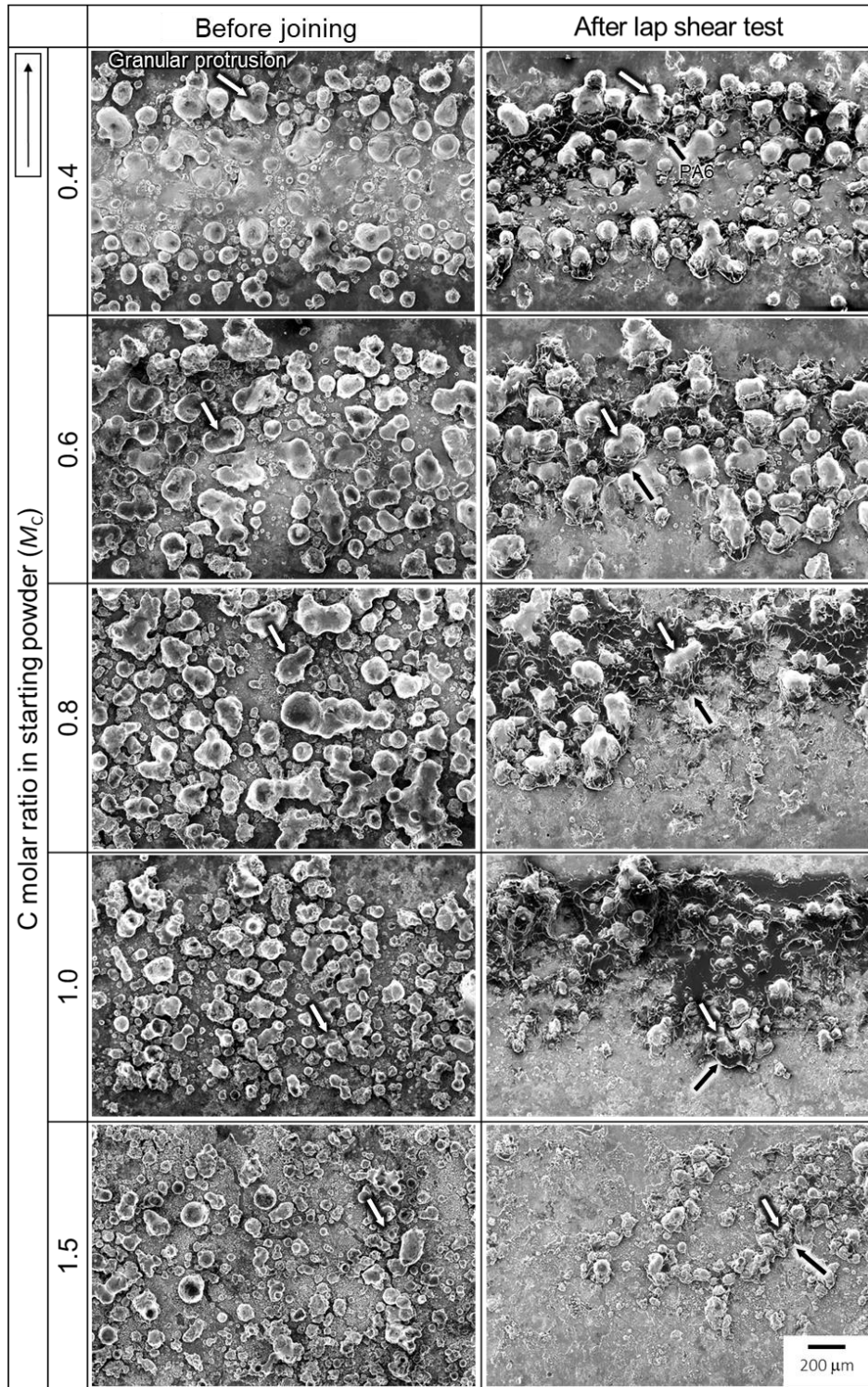


Fig. 5.13. SEM images showing the anchor layer before joining and corresponding fracture surface after shear tests (direction of applied force is indicated in white box).

5.4. Discussion

5.4.1. Morphology and microstructure of the anchor layer

The influence of M_C in the starting powders on the morphology and microstructure of the anchor layer was examined. When M_C was 0.8, the projected area was the highest value (**Fig. 5.5**). The TiC phase was formed in the anchor layer over all M_C conditions (**Fig. 5.8** and **5.10**). As indicated in **Fig. 3.8**, the TiC phase helped to form the granular protrusion. It is thought that the amount of TiC phase influenced the change of the projected area fraction of the anchor layers. The bonding ratio decreased rapidly when M_C changed from 0.6. to 0.8 (**Fig. 5.7**). The Al_3Ti phase elongated below the substrate was observed at the interface between the Al substrate and anchor layer which indicated high bonding ratio (**Fig. 5.7** and **5.11**). The bonding ratio and the formation of Al_3Ti phase increased with a decrease in M_C (**Fig. 5.7** and **5.8**). According to Yang et al. [5.3], the wettability between a metal surface and molten metal was improved by interfacial chemical reaction. From the above results, it is considered that the increase of the bonding ratio was attributed to the Al_3Ti formation reaction, which occurred at the interface between the Al substrate and anchor layer. Therefore, the formation of the TiC and Al_3Ti phases are meaningful.

Thermodynamic analysis was carried out to understand the TiC and Al_3Ti phases formation process. **Figure. 5.14 (a)** shows that calculated liquidus projection for the Al-Ti-C system and its calculated vertical section of equilibrium phase diagram in the case of the Al/Ti molar ratio = 1.0 (dotted-line in **Fig. 5.14 (a)**) is shown in **Fig. 5.14 (b)**. It was found from the liquidus projection that the TiC phase is the primary solidifying phase in the case of all powder compositions (indicated on the dotted-line in **Fig. 5.14 (a)**). The TiC phase indicated both dendritic and granular morphologies (**Fig. 5.10**). According to Emamian et al. [5.5], the dendritic and granular morphologies of TiC was formed in a partially solid melt pool. These facts suggest that the dendritic and granular morphologies of TiC phases were derived from the TiC + liquid phases region indicated in **Fig. 5.14 (b)** and the temperature reached the TiC + liquid phases region at least. As indicated in **Fig. 5.14 (b)**, secondary solidifying phases (Al_3Ti or Al_4C_3) would change depending on the C content in the studied Al-Ti-C starting powders (indicated in the dotted-lines in **Fig. 5.14 (b)**). The Al_3Ti and Al_4C_3 phases would be fabricated in the partially melted and quickly solidified powder generated by laser scanning. **Figure. 5.15** shows (a, b) solidification sequence and (c, d) component partitioning in liquid phase during solidification calculated based on Scheil assumption: (a, c) $M_C = 0.6$ and (b, d) $M_C = 1.0$. In the case of $M_C = 0.6$, after the primary TiC phase is generated in the liquid phase, the Al_3Ti phase is formed as indicated in the solidification sequence (**Fig. 5.15 (a)**). During the solidification process, the Ti and C contents in liquid phase form the TiC phase and decrease monotonically as shown in component partitioning (**Fig. 5.15 (c)**). After the TiC formation, the Ti element remains in the liquid phase and then forms Al_3Ti phase at low temperature. In the case of $M_C = 1.0$, the formation

of the TiC phase is followed by the formation of the Al_4C_3 phase as indicated in solidification sequence (Fig. 5.15 (b)). The C element remains in the liquid phase after the formation of the phase TiC and then forms the Al_4C_3 phase as indicated in component partitioning (Fig. 5.15 (d)). It is revealed that the formation of Al_3Ti or Al_4C_3 is determined depending on the relative amount of the C and Ti elements.

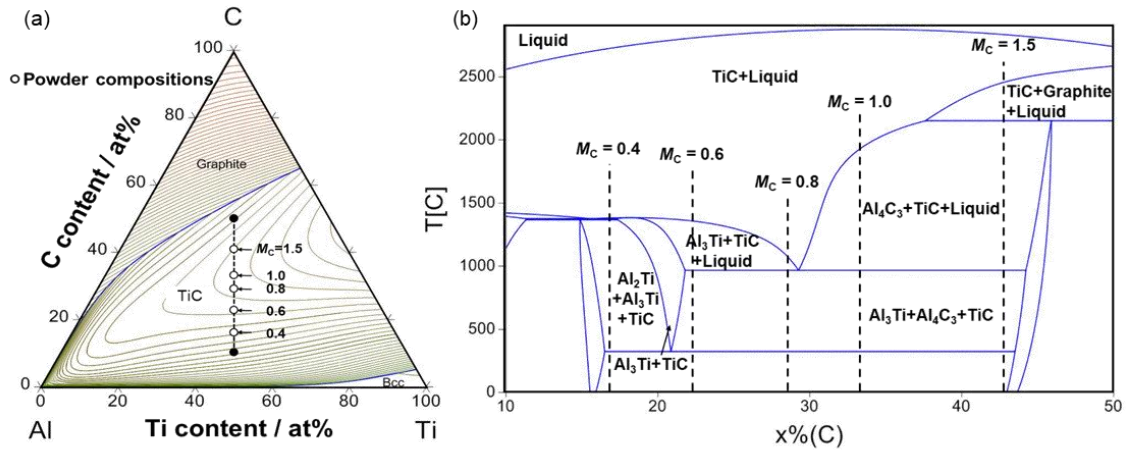


Fig. 5.14 (a) Liquidus projection of Al-Ti-C ternary system and (b) its vertical section of equilibrium phase diagram at Al/Ti = 1.0.

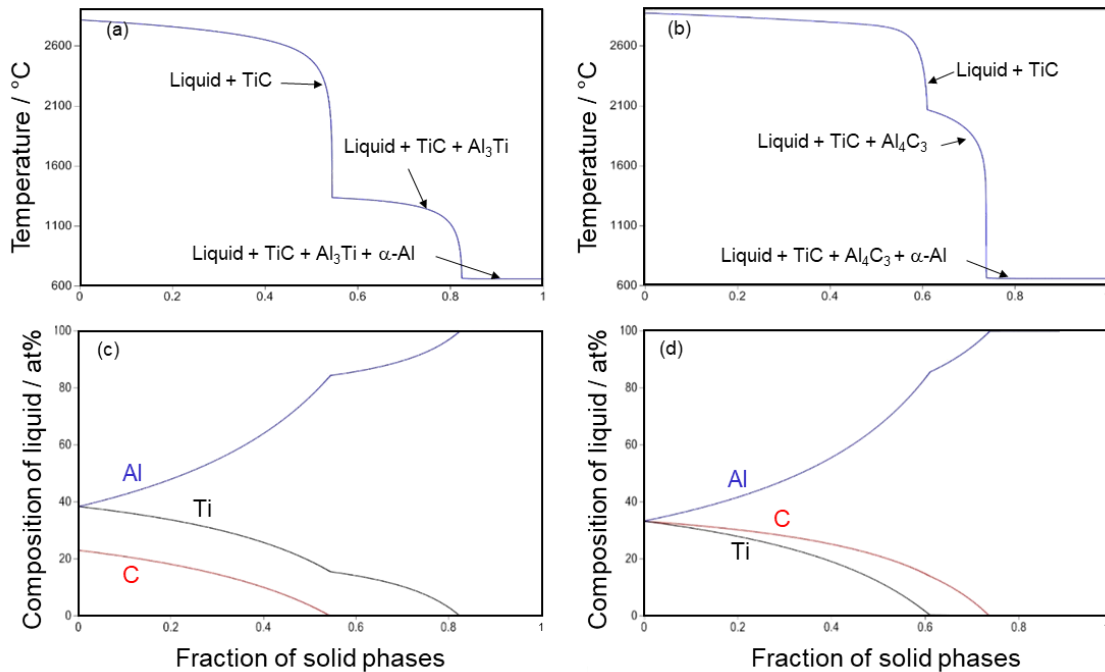


Fig. 5.15 (a, b) Solidification sequence and (c, d) component partitioning in liquid phase during solidification calculated based on Scheil assumption: (a, c) $M_C = 0.6$ and (b, d) $M_C = 1.0$.

The changes in mole fractions of final solid phases (Al_4C_3 , TiC, and Al_3Ti) calculated based on the Scheil solidification assumption as a function of M_C is summarized in **Fig. 5.16**. It is noteworthy that the TiC mole fraction indicates maximum at $M_C = 0.8$. Considering the TiC phase formed the skeleton structure in granular protrusions (**Fig. 3.8**), large amount of TiC phase facilitated the formation of granular protrusions. The calculated final mole fraction of TiC phase is in good agreement with the changes in the experimentally evaluated projected area fraction (**Fig. 5.5**). In the case of low M_C (0.4 and 0.6), the mole fraction of the Al_3Ti phase indicates high value, while the Al_4C_3 phase formation is low. In the case of high M_C (0.8, 1.0, and 1.5), the mole fraction of the Al_3Ti phase decreased rapidly in contrast to the formation of the Al_4C_3 phase. These calculation results are consistent with the experimentally measured XRD results (**Fig. 5.8**). In the case of the starting powder with low M_C , the Ti content was redundant in the liquid phase and formed the Al_3Ti phase by reacting with the Al element supplied from not only the starting powder but also the Al substrate. The reaction between the Ti powder and Al substrate formed the Al_3Ti phase below the surface of the Al substrate (**Fig. 5.11 (a)**), resulting in increasing the bonding ratio. When the starting powder with high C content was used, the Al_3Ti phase was hardly formed due to the lack of the Ti element. The Al_3Ti phase was rarely observed in the near Al substrate (**Fig. 5.11 (b)**). The bonding ratio decreased because the interfacial reaction between the Ti powder and Al substrate did not occur much.

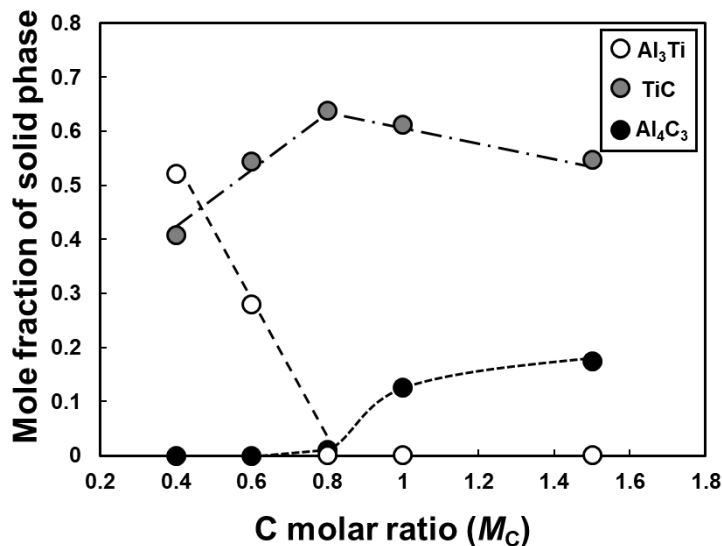


Fig. 5.16 The final mole fraction of solid Al_4C_3 , TiC and Al_3Ti phases as a function of C molar ratio (M_C) calculated based on the Scheil assumption.

An $\text{Al}_4\text{C}_3/\text{Al}$ composite was synthesized with graphene oxide and Al powder mixture by laser powder bed fusion method according to Zhou et al. [5.6]. The Al_4C_3 had rod-like morphology with diameter of < 140 nm and dispersed in the Al matrix. In the present study, it was not found any contribution from the Al_4C_3 phase to the structure of granular protrusions. This

may stem from the Al_4C_3 phase generated with very small size and dispersed into molten powder or Al substrate. Minute observations of the anchor layer are required in future works.

5.4.2. Mechanical behaviors of Al/PA6 joint via the anchor layer

When the anchor layer was fabricated using starting powders with high M_C (0.8, 1.0, and 1.5), granular protrusions severely fractured from the Al substrate (**Fig. 5.13**). The anchor layers fabricated using the starting powders with $M_C = 0.8, 1.0,$ and 1.5 indicated low bonding ratio and fractured easily when high external force was applied, resulting in low F_{USF} . In the case of the anchor layer fabricated using the starting powder with $M_C = 0.4$, the projected area fraction was low although the bonding ratio was high. The granular protrusions were not formed around the centerline of the laser irradiated region, which means interlocking sites for PA6 were not enough to exhibit high F_{USF} . When the anchor layer was fabricated using starting powder with $M_C = 0.6$, both the bonding ratio and projected area fraction were high. Granular protrusions were homogeneously distributed on the laser scanned region and adhered well with the Al substrate. The granular protrusions were hardly fractured from the Al substrate and PA6 remained among the granular protrusions. The strong interlocking between PA6 and the granular protrusions provided the highest F_{USF} . Obviously, the bonding ratio and projected area fraction influenced the joint strength. The area of the anchor layer should be considered because the F_{USF} will increase if the area becomes larger. Therefore, the F_{USF} was divided by the surface area and the ultimate shear stress (F_{USS}) was obtained.

Changes in the joint strength (F_{USF} and F_{USS}) with the projected area fraction and bonding ratio are shown in **Fig. 5.17 (a)** and **(b)**, respectively. There is no correlation indicated from these graphs. **Figure 5.17 (c)** shows the relationship between the joint strength (F_{USF} and F_{USS}) and product of bonding ratio and projected area fraction. The F_{USF} and the bonding ratio \times projected area fraction had linear correlation. The F_{USS} slightly increased with increasing the product of the bonding ratio and projected area fraction and rapidly increased especially when the product became 0.5. The joint strength including difference in the area of the anchor layer (F_{USS}) was also the highest. However, further investigation is needed to see if the above correlation between the joint strength and the product of the bonding ratio and projected area fraction applies even if the shape of the granular protrusion changes.

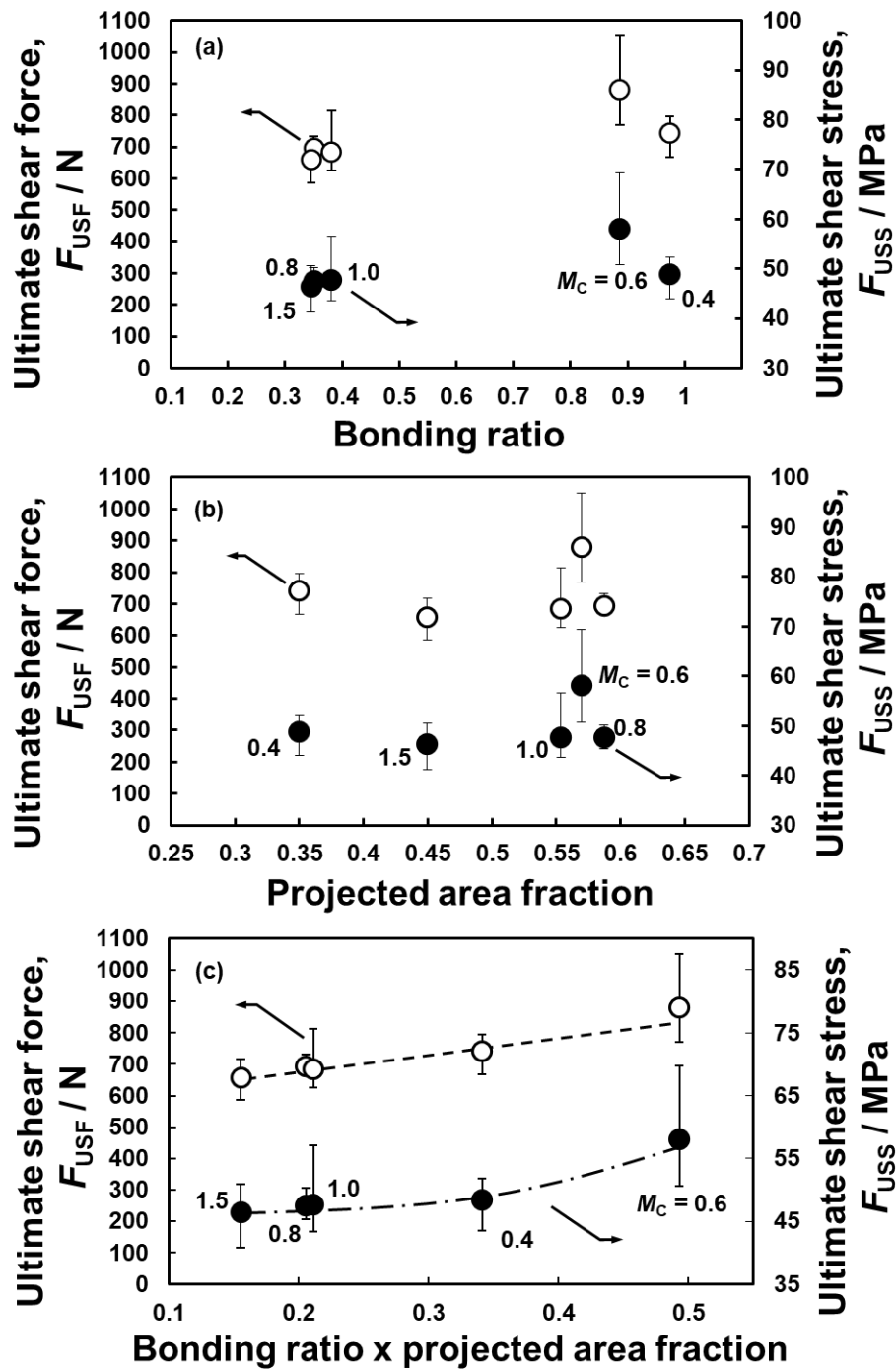


Fig. 5.17 Changes in F_{USF} and F_{USS} of Al/PA6 lap joint as a function of (a) bonding ratio, (b) projected area fraction, and (c) bonding ratio x projected area fraction.

5.5. Summary

- The morphology of the anchor layer changed depending on the C molar ratio in the Al-Ti-C powder blends.
- It was found from Scheil solidification simulation and phase identification that the TiC phase was primary phase during solidification process, followed by the formation of Al₃Ti or Al₄C₃ secondary phases. In the case of low M_C (0.4 and 0.6), the Al₃Ti phase was preferably generated, in contrast to the Al₄C₃ phase.
- The projected area fraction changed depending on M_C . This was related with final mole fraction of the TiC solid phase after solidification because the TiC phase forms the skeleton structure in the granular protrusion.
- The bonding ratio changed depending on M_C . The interfacial reaction between the Ti powder and Al substrate to form Al₃Ti at low M_C (0.4 and 0.6) improved in the bonding ratio.
- Lap shear tests and fracture surface observations revealed that both high bonding ratio and projected area fraction were required to obtain high Al/PA6 joint strength. Homogeneously distributed granular protrusions well-bonded with the substrate provided stiff interlocking sites for resisting high external force by distributing through the anchor layer.

Reference

- [5.1] PanAluminum. Thermodynamic database for commercial aluminum alloys. Computherm LLC, 8401 Greenway Blvd Suite 248, Middleton, WI 53562, USA (2016)
- [5.2] Takata, N., Okano, T., Suzuki, A., Kobashi, M. Microstructure of intermetallic-reinforced Al-Based alloy composites fabricated using eutectic reactions in Al–Mg–Zn ternary system. *Intermetallics*. 2018, 95, 48-58.
- [5.3] Lavernia, E. J., Ayers, J. D., Srivatsan, T. S. Rapid solidification processing with specific application to aluminum alloys. *International materials reviews*. 1992, 37(1), 1-44.
- [5.4] Yang, J., Huang, J., Ye, Z., Chen, S., Ji, R., Zhao, Y. Influence of interfacial reaction on reactive wettability of molten Ag-Cu-X wt.% Ti filler metal on SiC ceramic substrate and mechanism analysis. *Applied Surface Science*. 2018, 436, 768-778.
- [5.5] Emamian, A., Corbin, S. F., Khajepour, A. The influence of combined laser parameters on in-situ formed TiC morphology during laser cladding. *Surface and Coatings Technology*. 2011, 206(1), 124-131.
- [5.6] Zhou, W., Dong, M., Zhou, Z., Sun, X., Kikuchi, K., Nomura, N., Kawasaki, A. In situ formation of uniformly dispersed Al₄C₃ nanorods during additive manufacturing of graphene oxide/Al mixed powders. *Carbon*. 2019, 141, 67-75.

6. Structural control of anchor layer by changing laser conditions for enhancing Al/PA6 lap joint strength

6.1. Introduction

Structural control of the anchor layer is important since the bonding strength of directly joined metal/polymer hybrid structures significantly depends on the structure of metal surface at bonded area as mentioned in 1.3.1 section. Kurakake et al. [6.1] carried out laser spot joining to join polyethylene terephthalate (PET) and aluminum alloy (A5052) sheets. The joint strength of the Al/PET hybrid structure changed depending on the laser heat input. The cross-sectioned joint sample observation revealed that a cavity was formed on the Al surface and the depth of the cavity changed depending on the laser heat input. Byskov-Nielsen et al. [6.2] carried out laser drilling on a metal surface. The authors found that the morphology of the holes changed depending on the laser energy. These researches would open the possibility of controlling the structure of the anchor layer by changing laser parameters. In the present study, the effects of laser parameters (laser power (P) and scan speed (v)) on the structure of the anchor layers were investigated. An energy density (E_d) is used in laser processes including welding and additive manufacturing. The energy density is the total energy divided by the dimension of the region where is irradiated by laser. In the present study, the following linear energy density (E_d^L) was used [6.3].

$$\text{Linear energy density } (E_d^L) = \frac{P}{v} \quad (6.1)$$

The structure of the anchor layer was evaluated quantitatively and correlated with E_d^L . The mechanical properties of Al/PA6 hybrid structure were evaluated by the lap shear tests and fracture surface analysis. The mechanical properties were correlated with E_d^L and the quantities representing the anchor structures. The findings were used to discuss the relationship among the laser process conditions, the structure of the anchor layers, and the mechanical behaviors of Al/PA6 lap joints.

6.2. Experimental methods

The process for fabricating the anchor layer was the same as explained in section 3.2. The molar ratio of Al-Ti-C powder mixture was fixed as 1:1:0.6, which was proved to be the optimized condition in Chapter 5. Laser powers were controlled at 300 and 400 W, while the laser scan speeds were set at 10, 30, 50, 70, and 100 mm/s. After the laser irradiation, the top-view of the anchor layers was observed using the SEM.

The cross-sectioned anchor layer was observed using the SEM (back scattered electron mode). The cross-sectioning method for the anchor layer was the same method as explained in

section 3.2. The EDS analysis was conducted with the cross-sectioned anchor layer to acquire element maps (Al, Ti, and C) and line-scan analysis results.

The anchor structures were quantified by image-analyzing the SEM images with ImageJ software. The projected area fraction (F_{pa}) and bonding ratio (B_r) were evaluated by the same methods as explained in 5.2 section. Average width (w) and height (h) of granular protrusions were measured using the SEM images of the cross-sectioned anchor layers. The height was measured from the surface of the substrate near the granular protrusion as indicated in **Fig. 6.1**. The aspect ratio (A_r) was calculated using the width and height with the following equation.

$$\text{Aspect ratio } (A_r) = \frac{h}{w} \quad (6.2)$$

Two sample images were used for calculating the projected area fraction and more than 20 granular protrusions were used for calculating the bonding ratio, width, height and aspect ratio.

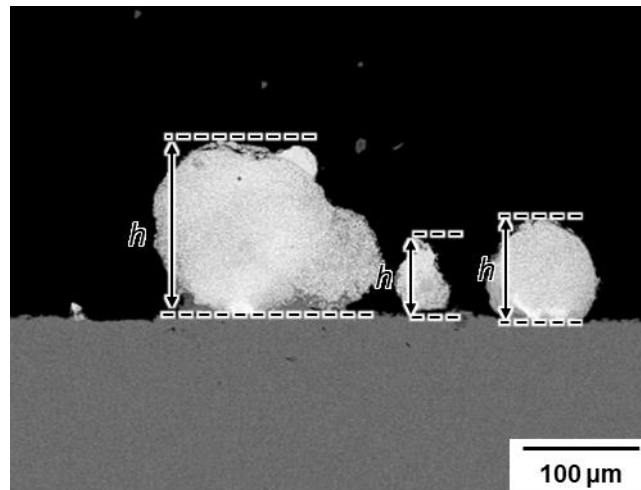


Fig. 6.1 Representative image used for evaluating the height (h) of the granular protrusions.

Hot-pressing was used to join the Al and PA6 substrates. The joining process was same as the process explained in 4.2.1 section. In this study, T_{JC} (joining complete temperature) of 190 °C was applied for all joint fabricating process. The dimension of the Al/PA6 lap joint is shown in **Fig. 5.2**. Lap shear test was conducted as same method and conditions as explained in 3.2 section. Basically, three Al/PA6 lap joint samples were used to obtain the average ultimate shear force (F_{USF}) for each laser condition. Two Al/PA6 lap joints via the anchor layer fabricated under the laser power of 300 W for the laser scan speed of 10, 50, and 100 mm/s were used to obtain the average F_{USF} . After the lap shear tests, fracture surfaces of the anchor layer were observed using the SEM.

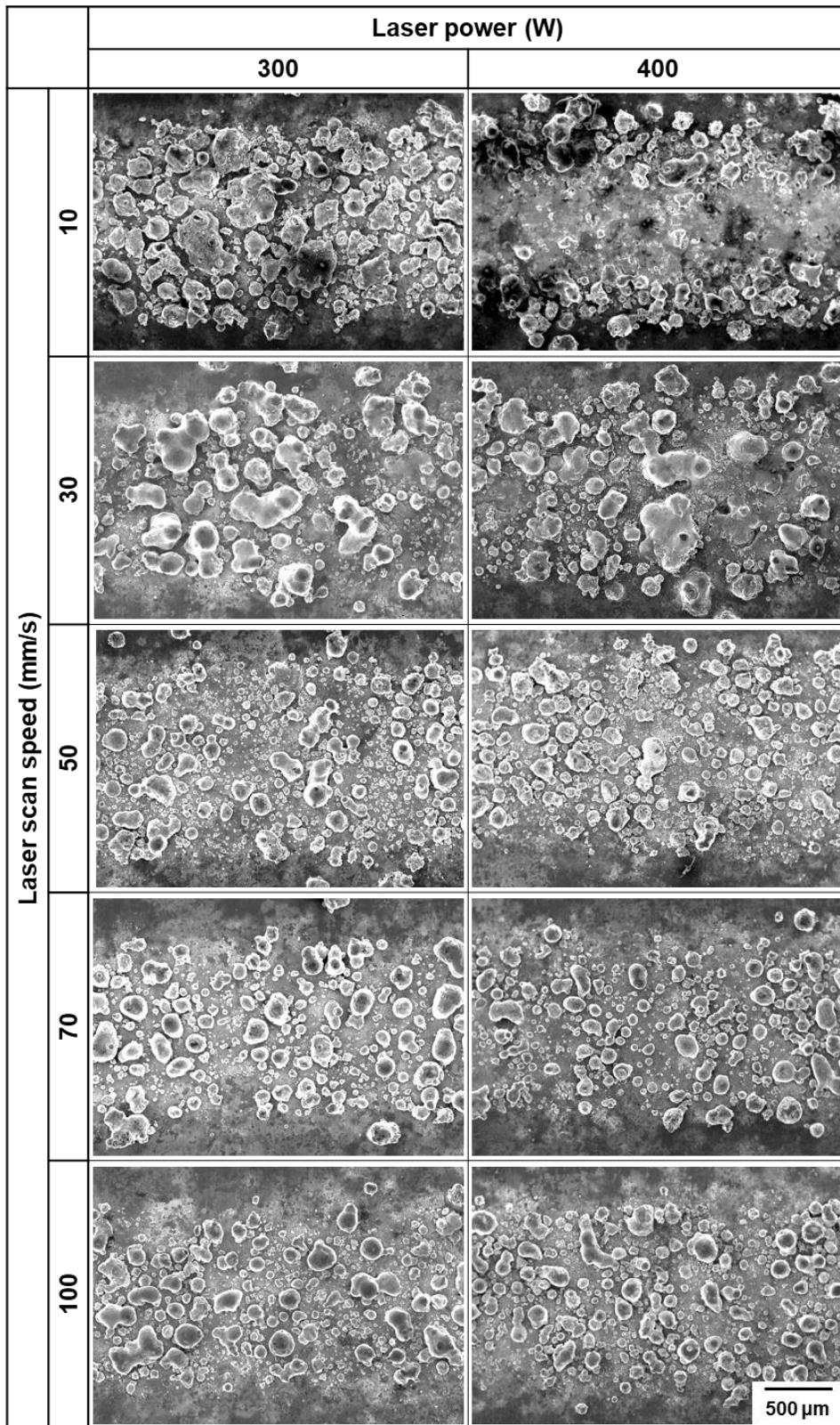


Fig. 6.2 SEM micrographs showing the top-view of the anchor layers fabricated under different laser power and scan speed.

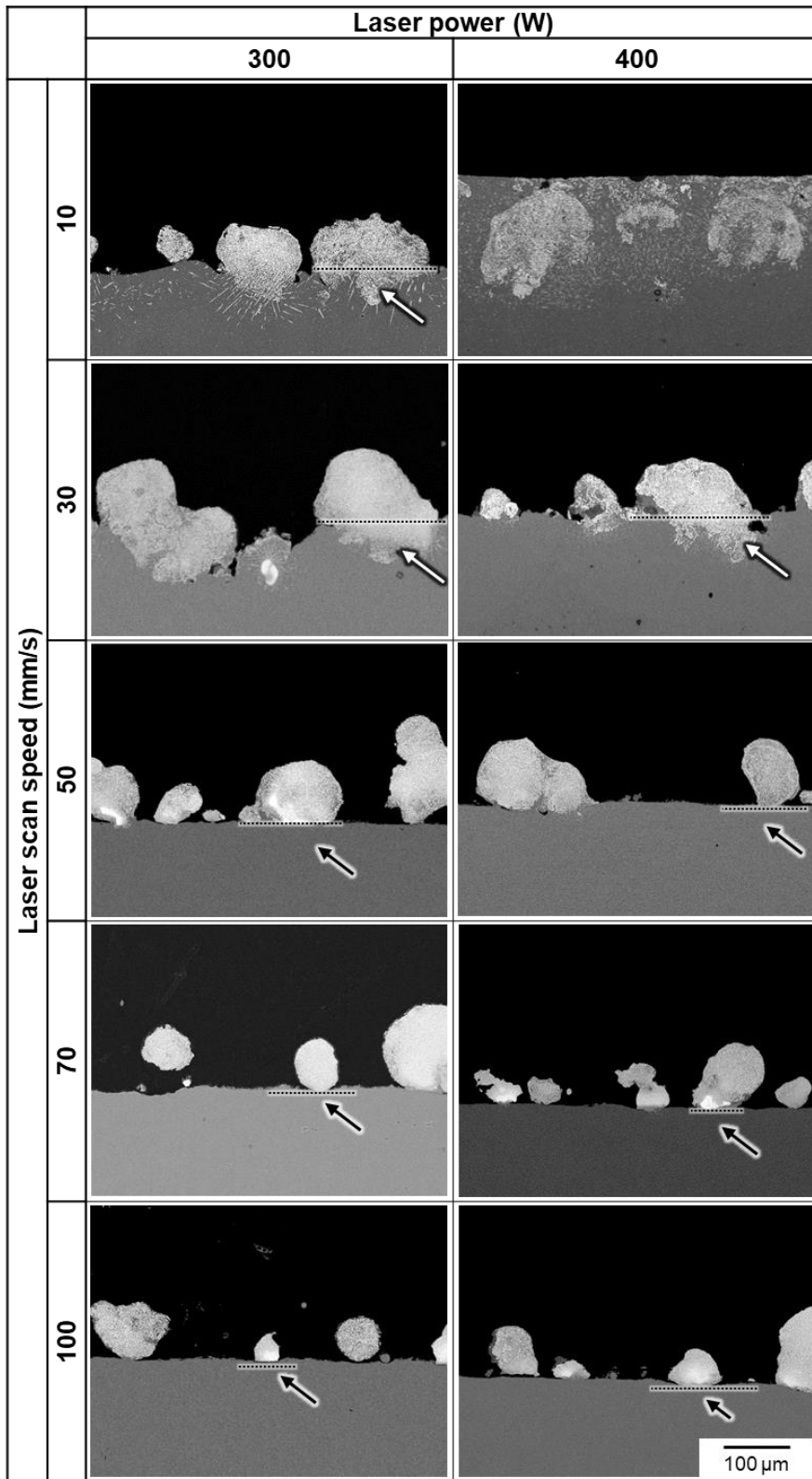


Fig. 6.3 SEM micrographs showing the cross-sectioned anchor layers fabricated under different laser power and scan speed.

6.3. Results

6.3.1. Characteristics of the anchor layers

Representative SEM micrographs showing the top-view anchor layer fabricated under different laser parameters are shown in **Fig. 6.2**. When the laser power was 300 W, the granular protrusions were homogeneously generated under all the laser scan speeds applied in this study. When the laser power was 400 W, the granular protrusions were generated under all the laser scan speed. However, the granular protrusions were scarcely observed around the centerline of the laser track in the case of 10 mm/s.

The SEM images of the cross-sectioned anchor layers are shown in **Fig. 6.3**. In the case of the laser conditions of 300 W and 10 mm/s, 300 W and 30 mm/s, and 400 W and 30 mm/s, the granular protrusions were intimately bonded with the Al substrate. The adhesiveness between the granular protrusions and Al substrate was poor when the laser conditions were 300 W and 50 ~ 100 mm/s and 400 W and 50 ~ 100 mm/s. The granular protrusions were filled with a phase with brighter contrast. The phase with brighter contrast was found below the interface between the granular protrusions and Al substrate when the anchor layer was fabricated under the laser conditions of 300 W and 10 mm/s, 300 W and 30 mm/s, and 400 W and 30 mm/s (indicated by the white arrows in **Fig. 6.3**). The phase with brighter contrast was rarely found below the interface when the anchor layer was fabricated under the laser conditions of 300 W and 50 ~ 100 mm/s and 400 W and 50 ~ 100 mm/s (indicated by the black arrows in **Fig. 6.3**). In the case of the laser conditions of 400 W and 10 mm/s, the granular protrusions were not formed on the surface of Al substrate, instead it seemed that the granular protrusions submerged into the substrate.

Figure 6.4 shows the changes in the quantities representing the anchor structures fabricated under different laser conditions as a function of E_d^L . The anchor layer fabricated under the laser conditions of 400 W and 10 mm/s was not quantified since no granular protrusions were observed from the cross-sectioned image. The bonding ratio increased with E_d^L from 3.0 to 10.0 J/mm and became constant at approximately 0.85 when E_d^L exceeded 10.0 J/mm. The projected area fraction and width indicated constant value when E_d^L was in the range of 3.0 ~ 10.0 J/mm and increased monotonically with an increase in E_d^L from 10.0 to 30.0 J/mm. The height and aspect ratio were almost constant when E_d^L was in the range of 3.0 ~ 10.0 J/mm and decreased with an increase in E_d^L from 10.0 to 30.0 J/mm. It was revealed that the quantities representing the anchor structures changed significantly at E_d^L around 10.0 J/mm.

The SEM images showing the cross-sectioned granular protrusion in the anchor layer fabricated below and above E_d^L of 10.0 J/mm are shown in **Fig. 6.5** ($E_d^L = 3.0$ J/mm) and **Fig. 6.6** ($E_d^L = 13.3$ J/mm), respectively. In the middle region of the granular protrusion (surrounded by dotted line), two phases were observed in both of $E_d^L = 3.0$ and 13.3 J/mm cases. The Ti and

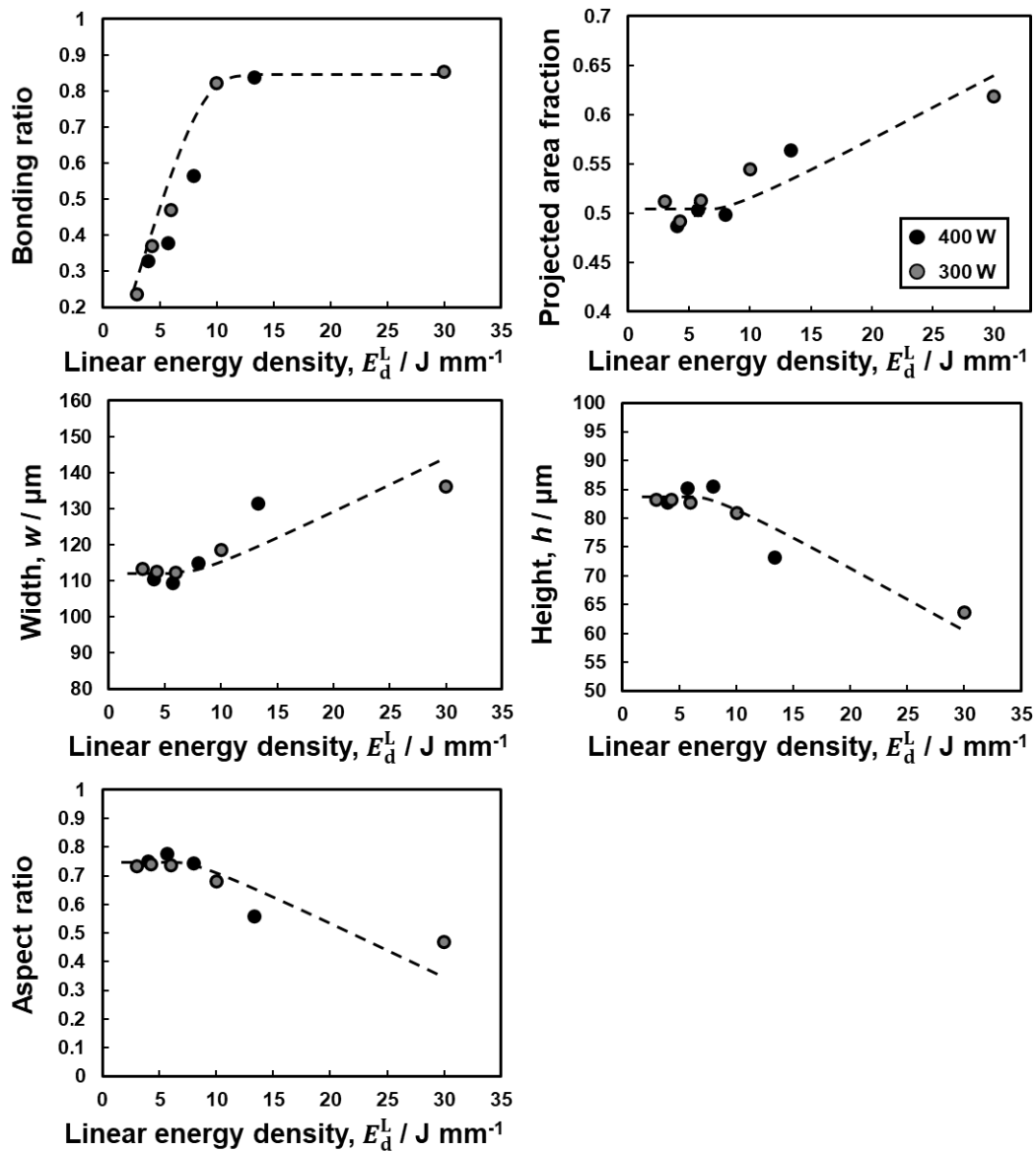


Fig. 6.4 Changes in the bonding ratio, projected area fraction, height, width, and aspect ratio of the granular protrusions as a function of linear energy density (E_d^L).

C elements were detected in the brightest phase, which is regarded as the TiC identified in Chapter 5. The TiC phase was encompassed by an Al-Ti intermetallic compound, which is regarded as the Al_3Ti identified in Chapter 5.

Different microstructures were observed in the region near the substrate depending on E_d^L . In the case of $E_d^L = 3.0$ J/mm (**Fig. 6.5**), the phase with the brightest contrast was observed just above the interface between the granular protrusion and Al substrate (surrounded by solid line). The magnified SEM image and elements maps indicated that the phase with the brightest contrast was a Ti-rich phase. The Ti element was also detected around the Ti-rich phase. The Al element was detected around the Ti-rich phase and below the interface. The C element was mainly

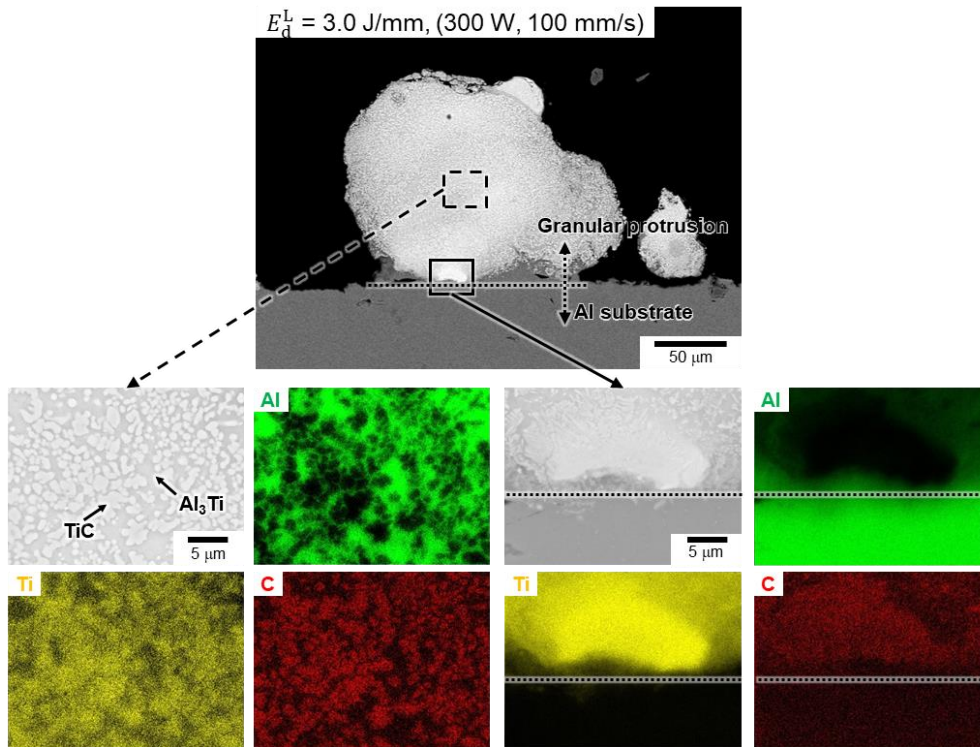


Fig. 6.5 SEM images and element maps (Al, Ti and C) of a cross-sectioned granular protrusion in the anchor layer fabricated with $E_d^L = 3.0 \text{ J/mm}$.

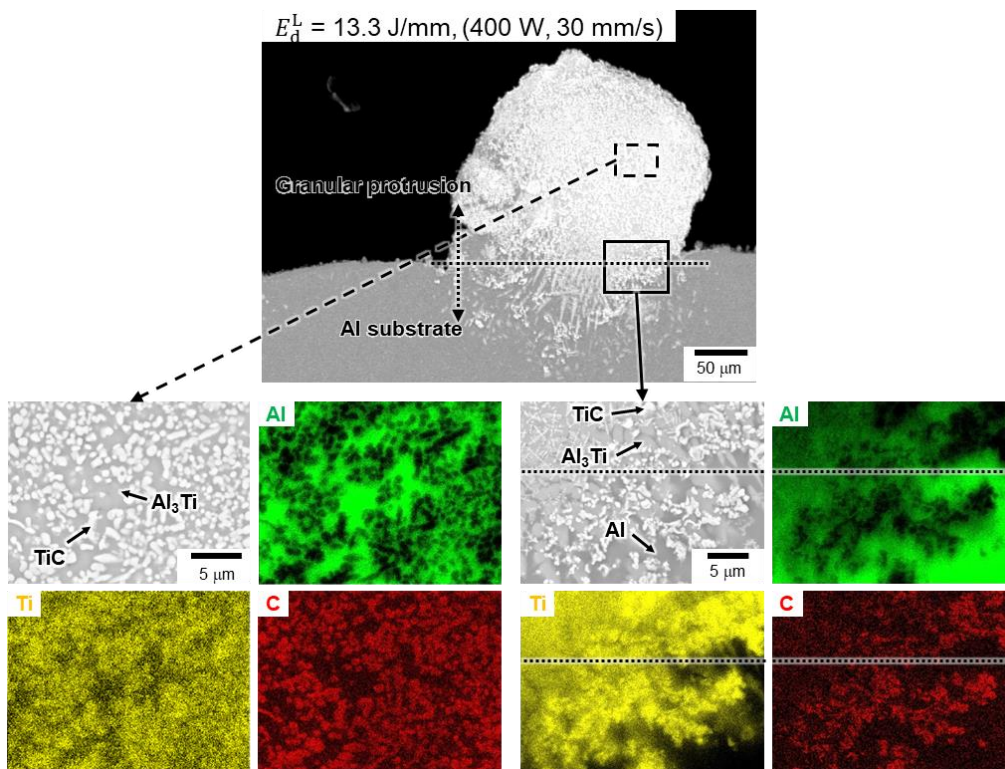


Fig. 6.6 SEM images and element maps (Al, Ti and C) of a cross-sectioned granular protrusion in the anchor layer fabricated with $E_d^L = 13.3 \text{ J/mm}$.

detected above the interface. **Figure 6.7 (a)** shows line-scan EDS analysis result for Al and Ti elements in the direction perpendicular to the interface between the granular protrusion and Al substrate (indicated by dotted horizontal line). The molar concentration of the Ti element was less than 1% below the interface and rapidly increased around the interface in contrast to the Al element.

In the case of $E_d^L = 13.3$ J/mm, three phases with different contrast were confirmed around the interface between the granular protrusion and Al substrate (surrounded by solid line) as indicated in **Fig. 6.6**. The phase with the brightest contrast was the TiC because the C and Ti elements were detected. The TiC phase was distributed in the region near the Al substrate. The Al and Ti elements were detected in the middle contrast phase, which was regarded as the Al_3Ti phase. **Figure 6.7 (b)** shows line-scan EDS analysis result for Al and Ti elements in the direction perpendicular to the interface between the granular protrusion and Al substrate (indicated by dotted horizontal line). The molar concentration of Ti element below the interface was in the

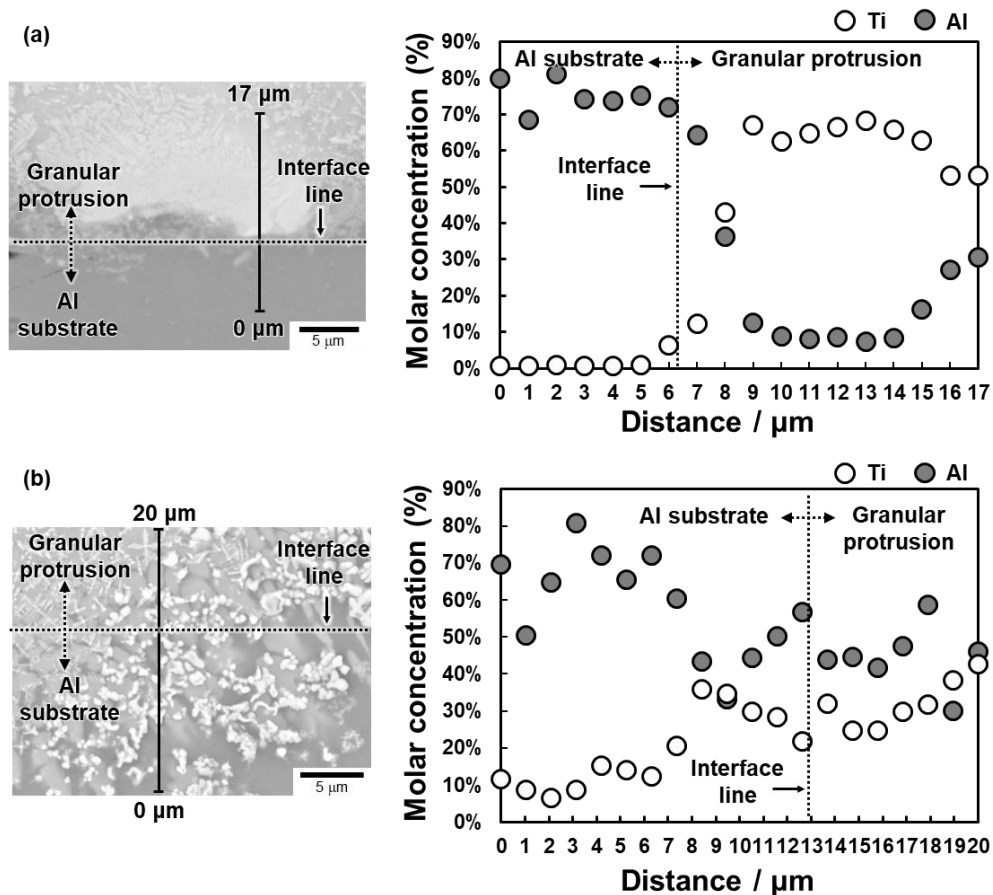


Fig. 6.7 SEM images of the cross-sectioned granular protrusion in near the substrate region and changes in molar concentration of Al and Ti elements along with the vertical line in the SEM micrograph: (a) $E_d^L = 3.0$ J/mm and (b) $E_d^L = 13.3$ J/mm.

range of 6 ~ 36%, which was much higher than in the case of $E_d^L = 3.0$ J/mm. The Al and Ti elements in the substrate around the interface were detected almost the same level in the granular protrusion.

6.3.2. Mechanical behaviors of Al/PA6 lap joints

Changes in the average ultimate shear force (F_{USF}) of Al/PA6 lap joints via the anchor layer fabricated under different E_d^L are shown in **Fig. 6.8**. Error bars indicate the difference between minimum and maximum values. The F_{USF} increased with an increase in E_d^L from 3.0 to 10.0 and decreased with an increase in E_d^L from 10.0 to 30.0.

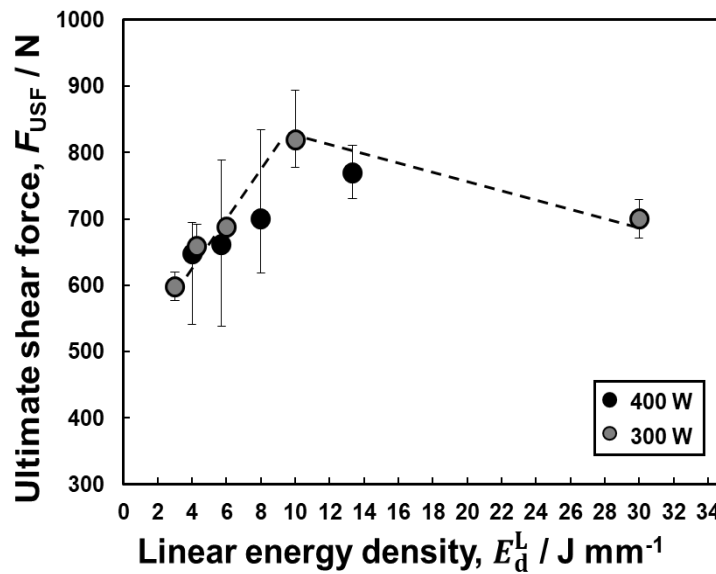


Fig. 6.8 Changes in F_{USF} of Al/PA6 lap joints as a function of linear energy density (E_d^L) of the laser source.

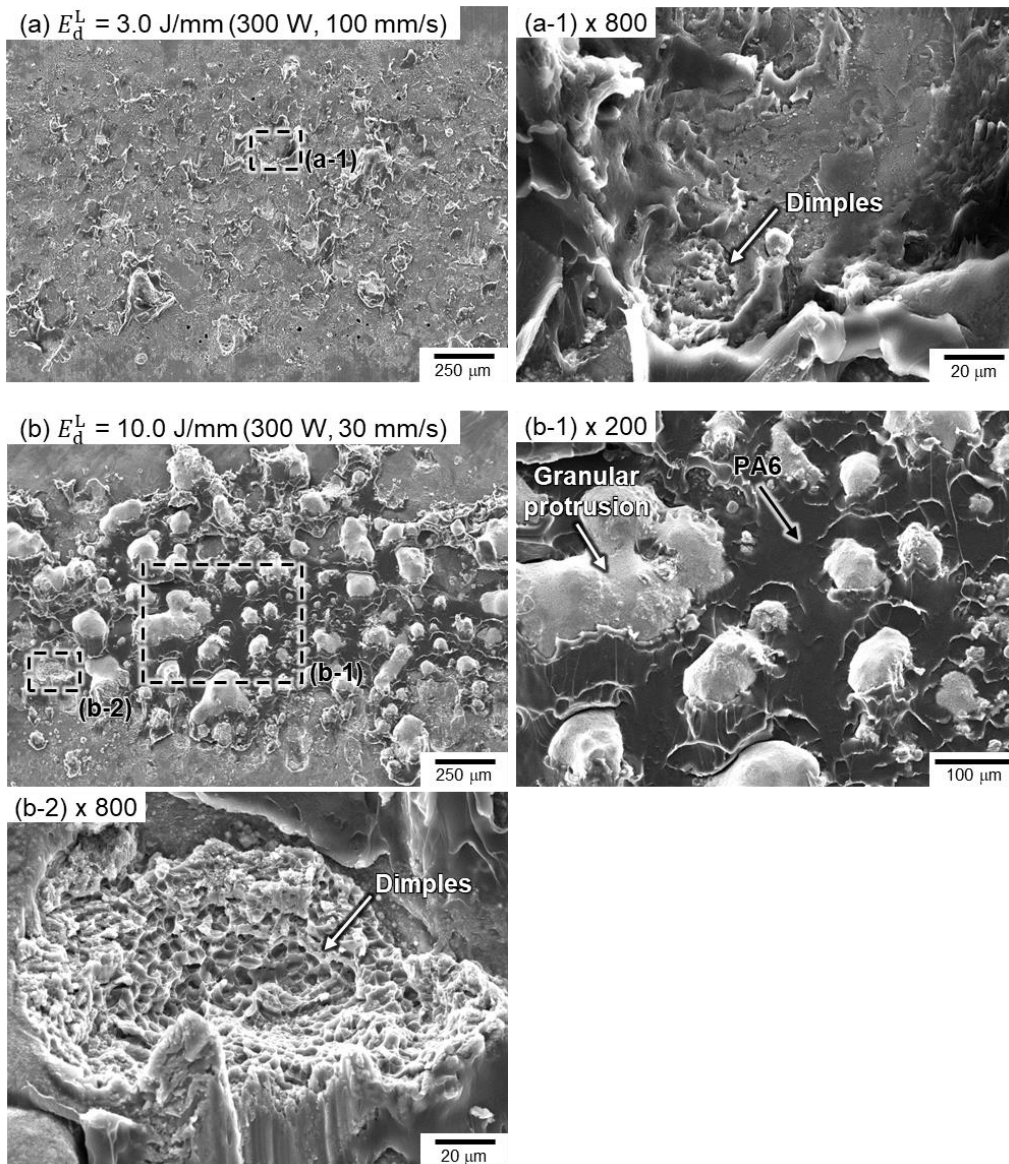
Figure 6.9 shows SEM micrographs of the fracture surfaces on the Al substrate sides after the shear tests of the joints via the anchor layers fabricated under E_d^L of 3.0, 10.0, and 13.3 J/mm. The PA6 substrate was pulled upward direction in the images.

In the case of $E_d^L = 3.0$ J/mm (**Fig. 6.9 (a)**), remaining granular protrusions and PA6 were hardly observed on the Al substrate. **Figure 6.9 (a-1)** show high-magnification SEM images of the fracture surface. Dimples were observed (indicated by the white arrow) on the magnified fracture surface. It was thought that the dimples were formed when the bonded part of the granular protrusion with the Al substrate were fractured due to the external force. The diameter of the region where the dimples were formed was about 20 μ m.

In the case of $E_d^L = 10.0$ J/mm, PA6 and granular protrusions remained on the fracture surface as indicated in **Fig. 6.9 (b)**. **Figure 6.9 (b-1)** and **(b-2)** show high-magnification SEM images of the fracture surface. As indicated in **Fig. 6.9 (b-1)**, the granular protrusions were hardly

fractured (indicated by the white arrow) and PA6 remained among the granular protrusions (indicated by the black arrow). PA6 did not remain on the top surface of the granular protrusions. Dimples were formed on the Al substrate as indicated in **Fig. 6.9 (b-2)**. The size of the region where the dimples were formed in the case of $E_d^L = 10.0 \text{ J/mm}$ was larger than that in the case of $E_d^L = 3.0 \text{ J/mm}$.

Figure 6.9 (c) shows the anchor layer after the lap shear test in the case of $E_d^L = 13.3 \text{ J/mm}$. The granular protrusions and PA6 remained on the fracture surface. High-magnification SEM images of the fracture surface are indicated in **Fig. 6.9 (c-1)** and **(c-2)**. As indicated in **Fig. 6.9 (c-1)**, PA6 remained around the granular protrusions (indicated by the black arrows). Granular protrusions around which PA6 did not remain (indicated by the white arrow with dotted line) and a small amount of PA6 remained (indicated by the white arrow with solid line) were also observed.



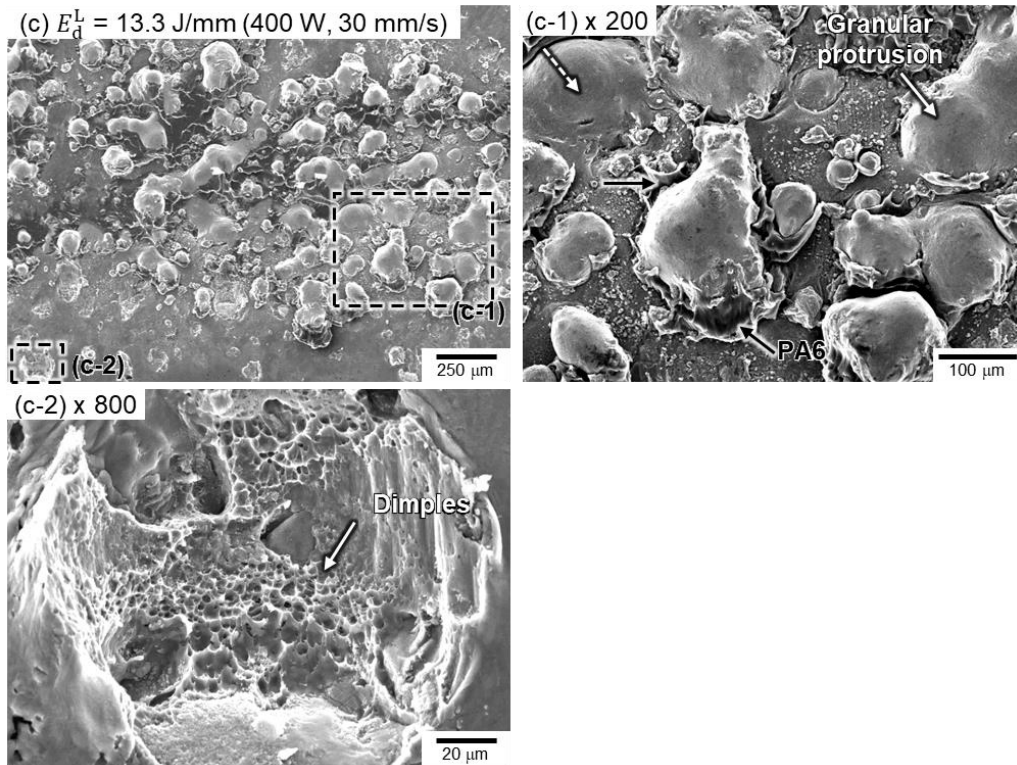


Fig. 6.9 SEM images of the low and high-magnification fracture surfaces on the Al substrate of the Al/PA6 joints via the anchor layers fabricated with (a) $E_d^L = 3.0$ J/mm, (b) $E_d^L = 10.0$ J/mm and (c) $E_d^L = 13.3$ J/mm.

The size of the region where the dimples were formed in the case of $E_d^L = 13.3$ J/mm was larger than that in the case of $E_d^L = 3.0$ J/mm as indicated in **Fig. 6.9 (c-2)**.

6.4. Discussion

6.4.1. Characteristics of the anchor layers

The effect of the laser conditions on the anchor structures was examined. The quantities representing the anchor structures studied in this chapter changed significantly below and above $E_d^L = 10.0$ J/mm (**Fig. 6.4**). The bonding ratio increased with E_d^L from 3.0 to 10.0 J/mm and became constant with $E_d^L \geq 10.0$ J/mm. The projected area fraction and width were roughly constant when E_d^L was below 10.0 J/mm and increased as E_d^L was further increased. The height and aspect ratio were almost constant when E_d^L was below 10.0 J/mm and decreased as E_d^L was further increased. As shown in Chapter 5, the interfacial chemical reaction between the granular protrusions and Al substrate helped to increase the bonding ratio. The interfacial chemical reaction was thought to be responsible for the changes in the anchor structures in this chapter.

The microstructure of the cross-sectioned anchor layer changed depending on E_d^L . When the anchor layers were fabricated with $E_d^L < 10.0$ J/mm (300 W and 50 ~ 100 mm/s, and 400 W and 50 ~ 100 mm/s), the phase with brighter contrast (TiC and Al₃Ti) was hardly formed

below the interface between the granular protrusions and Al substrate (**Fig. 6.3**). In contrast, in the case of the anchor layers fabricated with $E_d^L \geq 10.0$ J/mm (300 W and 10 ~30 mm/s, and 400 W and 30 mm/s), the phase with brighter contrast was formed below and above the interface between the granular protrusions and Al substrate (**Fig. 6.3**). In addition, the granular protrusions and Al substrate were intimately bonded. In other words, metallurgical bonding between the granular protrusions and Al substrate was formed when high E_d^L was applied. The high-magnification SEM images and element maps revealed that the Ti-rich phase was observed just above the interface between the granular protrusion and Al substrate in the case of low E_d^L (3.0 J/mm) (**Fig. 6.5** and **6.7**). On the other hand, considerable amount of the Ti element was detected below the interface in the forms of Al_3Ti and TiC phases in the case of high E_d^L (13.0 J/mm) (**Fig. 6.6**, and **6.7**). It was found in chapter 5 that the chemical reaction at the interface between the Ti powder and Al substrate to generate the Al_3Ti phase played an important role to form metallurgical bonding at the interface and increase the bonding ratio. These findings suggest that enough energy needs to be provided from the laser source to induce chemical reactions at the interface, even if sufficient Ti element was provided from the molten powder blend. For inducing the interfacial chemical reaction, the laser conditions with $E_d^L \geq 10.0$ J/mm were required from the laser device used in this study. Note that the threshold energy density can change depending on other conditions including laser spot size and composition of the powder.

The fact that the interfacial chemical reaction occurred at the laser conditions of $E_d^L \geq 10.0$ J/mm suggests that the interfacial chemical reaction caused the changes in the quantities representing the anchor structure. In the case of Al sessile drop experiments on a ceramic substrate, a stable Al oxide is formed around the Al drop, which prevents wetting [**6.4**]. The wettability made a transition from poor to good at the testing temperature of 1000 °C, which was attributed to the breakup of the Al oxide film at high temperature. In this study, the temperature of the Al substrate and molten powders were increased with the increase in E_d^L , which might facilitate the breakup of the Al oxide and induce the interfacial chemical reaction. The interfacial chemical reaction occurred at high E_d^L conditions further improved wettability between the granular protrusions and the Al substrate. As a result, the bonding ratio of the anchor layers increased (**Fig. 6.4**). As indicated in Chapter 5, significant interfacial reaction to form Al_3Ti in the case of $Mc = 0.4$ (molar ratio of C) made granular protrusion sink into the substrate (**Fig. 5.6**), resulting in no granular protrusions around the centerline of the laser track (**Fig. 5.4**). Also in this chapter, granular protrusions formed below the substrate under the laser condition with high energy density (400 W, 10 mm/s) (**Fig. 6.3**). Therefore, the interfacial reaction promoted by low C content or high energy submerged granular protrusions into the substrate. The submerging decreased the height of the granular protrusions at higher energy density. The width of the granular protrusions increased since the granular protrusions might spread on the Al substrate due to the improvement

of the wettability at high E_d^L . As a result, the aspect ratio decreased. The increase in the width of the granular protrusions attributed to the increase in the projected area fraction. However, the detailed mechanism of the structural change with E_d^L needs further investigation.

6.4.2. Mechanical behaviors of Al/PA6 lap joints

The fact that the quantities representing the anchor structures changed significantly at $E_d^L = 10.0$ J/mm (Fig. 6.4) supports that the change in the joint strength at $E_d^L = 10.0$ J/mm (Fig. 6.8) was derived from the changes in the anchor structures.

Figure 6.10 shows changes in the F_{USF} with the quantities representing the anchor structures. Figure 6.10 (a) shows the relationship between the F_{USF} and the product of projected area fraction and bonding ratio. The joint strength shows a positive correlation with the product of projected area fraction and bonding ratio in the range of approximately 0.12 ~ 0.45 (corresponded to $E_d^L < 10.0$ J/mm) and a negative correlation with the product value of equal to or more than 0.45 (corresponded to $E_d^L \geq 10.0$ J/mm). These results suggested that the parameters other than projected area fraction and bonding ratio contributed to the change in the joint strength.

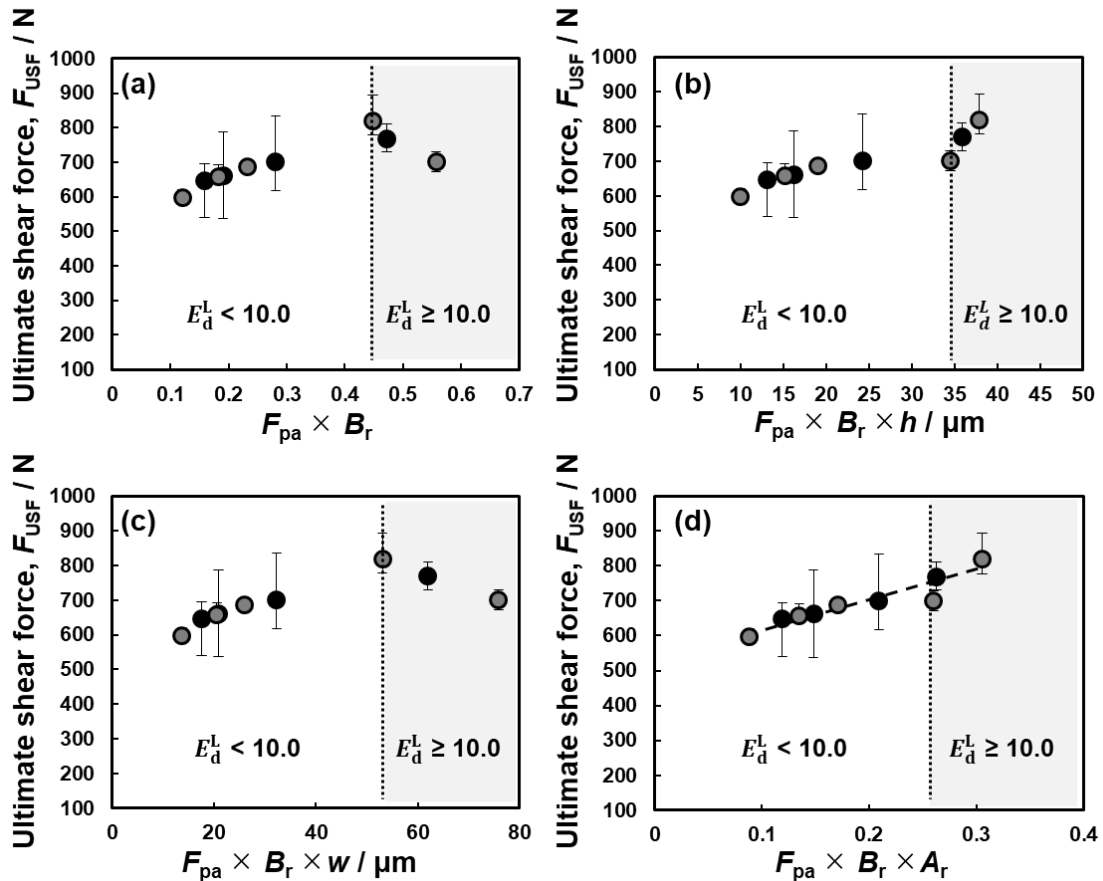


Fig. 6.10 Changes in the F_{USF} of Al/PA6 lap joints as a function of (a) projected area fraction (F_{pa}) \times bonding ratio (B_r), (b) $F_{pa} \times B_r \times$ height (h), (c) $F_{pa} \times B_r \times$ width (w), and (d) $F_{pa} \times B_r \times$ aspect ratio (A_r).

Figure 6.10 (b), (c), and (d) shows the relationship between the F_{USF} and projected area fraction \times bonding ratio \times height, projected area fraction \times bonding ratio \times width, and projected area fraction \times bonding ratio \times aspect ratio, respectively. The joint strength decreased also with increasing projected area fraction \times bonding ratio \times width over E_d^L value corresponding to 10 J/mm (**Fig. 6.10 (c)**). On the other hand, there was a positive correlation between the joint strength and the projected area fraction \times bonding ratio \times height (**Fig. 6.10 (b)**). Also, the joint strength increased almost linearly with an increase in the projected area fraction \times bonding ratio \times aspect ratio (**Fig. 6.10(d)**). These results indicated that the joint strength was improved by not only increasing the projected area fraction and bonding ratio but also generating tall granular protrusions.

When the anchor layer was fabricated with $E_d^L = 3.0$ J/mm, the joint strength was the lowest (**Fig. 6.8**) and granular protrusions and PA6 hardly remained on the fracture surface (**Fig. 6.9 (a)**). The size of the region where the dimples were formed was small (**Fig. 6.9 (a-1)**) compared to other anchor layers fabricated with high E_d^L (**Fig. 6.9 (b-2)** and **(c-2)**) since the fraction of bonded part of the granular protrusions with Al substrate (bonding ratio) was low. The granular protrusions were easily fractured when high external force was applied, which means the anchor layer was not strong enough to hold PA6.

In the case of $E_d^L = 10.0$ J/mm, the joint strength was the highest (**Fig. 6.8**). The anchor effect acted strongly since many granular protrusions interlocked with PA6 on the fracture surface (**Fig. 6.9 (b-1)**). Although some granular protrusions were fractured, it is considered that larger stress could be distributed to the fractured granular protrusions compared to the granular protrusions in the anchor layer with lower bonding ratio judged from the size of the region where the dimples were formed (**Fig. 6.9 (b-2)**). It is noteworthy that PA6 hardly remained on the top surface of the granular protrusions (**Fig. 6.9 (b-1)**), indicating that the top surface of the granular protrusions hardly contributed to the mechanical interlocking between the granular protrusions and PA6. The region of the top surface of a granular protrusion increases with an increase in the width of the granular protrusion. Therefore, the width of the granular protrusions influenced a negative impact on the joint strength (**Fig. 6.10 (c)**).

The joint strength of Al/PA6 lap joint decreased when E_d increased from 10.0 to 13.3 J/mm (**Fig. 6.8**). Some granular protrusions around which PA6 did not remain hardly contributed to mechanical interlocking (**Fig. 6.9 (c-1)**). A possible reason why PA6 did not interlock with the granular protrusions is that the height of the granular protrusions was low. The increase in the height of the granular protrusions might facilitate resisting larger external force since the area where the tall granular protrusions were entangled with PA6 was increased.

6.5. Summary

The anchor layers were fabricated with Al-Ti-C powder mixture under different laser power and scan speed. The effects of laser conditions on the structure and the microstructure of the anchor layer and joint strength of Al/PA6 hybrid structure via the anchor layer were investigated.

- The changes in the structural parameters of the anchor layers were described well with the linear energy density of the laser source (E_d^L). The quantities representing the anchor structures significantly changed around $E_d^L = 10$ J/mm.
- The anchor structures were influenced by the interfacial chemical reaction. The interfacial chemical reaction between the granular protrusions and Al substrate occurred severely at $E_d^L \geq 10.0$ J/mm.
- The joint strength of Al/PA6 hybrid structures changed depending on the quantities representing the anchor structures. The bonding ratio, projected area fraction, and height influenced a positive impact on the joint strength, while the width influenced a negative impact on the joint strength.

References

- [6.1] Kurakake, Y., Farazila, Y., Miyashita, Y., Otsuka, Y., Mutoh, Y. Effect of molten pool shape on tensile shear strength of dissimilar materials laser spot joint between plastic and metal. *Journal of Laser Micro Nanoengineering*. 2013, 8(2), 161.
- [6.2] Byskov-Nielsen, J., Balling, P. Laser structuring of metal surfaces: Micro-mechanical interlocking. *Applied surface science*. 2009, 255(10), 5591-5594.
- [6.3] Bourell, D., Coholich, J., Chalancon, A., Bhat, A. Evaluation of energy density measures and validation for powder bed fusion of polyamide. *CIRP Annals*. 2017, 66(1), 217-220.
- [6.4] Ferro, A. C., Derby, B. Wetting behaviour in the Al-Si/SiC system: interface reactions and solubility effects. *Acta metallurgica et materialia*. 1995, 43(8), 3061-3073.

7. Summary

This study aimed to strongly join metals and polymers via additively manufactured anchor layer. Firstly, to correctly understand the wetting phenomenon between metals and polymers, various surface treatments were performed on the Al surface. The surface purification greatly improved the wettability between the epoxy resin and the Al substrate. The atmospheric plasma treatment was effective for the surface purification. An attempt was made to additively fabricate the anchor layer on the Al substrate by laser-induced in-situ reaction. The Al-Ti-C powder blend was suitable for fabricating the anchor layer since it has complex structure with protrusive morphology. The anchor layer consisted of a number of micro-sized granular protrusions. The Al substrate with the anchor layer was joined with the PA6 substrate utilizing hot-pressing process. Furnace cooling below the crystallization ending temperature of PA6 was an effective method for increasing the degree of crystallinity, resulting in the high joint strength. In addition, it was demonstrated that the joining process utilizing the anchor layer is possible even at very low joining pressure below the melting point of polymer material.

The influence of process conditions for fabricating the anchor layer on the structure of the anchor layer was investigated for further strengthening of the Al/PA6 lap joint. Firstly, it was found that the molar ratio of C element in the Al-Ti-C powder blend influenced the structure and constitute phases of the anchor layer. It was revealed that the projected area fraction and bonding ratio significantly influenced the joint strength. Secondly, the structure of the anchor layer could be controlled by the volumetric energy density of the laser source. In addition to the projected area fraction and bonding ratio, the aspect ratio of the granular protrusions also influenced the joint strength.

In chapter 1, the social background for the necessity of the multi-material structure and dissimilar joining technique, and importance of the anchor effect in metal/polymer direct joining were described. Also, the conventional methods for metal surface structuring and joining methods for metals and polymers were reviewed. Based on the above, the importance and necessity of additively manufactured anchor layer and the purpose of this study were described.

In chapter 2, the importance of metal surface treatment for the direct metal/polymer joining was demonstrated through the wettability measurements between the Al substrate and various liquids (water and epoxy resin). The atmospheric plasma treatment improved the wettability between the Al substrate and liquid phases by removing organic impurities and forming Al oxides on the surface of the Al substrate.

In chapter 3, the Al-Ti and Al-Ti-C powder blends were tried to fabricate the anchor layer by laser-induced in-situ reaction. It was found that Al-Ti-C powder was suitable for

fabricating the anchor layer consisting of granular protrusions. The joint strength of approximately 45 MPa was obtained, which was more than twice as high as the required lap shear strength in the automobile industry (20 MPa). Homogeneously distributed granular protrusions provided mechanical interlocking sites for PA6, resulting in the high and reliable joint strength.

In chapter 4, the effect of joining temperature history on the mechanical behaviors of the Al/PA6 lap joints was investigated. It was shown that the degree of crystallinity of PA6 in the vicinity of Al/PA6 interface changes depending on the joining temperature history. When the joining process started at 215 °C, furnace cooling below 190 °C was effective for improving the joint strength because the degree of crystallinity was sufficiently increased.

In chapter 5, the influence of the C molar ratio in the Al-Ti-C powder blend on the characteristics of the anchor layer and joint strength was investigated. The formation of Al₃Ti and TiC phases, which can be controlled by the relative molar ratio of C and Ti powders, was related with the bonding ratio and projected area fraction. It was possible to fabricate the anchor layer with high projected area fraction and high bonding ratio which showed the highest joint strength by using the Al-Ti-C powder blend with the molar ratio of 1:1:0.6.

In chapter 6, the effects of the laser conditions on the characteristics of the anchor layer and joint strength were investigated. The interfacial reaction between the granular protrusions and Al substrate occurred when the linear energy density of the laser source was high enough ($E_d^L \geq 10.0 \text{ J/mm}$). The interfacial reaction changed the structure of the anchor layer significantly. It was revealed that the aspect ratio of the granular protrusions affected the joint strength in addition to the bonding ratio and projected area fraction.

The joint efficiency of metal/polymer single-lap joint structure of present study and previous researches are compared in **Fig. 7.1**. The joint efficiency was calculated by dividing the joint strength in [MPa] unit by the tensile strength of the weaker joint material (polymer). The bonded area of the metal/polymer joint is also indicated for a fair comparison since the joint strength in [MPa] unit decreases with increasing the bonded area as indicated in **Fig. 3.12**. **Table 7.1** summarizes the joining process, joining partners, bonded area, joint strength in [MPa] unit, and joint efficiency of the previous researches plotted in **Fig. 7.1**. If only the joint efficiency is considered, the present study indicates the highest joint efficiency. However, it is obvious that the bonded area of the lap joints must be increased while the joint efficiency is maintained high value for a practical use in the multi-material structure.

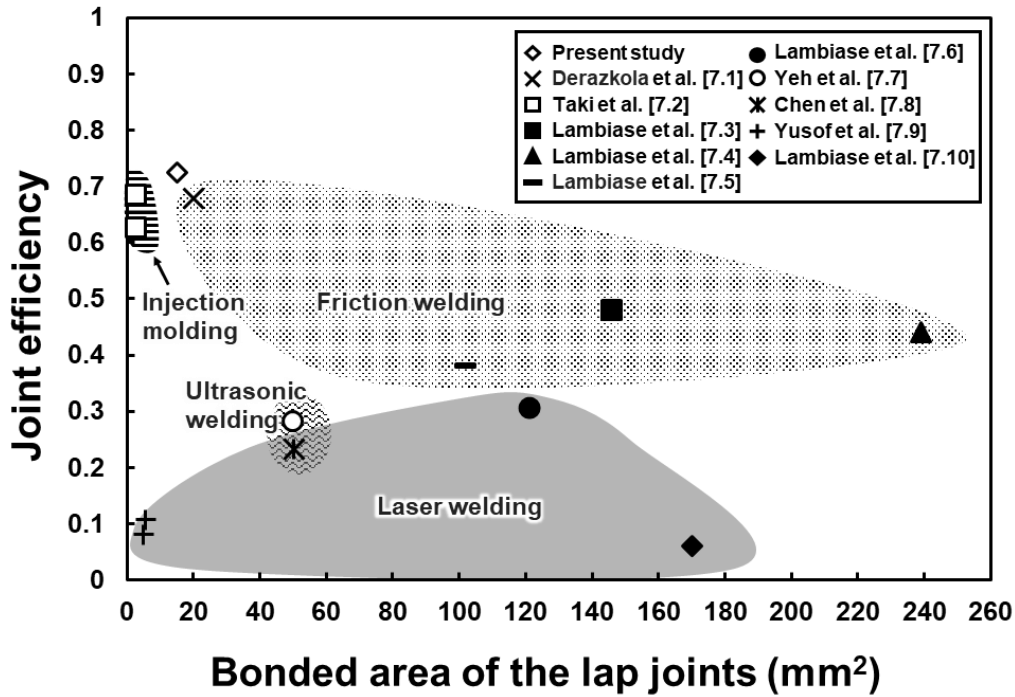


Fig. 7.1 Joint efficiency and bonded area of the metal/polymer lap joints of previous researches [7.1–7.10].

Table 7.1 Summary of previous metal/polymer joining researches [7.1-7.10].

Reference	Joining process	Metal	Polymer	Bonded area (mm ²)	Joint strength (MPa)	Joint efficiency
Present study	Hot-press	Al alloy (A5052) with anchor layer	PA6	15	58.0	0.73
[7.1]	Friction stir welding	As received Al alloy (A5058)	PC	20	46	0.69
[7.2]	Injection molded direct joining	Laser-textured Al alloy	PS	3	35.6	0.68
[7.3]	Friction stir spot welding	Laser-textured Al alloy (A5053)	PEEK	145.8	47	0.48
[7.4]	Friction stir spot welding	Laser-textured Al alloy (A5053)	PVC	238.9	16.1	0.44
[7.5]	Friction stir spot welding	Laser-textured pure Ti	PEEK	102	37.3	0.38
[7.6]	Laser spot welding	Laser-textured Al alloy (A5053)	PEEK	121	30.0	0.31
[7.7]	Ultrasonic welding	Laser-textured Al alloy (A5052)	ABS	50	11.0	0.28
[7.8]	Ultrasonic-aided laser welding	Surface cleaned pure Ti	PET	50	18.7	0.23
[7.9]	Laser spot welding	Anodized Al alloy (A5052)	PET	6	8.5	0.11
[7.9]	Laser spot welding	As received Al alloy (A5052)	PET	5	6.5	0.08
[7.10]	Laser welding	Stainless steel (AISI304)	PC	170	3.7	0.06

Future issues are discussed here. Although it was demonstrated that the lap shear strength of the Al/PA6 joint was excellent, it is necessary to show that the joint strength in the tensile direction perpendicular to the joint interface is high. The influence of the structure of the anchor layer on the joint strength was discussed to some extent by the fractography. Further research such as finite element method (FEM) analysis is required to gain a deeper understanding for the relationship between the joint strength and structure of the anchor layer. In addition, to increase the joint strength by controlling the structure of the anchor layer, it is necessary to investigate in detail the effects of the powder size and the molar ratio of the Al and Ti powders on the characteristics of the anchor layers and joint strength. Finally, it is necessary to apply the joining process utilizing the anchor layer to CFRTPs for more practical use. The optimization of joining condition for bonding the Al substrate and CFRTPs are required.

References

- [7.1] Derazkola, H. A., Elyasi, M. The influence of process parameters in friction stir welding of Al-Mg alloy and polycarbonate. *Journal of Manufacturing Processes*. 2018, 35, 88-98.
- [7.2] Taki, K., Nakamura, S., Takayama, T., Nemoto, A., Ito, H. Direct joining of a laser-ablated metal surface and polymers by precise injection molding. *Microsystem Technologies*. 2016, 22(1), 31-38.
- [7.3] Lambiase, F., Paoletti, A. Mechanical behavior of AA5053/polyetheretherketone (PEEK) made by friction assisted joining. *Composite Structures*. 2018, 189, 70-78.
- [7.4] Lambiase, F., Paoletti, A., Grossi, V., Di Ilio, A. Friction assisted joining of aluminum and PVC sheets. *Journal of Manufacturing Processes*. 2017, 29, 221-231.
- [7.5] Lambiase, F., Paoletti, A. Friction assisted joining of titanium and polyetheretherketone (PEEK) sheets. *Thin-Walled Structures*. 2018, 130, 254-261.
- [7.6] Lambiase, F., Genna, S. Experimental analysis of laser assisted joining of Al-Mg aluminium alloy with polyetheretherketone (PEEK). *International Journal of Adhesion and Adhesives*. 2018, 84, 265-274.
- [7.7] Yeh, R. Y., Hsu, R. Q. Development of ultrasonic direct joining of thermoplastic to laser structured metal. *International Journal of Adhesion and Adhesives*. 2016, 65, 28-32.
- [7.8] Chen, Y. J., Yue, T. M., Guo, Z. N. A new laser joining technology for direct-bonding of metals and plastics. *Materials & Design*. 2016, 110, 775-781.
- [7.9] Yusof, F., Yukio, M., Yoshiharu, M., Shukor, M. H. A. Effect of anodizing on pulsed Nd: YAG laser joining of polyethylene terephthalate (PET) and aluminium alloy (A5052). *Materials & Design*. 2012, 37, 410-415.

[7.10] Lambiase, F., Genna, S. Laser-assisted direct joining of AISI304 stainless steel with polycarbonate sheets: thermal analysis, mechanical characterization, and bonds morphology. *Optics & Laser Technology*. 2017, 88, 205-214.

Appendix A. Preliminary experiments for producing the anchor layer on Al substrate

A.1. Introduction

In this chapter, preliminary experiments were carried out to additively fabricate the anchor layer, which has complex morphology, by laser-induced in-situ reaction. The effect of the process parameters (the size, molar ratio of power blend, laser power and laser scanning speed) on the morphology and microstructure of the anchor was investigated.

A.2. Experimental methods

A.2.1. Experimental procedure

The experimental process can be divided into powder blending and laser irradiation. The schematic illustration is shown in **Fig. 1.10**. Al, Ti and C powders were wet mixed with ethanol to fabricate powder mixtures. The powder mixture was bedded on an Al alloy substrate (A5052) in a rectangular form (15 mm × 5 mm). The height was decided depending on the powder size. A diode laser with pulsed mode was adopted on the powder mixture bedded on the Al substrate. The laser irradiation length was about 10 mm. Laser specification was same as that explained in section 3.2.1. Ultrasonic cleaning with water was carried out with the Al substrate for 1 min to remove unreacted powders. After the laser irradiation, the produced anchor layer was observed using a scanning electron microscopy (SEM). The cross-sectioning method for the anchor layer was same as that explained in 3.2.1.

The anchor layer was evaluated in terms of projected area fraction and adhesiveness between the anchor layer and Al substrate. The projected area fraction was evaluated using binarized top-view anchor layer image as shown in **Fig. A.1**. The adhesiveness between the anchor layer and Al substrate was evaluated qualitatively using cross-sectioned SEM image of the anchor layer. The presence of chemical compound at the interface between the anchor layer

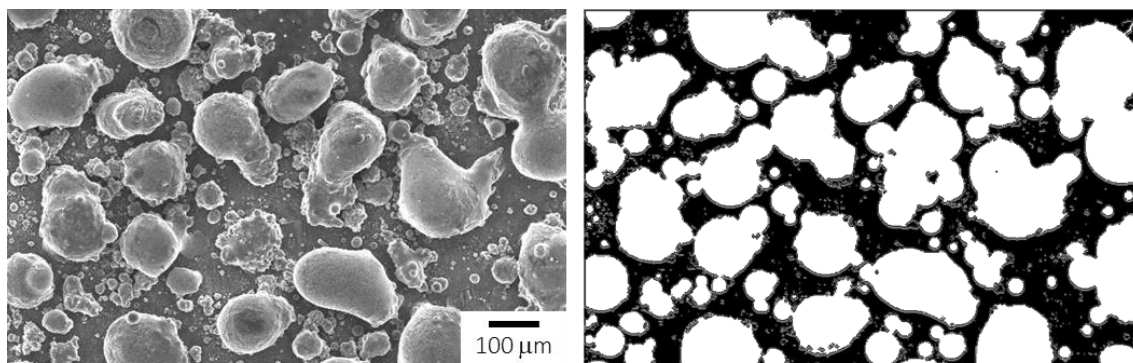


Fig. A.1 An example of SEM image showing a top-view of an anchor layer and its binarized image.

and Al substrate was also a criterion of the adhesiveness.

A.2.2. Experimental conditions

Numerous process conditions were applied to find the optimal condition for fabricating an appropriate anchor structure. Firstly, the effect of particle size of carbon powder on the anchor layer were investigated. Detailed conditions are summarized in **Table A.1**. Al powder ($< 45 \mu\text{m}$, purity 99.99%), Ti powder ($< 45 \mu\text{m}$, purity 99.9%), C powder ($< 5 \mu\text{m}$, purity 99.7%) and C powder ($\approx 5 \text{ nm}$, purity 98%) were used. These powders were weighed so that the molar ratio of Al:Ti:C was 1:1:1 and were wet mixed for 1 hour. The stack height of the bedded powder was about $100 \mu\text{m}$. Laser power and scan speed were controlled in the range of $200 \sim 400 \text{ W}$ and $30 \sim 70 \text{ mm/s}$. Several laser conditions were tested to find suitable conditions for producing the anchor layer.

The effect of Al molar ratio in the Al-Ti-C powder mixture on the anchor structure was investigated. Experimental conditions were summarized in **Table A.2**. Al powder ($< 45 \mu\text{m}$, purity 99.99%), Ti powder ($< 45 \mu\text{m}$, purity 99.9%), and C powder ($\approx 5 \text{ nm}$, purity 98%) were used. The powders were mixed for 1 hour so that the molar ratio Al:Ti:C was $x:1:1$ ($x = 0, 0.33, 1, 3, 5, \text{ and } \infty$). The $x = \infty$ means only the Al powder was used. The stack height of the bedded powder was about $100 \mu\text{m}$. Laser power and scan speed was controlled at 400 W and 40 mm/s , respectively.

The effect of laser scan speed on the anchor structure was investigated. Detailed experimental conditions are shown in **Table A.3**. Al powder ($< 45 \mu\text{m}$, purity 99.99%), Ti powder ($< 45 \mu\text{m}$, purity 99.9%), and C powder ($\approx 5 \text{ nm}$, purity 98%) were used. These powders were weighed so that the molar ratio of Al:Ti:C was 1:1:1 and were blended for 1 hour. The stack height of the bedded powder was about $100 \mu\text{m}$. Laser scan speed was controlled to be in the range of $10 \sim 100 \text{ mm/s}$ and laser power was 400 W .

The experimental conditions for investigating the effects of Al and Ti powder size on the anchor layer are summarized in **Table A.4**. Al powder ($< 45 \mu\text{m}$, $106\text{-}180 \mu\text{m}$, $425\text{-}850 \mu\text{m}$, 99.99 %), Ti powder ($< 45 \mu\text{m}$, $90\text{-}150 \mu\text{m}$, $250\text{-}600 \mu\text{m}$, 99.9 %), and C powder ($\approx 5 \text{ nm}$, purity 98%) were used. These powders were blended for 1 hours so that the molar ratio of Al:Ti:C was 1:1:1. The stack height of the bedded powder was basically set at about $500 \mu\text{m}$. However, when large size Ti powder ($250\text{-}600 \mu\text{m}$) were used, the stack height was raised to $600 \mu\text{m}$. Moreover, when the powder mixture included the large-sized Al powder ($425\text{-}850 \mu\text{m}$), the stack height was further increased to $850 \mu\text{m}$. Laser power and scan speed was fixed 400 W and 60 mm/s .

The effect of powder mixing time on the anchor layer was investigated. The experimental conditions are summarized in **Table A.5**. Al powder ($< 45 \mu\text{m}$, purity 99.99%), Ti powder ($< 45 \mu\text{m}$, purity 99.9%), and C powder ($\approx 5 \text{ nm}$, purity 98%) were used. These powders

were weighed so that the molar ratio of Al:Ti:C was 1:1:1 and mixed for 40, 50, and 60 min. The powder mixtures were observed with the SEM. The stack height of the bedded powder was about 500 μm . Laser power and scan speed was controlled at 400 W and 40 mm/s, respectively.

The experimental conditions and the numbers of figures showing corresponding results are summarized in **Table A.6**.

Table A.1 Experimental conditions for investigating the effect of powder size of C powder on the anchor structure.

	Powder condition			Laser condition		
	Al powder	Ti powder	C powder	Speed (mm/s)		
Size	< 45 μm	< 45 μm	< 5 μm ○ ≈ 5 nm ◎	30	50	70
Molar ratio	1	1	1	400	350	200
				○, ◎	○, ◎	○
				○	○	○
				○	○	○

Table A.2 Experimental conditions for investigating the effect of the composition in the powder mixture on the anchor structure.

	Powder condition			Laser condition	
	Al powder	Ti powder	C powder	Speed (mm/s)	Power (W)
Size	< 45 μm	< 45 μm	\approx 5 nm	40	400
Molar ratio	0				
	0.33				
	1	1	1		
	3				
	5				
	∞				

Table A.3 Experimental conditions for investigating the effect of laser scan speed on the anchor structure.

	Powder condition			Laser condition	
	Al powder	Ti powder	C powder	Speed (mm/s)	Power (W)
Size	< 45 μm	< 45 μm	\approx 5 nm	10	
Molar ratio	1	1	1	20	
				40	400
				60	
				80	
				100	

Table A.4 Experimental conditions for investigating the effects of particle of Al and Ti powders sizes on the anchor structure.

	Powder condition			Laser condition	
	Al powder	Ti powder	C powder	Speed (mm/s)	Power (W)
Size	< 45 μm	<45 μm	\approx 5 nm	40	400
		90-150 μm		60	
		250-600 μm			
	106-180 μm	<45 μm			
		90-150 μm			
		250-600 μm			
425-850 μm	<45 μm				
	90-150 μm				
	250-600 μm				
Molar ratio	1	1	1		

Table A.5 Experimental conditions for investigating the effect of powder mixing time on the anchor structure.

	Powder condition				Laser condition	
	Al powder	Ti powder	C powder	Mixing time (min)	Speed (mm/s)	Power (W)
Size	< 45 μm	< 45 μm	\approx 5 nm	40, 50, 60	40	400
Molar ratio	1	1	1			

Table A.6 Lists of experimental conditions and the numbers of figures showing corresponding results

Experimental condition table	Result figures
A.1	A.2 ~ A.3
A.2	A.4 ~ A.5
A.3	A.6 ~ A.9
A.4	A.10 ~ A.12
A.5	A.13

A.3. Results

A.3.1. Effect of particle size of C powder

The representative SEM images showing the top-view of the anchor layer produced from the powder mixtures with different laser parameters and C powders are shown in **Fig. A.2**. In the case of C powder with the size of $< 5 \mu\text{m}$, the products elongated perpendicular to the laser scanning direction were generated periodically. The amount of the products increased with an increase in the laser power and decrease in the laser scan speed. When the laser power was 200 W, the anchor layer was only produced with the laser speed of 30 mm/s. In the case of the laser power of 350 W, the anchor layer was produced with the laser speed of 30 and 50 mm/s. The anchor layer was formed at all laser speed when the laser power was 400 W.

A number of granular products were formed on the Al substrate when the nano-sized C powder was used. The size of the products was significantly smaller than that of the products when the micro-sized C powder was used. The size of the granular products obtained under the laser scan speed of 30 mm/s was larger compare to 50 mm/s. Obviously, the anchor layer indicated more complex morphology when the nano-sized C powder was used.

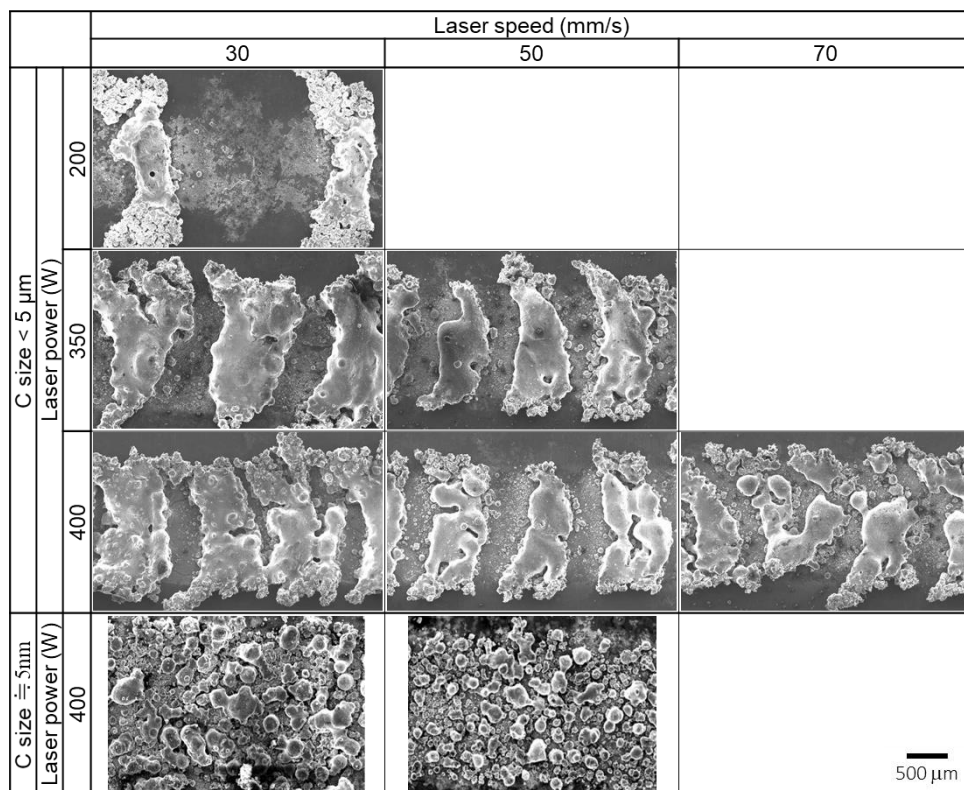


Fig. A.2 SEM images showing the top-view of the anchor layers fabricated from the powder mixture with different particle size C powder under different laser power and scan speeds.

The SEM image of the cross-sectioned anchor layer are shown in **Fig. A.3** It was confirmed that the anchor layers indicated protrusive morphology at all the conditions because the anchor layers were formed on the Al substrate. It was indicated that the anchor layer which was fabricated with nano-sized C powder was beneficial for obtain more complex structured anchor layer with better adhesiveness with the Al substrate. It seems that the laser power of 400 W was suitable to produce the anchor layer.

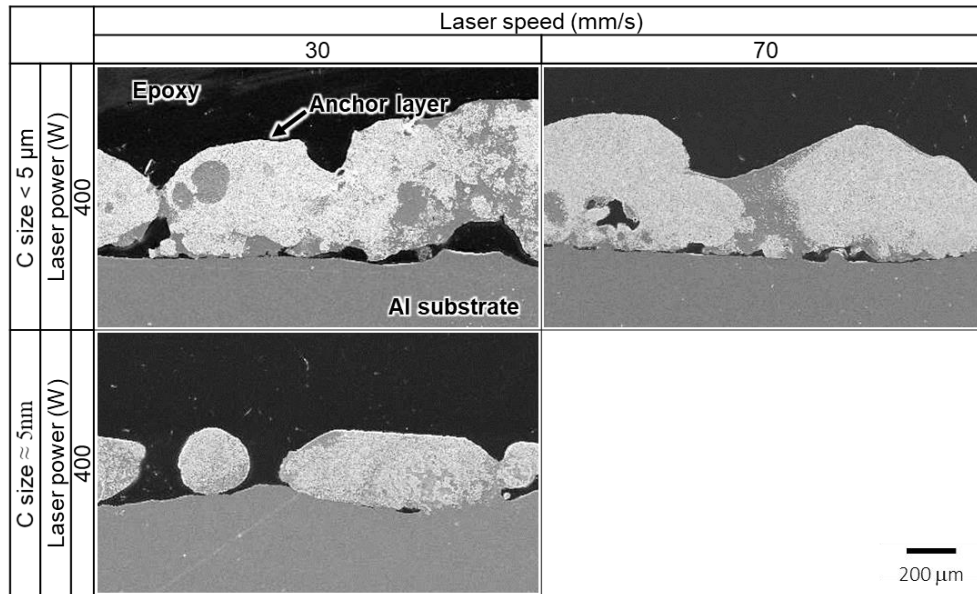


Fig. A.3 SEM images of the cross-sectioned anchor layer formed with different laser parameters and C powder type.

A.3.2. Effect of Al molar ratio

Figure A.4 shows the representative SEM images of the top-view and cross-sectioned anchor layer produced from the powder mixtures with different Al molar ratio (x). The anchor layers consisted of granular protrusions. It was observed that granular protrusions were homogeneously distributed in laser-irradiated region except when only Al powder ($x = \infty$) was used. The size of the granular protrusions increased with an increase in the Al molar ratio. The projected area fraction of each anchor layer formed with different powder molar ratio is quantitatively measured and shown in **Fig. A.5**. The projected area fraction was the lowest when the Ti-C powder mixture ($x = 0$) was used. The projected area fraction of the anchor layer increased from about 37 to 72% with an increase in the Al molar ratio from 0 to 1.0 and decreased when the Al molar ratio was larger than 1.0.

The cross-sectioned images indicated that the granular protrusions and Al substrate indicated good adhesiveness when x was 0, 0.33, 1, and ∞ . When the only Al powder ($x = \infty$) was used, the interface between the anchor layer and Al substrate was hardly recognized. It

seemed that the molar ratio of Al power of 1.0 was the most suitable condition because the anchor layer had both high projected area fraction and good adhesiveness with the Al substrate.

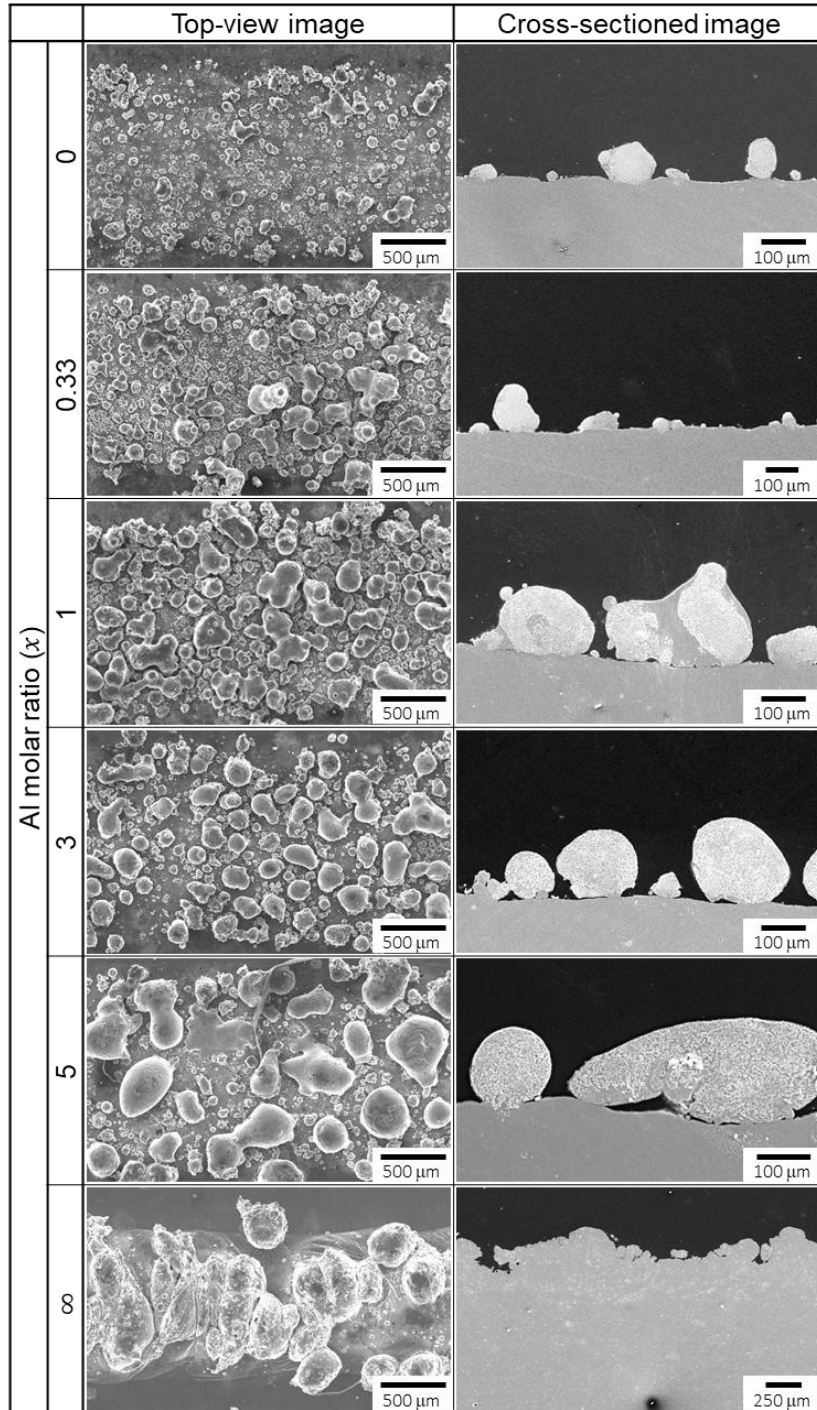


Fig. A.4 SEM images showing the top-view and cross-section of the anchor layers fabricate from the powder mixtures with different Al molar ratio.

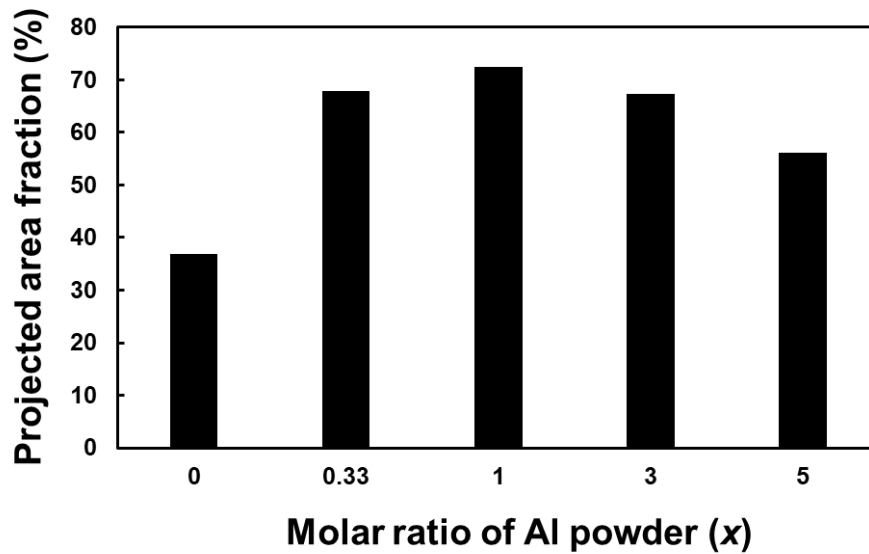


Fig. A.5 Projected area fractions of the anchor layers fabricated from the powder mixtures with different Al molar ratio (x).

A.3.3. Effect of laser speed

The representative SEM images showing the top-view of the anchor layer were indicated in **Fig. A.6**. It was observed that the size of the protrusions decreased with an increase in the laser speed. When the scanning speeds were 10 and 20 mm/s, the granular protrusions were connected each other, and large. The Al substrate was cracked under the laser speed of 10 and 20 mm/s because of very high energy input. A number of granular protrusions were produced and homogeneously distributed on the laser irradiated region under the laser scan speed of 40 to 100

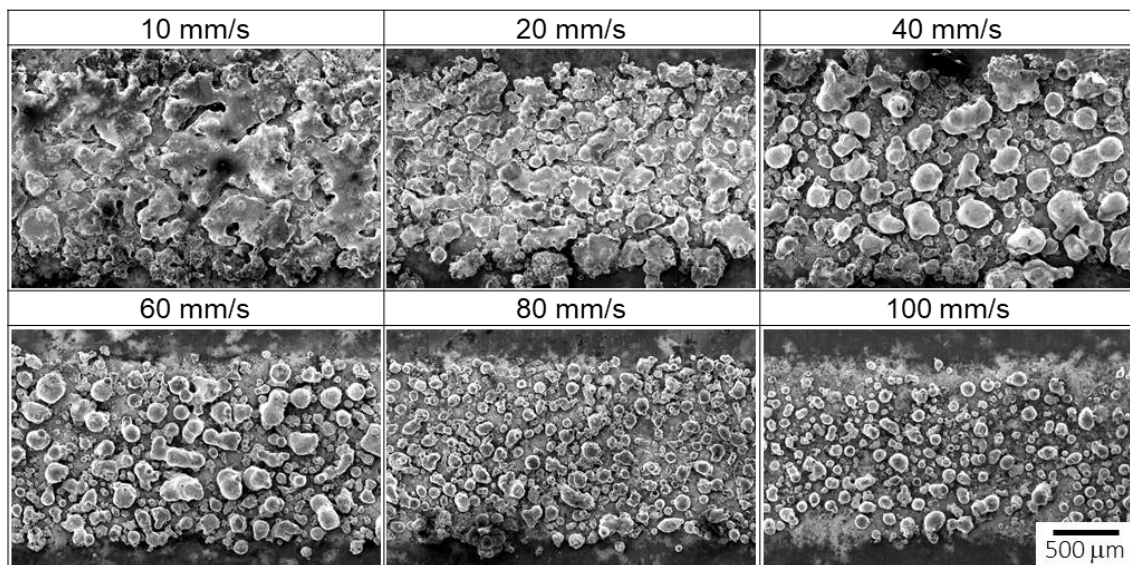


Fig. A.6 SEM images showing the top-view of anchor layers formed under different laser scan speeds.

mm/s. The projected area fraction of the anchor layer under the laser scan speed of 40 to 100 mm/s was obtained and summarized in **Fig. A.7**. The projected area fraction did not change much even when the laser scan speed increased from 40 to 60 mm/s. Above the laser scan speed of 60 mm/s, the projected area fraction decreased with increasing the laser scan speed.

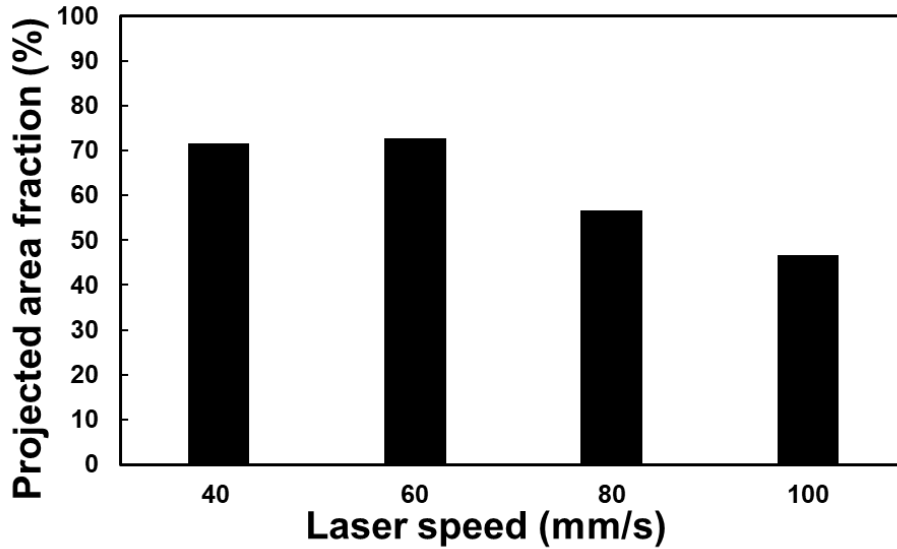


Fig. A.7 Projected area fraction of anchor layer formed under different laser scan speeds.

The SEM images for the cross-sectioned anchor layer are shown in **Fig. A.8**. When the laser speed was 20 mm/s, the granular protrusions were intimately bonded with the Al substrate. The granular protrusions were observed under the laser scan speed of 40 to 100 mm/s. The adhesiveness between the anchor layer and Al substrate was improved with a decrease in the laser

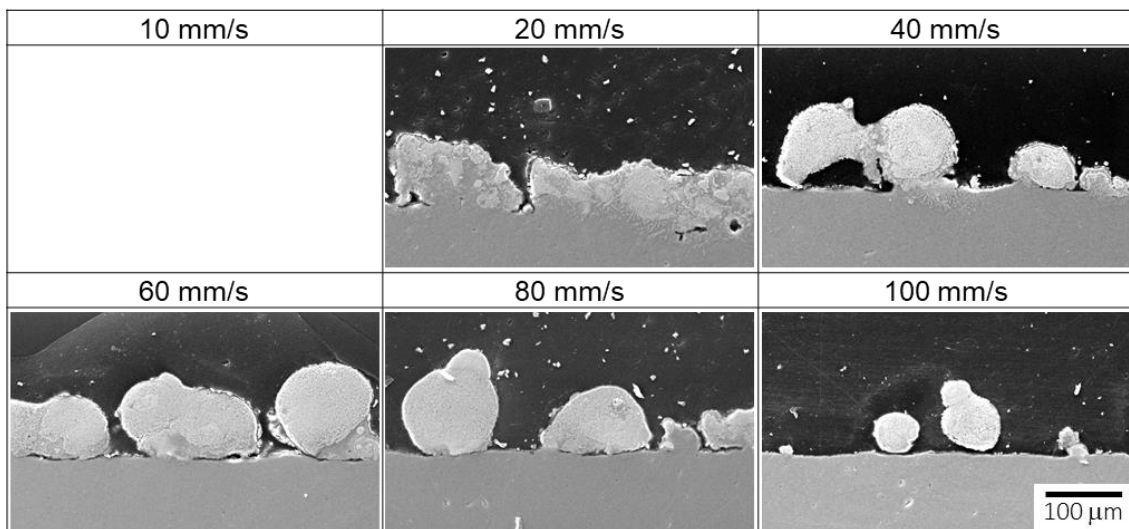


Fig. A.8 SEM images of the cross-sectioned anchor layer formed under different laser scan speeds.

scan speed. The adhesiveness between the granular protrusions and Al substrate is very poor under the laser speed of 100 mm/s.

The magnified SEM images of the cross-sectioned anchor layer fabricated under a laser scan speed of 60 and 40 mm/s are shown in **Fig. A.9 (a)** and **(b)**, respectively. The phase with brighter contrast exhibited a particle morphology. The phase identification will be described in the chapter 4.

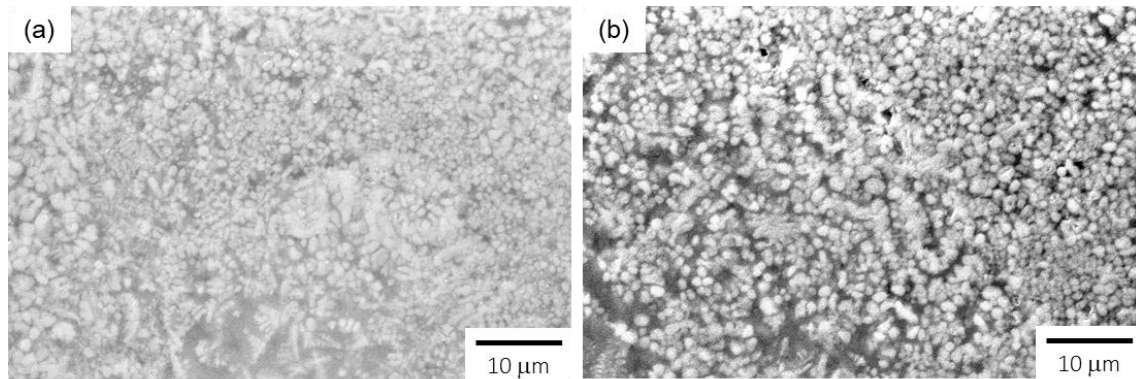


Fig. A.9 High magnification SEM image of the cross-sectioned granular protrusion formed with laser speed of (a) 60 mm/s and (b) 40 mm/s.

A.3.4. Effect of particle sizes of Al and Ti powders

Figure A.10 shows the SEM images showing the top-view of the anchor layer fabricated from the powder mixtures with different Al and Ti particle sizes under the laser scan speed of 60 mm/s. It was observed that granular or spreading form of protrusions were produced on the Al substrate from most conditions. When the powder mixture was fabricated with the Al powder (425 - 805 μm) and Ti powder (< 45 μm and 90 - 150 μm), the molten powder spread on the Al substrate rather than producing granular protrusions. Huge size of granular protrusions was generated when the Al powder (425 - 805 μm) and Ti powder (250 - 600 μm) were used, while the number of the granular protrusion was small. It seemed that the Al powder size of < 180 μm is suitable for fabricating the anchor layer judged by the top-view anchor layer, although the Al-Ti-C powder using the Al powder size of 180 ~ 425 μm needs to be investigated. **Figure A.11** shows the cross-sectioned anchor layer fabricated with various powder size under the laser speed of 60 mm/s. It is observed that the height of protrusions increased when the particle size of Al powder increased from 45 μm to 106-180 μm and did not change when the particle size of Al powder increased from 106-180 μm to 425-850 μm . The protrusions spread with increasing the particle size of Al powder. The particle size of Ti powder slightly affected the morphology of protrusions. The adhesiveness between the anchor layer and Al substrate was improved largely with increasing the particle size of Al powder. Most of the

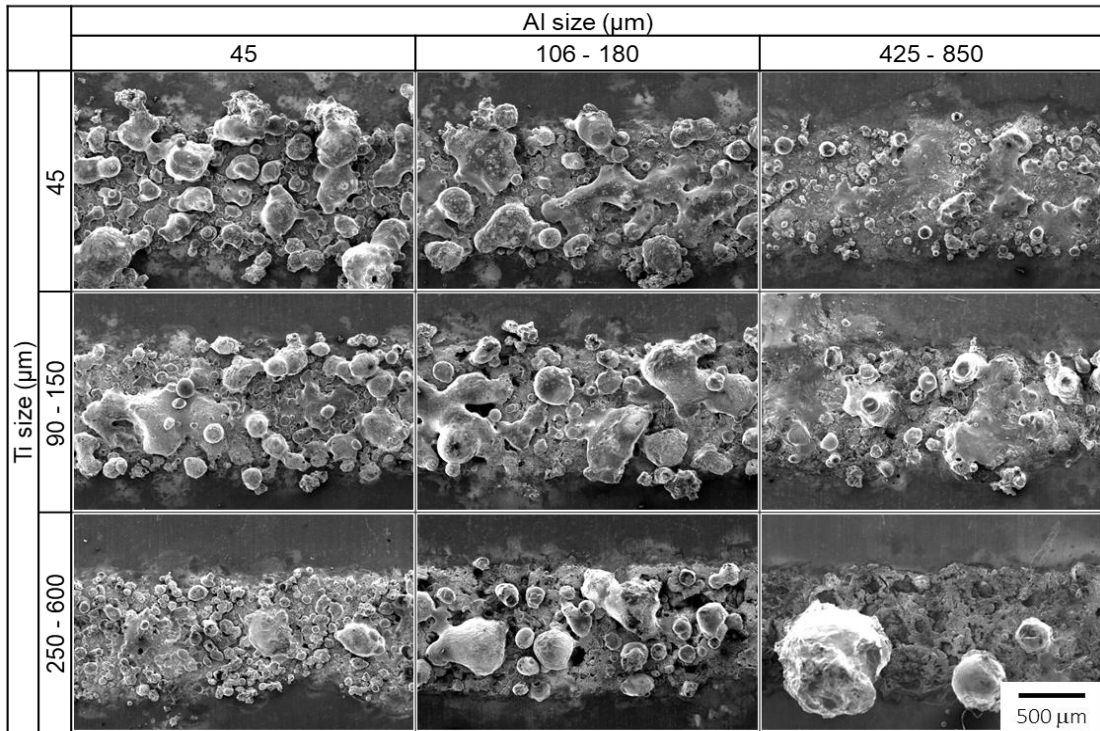


Fig. A.10 SEM images showing the top-view of anchor layers fabricated from the powder mixtures with various particle sizes of Al and Ti powders.

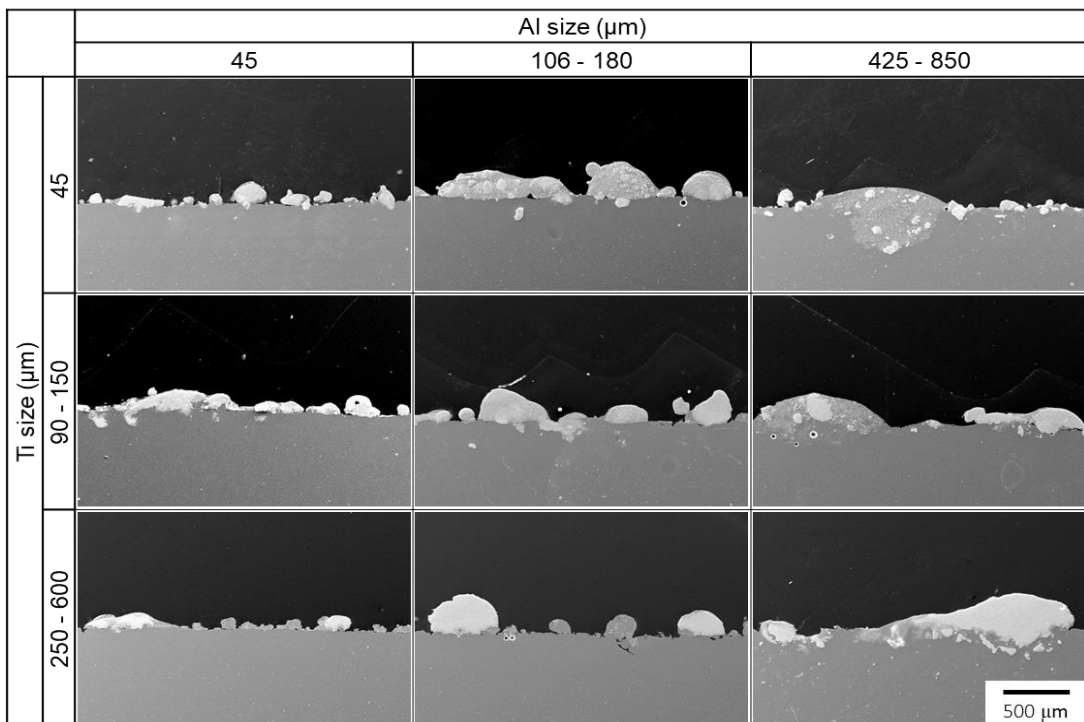


Fig. A.11 SEM images showing the top-view of anchor layers fabricated from the powder mixtures with various particle sizes of Al and Ti powders.

protrusions were filled with a phase of brighter contrast. The brighter contrast phase was found below the interface between the granular protrusions and Al substrate except for the anchor layer fabricated from powder mixtures consisting of with Al powder with particle sizes of $< 45 \mu\text{m}$, $106 - 180 \mu\text{m}$ and Ti powder with a particle size of $250 - 600 \mu\text{m}$. **Figure A.12** shows the magnified SEM image of the anchor layer fabricated from the powder mixture consisting of the Ti powder with a particle size of $< 45 \mu\text{m}$ and Al powder with a particle size of $106 - 180 \mu\text{m}$. Considering the number of granular protrusions and adhesiveness, the anchor layer fabricated with the Al powder ($< 180 \mu\text{m}$) and the Ti powder ($< 150 \mu\text{m}$) was suitable. The Al-Ti-C powder mixture using the Al powder size of $180 \sim 425 \mu\text{m}$ and the Ti powder size of $150 \sim 250 \mu\text{m}$ needs to be investigated

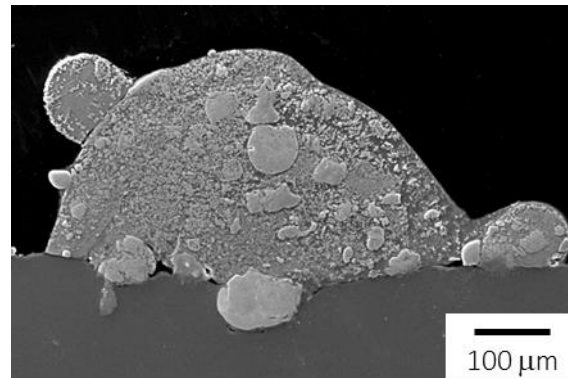


Fig. A.12 The magnified SEM image showing cross-sectioned anchor layer fabricated from the powder mixtures consisting of Al ($106-180 \mu\text{m}$) and Ti ($<45 \mu\text{m}$) powders.

A.3.5. Effect of powder mixing time

Figure A.13 shows SEM images of the powder mixtures and corresponding anchor layer fabricated from the powder mixtures. The powders were aggregated at a shorter mixing time and uniformly dispersed with increasing the mixing time. Some aggregated powders more than $500 \mu\text{m}$ in size after wet mixing for 40 minutes were observed. The aggregated powder after wet mixing for 50 minutes was about $300 \mu\text{m}$ or less. When the mixing time was 60 min, the powder mixture was very fine. In the case of the power mixture blended for 40 and 50 min, granular protrusions had large size and ununiformly distributed on the Al substrate. When the power mixing time was 60 min, granular protrusions with uniform size was distributed uniformly. Thus, the powder mixing time longer than 60 min is preferable for fabricating the anchor layer with a uniform structure.

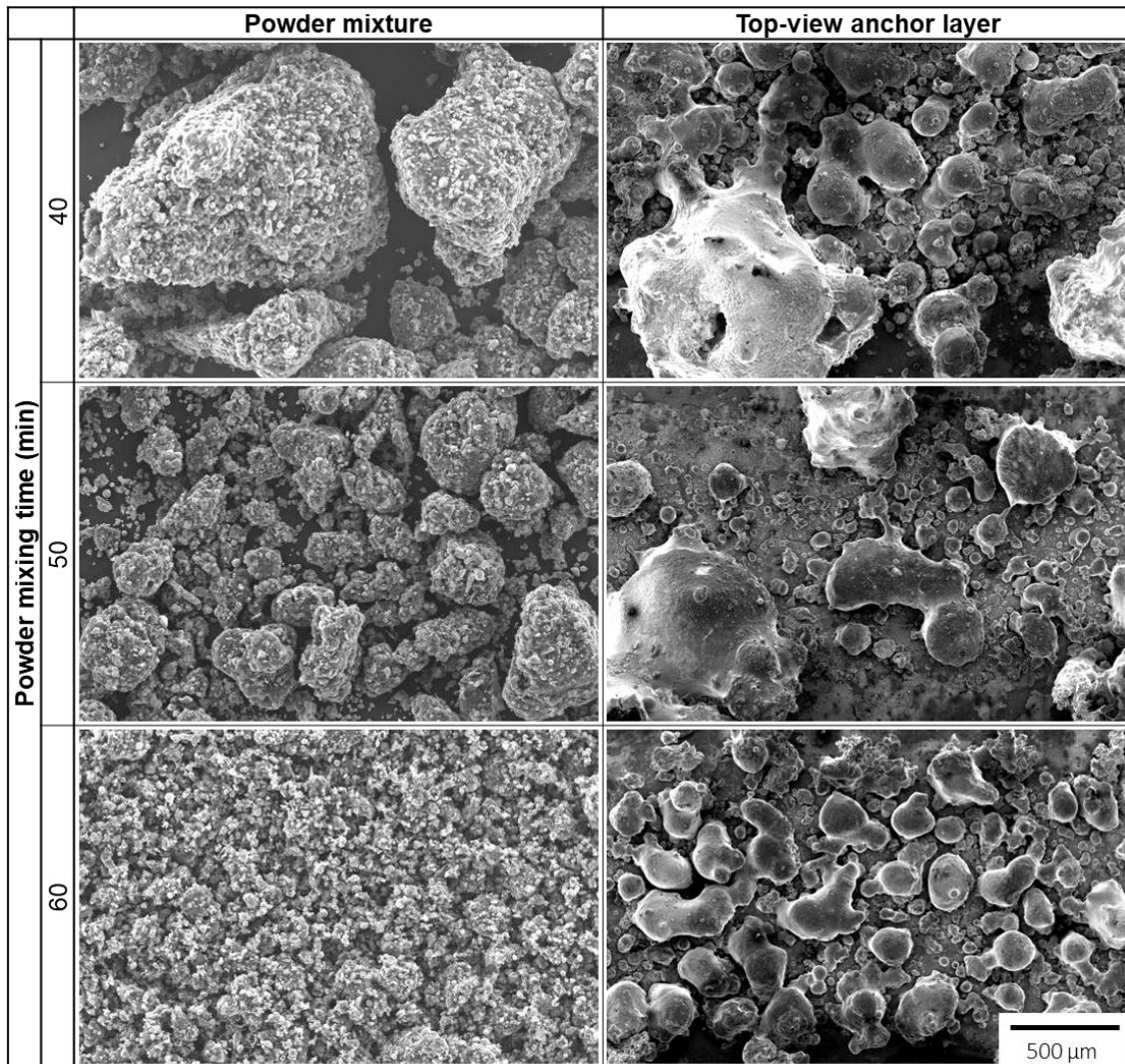


Fig. A.13 SEM images showing powder mixture blended for 40, 50, and 60 min and top-view of anchor layers fabricated from the powder mixtures.

A.4. Summary

Preliminary experiments were carried out in this chapter to additively fabricate the anchor layer on the Al substrate by laser-induced in-situ reaction. Various process parameters were considered, and the followings are main results.

- The use of nano-sized C powder in Al-Ti-C powder mixture was effective for fabricating the anchor layer which has complex morphology and good adhesiveness with the Al substrate.
- The molar ratio of Al-Ti-C powder of 1:1:1 was suitable for fabricating the anchor layer consisting of many granular protrusions well-bonded with the Al substrate.

- The size of the granular products increased with a decrease in the laser scan speed. The adhesiveness between the anchor layer and Al substrate increased with a decrease in the laser speed. It was found that the Al substrate was damaged under the low scan laser speed conditions.
- When large-sized Al powder was used, the adhesiveness between the granular protrusion and Al substrate was improved, while the number of granular products decreased. The use of large-sized Al powder increased the height of protrusions. The particle size of Ti powder slightly affected the anchor structure.
- The powder mixing time longer than 60 min was preferable for fabricating the anchor layer consisting of uniformly distributed granular products.

Appendix B. Non-equilibrium solidification – Scheil solidification

Scheil solidification is a model to explain partitioning of a solute in liquid and solid phases and fraction of solid phases after the solidification of alloys under non-equilibrium condition (fast cooling condition). Scheil solidification assumes no diffusion in the solid phase, complete mixing of elements in the liquid phase (infinite mixing speed), and equilibrium at the liquid-solid interface.

Figure B.1 shows schematic illustration of equilibrium phase diagrams of A-B eutectic system (left) and the microstructures (right) at various temperatures during solidification [B.1]. The solidification route is indicated on the phase diagrams by the black arrows. Consider an alloy with a composition of C_0 is given and being cooled from a liquid phase (**Fig. B.1 (a)**). When the temperature reaches T_1 , which is just below the liquidus line, an α -phase nucleus forms with the composition of $C_{S,1}$ in the liquid phase. The composition of the liquid phase is instantly determined to $C_{L,1}$ because of the assumption of complete mixing in the liquid phase. When the temperature reaches T_2 , the α -phase with the composition of $C_{S,2}$ is formed around the previously formed α -phase ($C_{S,1}$) (**Fig. B.1 (b)**). The composition of the liquid phase instantly becomes $C_{L,2}$. At the temperature of T_3 , the α -phase with composition of $C_{S,3}$ is formed around the previously formed α -phase (**Fig. B.1 (c)**). The composition of the liquid phase instantly becomes $C_{L,3}$. The above-mentioned processes are repeated. When the temperature reaches T_E (Eutectic temperature), the compositions of the α -phase and liquid phase will finally reach $C_{S,E}$ and $C_{L,E}$ (eutectic point), respectively. The microstructure of grains of α -phase will indicate gradient composition since no diffusion in the solid phase is assumed.

The derivation of the Scheil equation is shown as follows [B.2]. The alloy melt with the initial concentration of C_0 is being cooled down. When the temperature of the system reaches T_1 , which is just below the liquidus line, the primary α phase with the composition of $C_{S,1}$ formed in the liquid phase (**Fig. B.2 (a)**). The composition of the liquid phase is instantly determined to $C_{L,1}$. The compositions of liquid and solid phases increase as the solute is partitioned into both phases since the newly formed solid phase was generated from a more concentrated liquid phase. At the temperature of T_n , the volume fraction of solid phase becomes V_S and the compositions of the newly formed solid and liquid phases are C_S and C_L , respectively (**Fig. B.2 (b)**). Consider the temperature slightly decreases and the volume fraction of the solid phase increases dV_S . The solute partitioned into the liquid phase can be expressed as follow.

$$C_L \cdot dV_S - C_S \cdot dV_S \quad (\text{B.1})$$

where $C_L \cdot dV_S$ represents the solute contained in the liquid phase in the volume of dV_S before the solidification and $C_S \cdot dV_S$ represents the solute partitioned into the newly formed solid phase. The Eq. (B.1) can be written

$$(C_L - C_S)dV_S \quad (B.2)$$

Consider the composition of the liquid phase increases dC_L , the solute partitioned into the liquid phase can be also expressed as follow.

$$(1 - V_S)dC_L \quad (B.3)$$

The amount of partitioned solute must be same. Therefore, Eq. (B.2) and (B.3) are same.

$$(C_L - C_S)dV_S = (1 - V_S)dC_L \quad (B.4)$$

The Eq. (B.4) represents the gray areas in the figure are same. A partitioning coefficient (k) is defined as

$$k = C_S/C_L$$

Then, the Eq. (B.4) can be written

$$(1 - k)C_L dV_S = (1 - V_S)dC_L$$

Separation of variables is used to solve this differential equation.

$$\frac{1}{(1-V_S)} dV_S = \frac{1}{C_L(1-k)} dC_L$$

If we solve the following integration

$$\int_0^{V_S} \frac{1}{(1-V_S)} dV_S = \frac{1}{(1-k)} \int_{C_0}^{C_L} \frac{1}{C_L} dC_L$$

The composition of the solid phase is obtained as follow.

$$C_S = kC_0(1 - V_S)^{k-1} \quad (B.5)$$

The Eq. (B.5) is called as Scheil equation. The equation says C_S diverges infinitely with increasing V_S since k is less than 1, whereas C_S must have an upper limit. In the case of the eutectic system, $C_{S,E}$ is the upper limit as indicated in **Fig. B.1 (c)**. Change in C_S as a function of V_S is shown in **Fig. B.2 (c)**. When the temperature reaches T_E (eutectic temperature), the solid phase with the composition of $C_{S,E}$ is formed, and the eutectic reaction is occurred in the liquid phase.

References

- [B.1] Warczok, P. Performing Scheil-Gulliver (SG) analysis in MatCalc. https://www.matcalc-engineering.com/images/external/PDF-Files/scheil_gulliver.pdf, (accessed 2020-6-25).
- [B.2] The Scheil Equation. Dissemination of IT for the Promotion of Materials Science (DoITPoMS). https://www.doitpoms.ac.uk/tlplib/solidification_alloys/scheil.php, (accessed 2020-6-25).

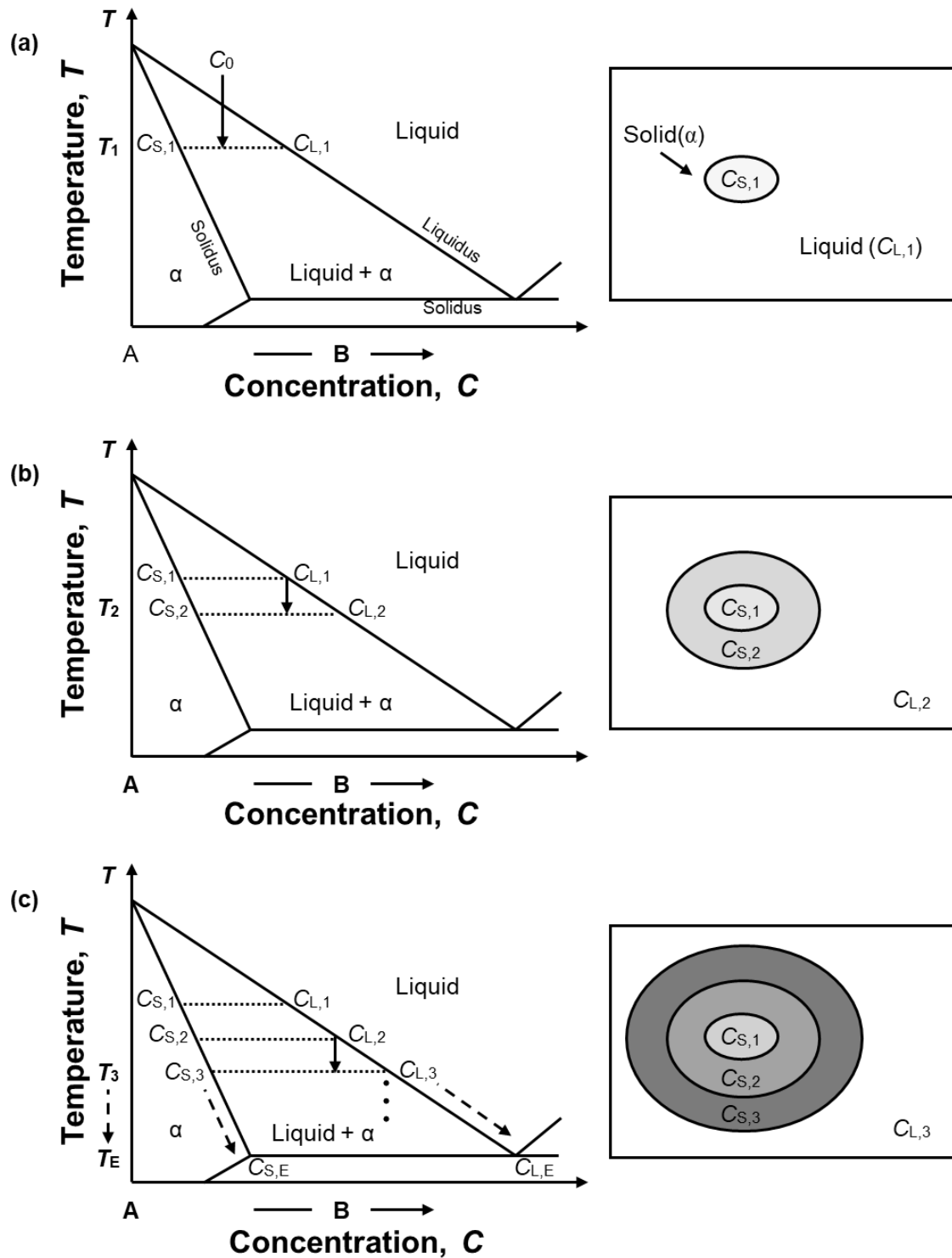


Fig. B.1 Schematic illustrations of a solidification route on phase diagrams (left) and the corresponding microstructure evolution (right) during the solidification process at (a) T_1 , (b) T_2 , and (c) T_3 under non-equilibrium condition [B.1].

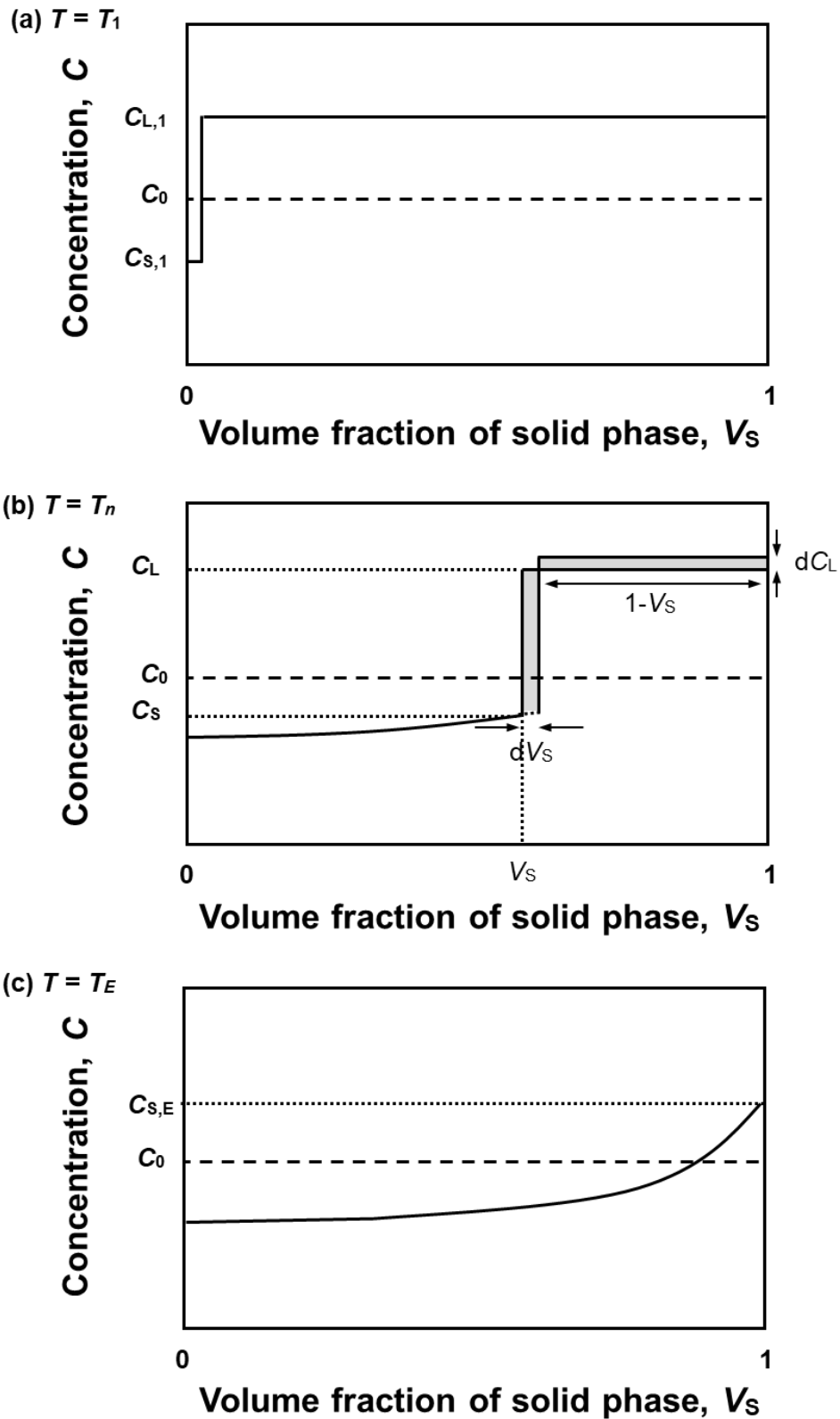


Fig. B.2 Schematic illustrations of concentration profiles of solid and liquid phases during a solidification process at (a) T_1 , (b) T_n , and (c) T_E under non-equilibrium condition [B.2].

【Articles related to this research and related chapters】

1. Journals

1. “Joining of metals and polymers using powder metallurgy with laser irradiation” Chapter 3
Seung-Gwang Kim, Asuka Suzuki, Naoki Takata, and Makoto Kobashi, *Journal of Materials Processing Technology*, 270 (2019), 1-7.
2. “Effect of hot-press thermal history on joint strength of A5052/Polyamide-6 hybrid structure via a porous layer” Chapter 4
Seung-Gwang Kim, Asuka Suzuki, Naoki Takata, and Makoto Kobashi, *Journal of Materials Processing Technology*, 276 (2020), 116388.
3. “Interfacial structural control of Al/polymer hybrid structure via a porous layer for enhancing the joint strength” Chapter 5
Seung-Gwang Kim, Asuka Suzuki, Naoki Takata, and Makoto Kobashi, *Journal of Materials Processing Technology* (Under review).

2. International conferences

1. “Fabrication and structure control of porous anchor layer on Al alloy substrate for PA6-Al hybrid joint using laser-induced combustion synthesis” Chapter 3
Seung-Gwang Kim, Asuka Suzuki, Naoki Takata, and Makoto Kobashi, 9th NTTH joint symposium, 13 July 2017
2. “Direct joining between metal and polymer using protruding anchor layer fabricated by laser-induced combustion synthesis” Chapter 3
Seung-Gwang Kim, Asuka Suzuki, Naoki Takata, and Makoto Kobashi, 60th JSPM International Conference on Powder and Powder Metallurgy, P-A5-01, 7 November 2017
3. “Microstructure characteristic of protruding anchor layer fabricated by laser-induced combustion synthesis reaction of Al-Ti-C System” Chapter 3
Seung-Gwang Kim, Asuka Suzuki, Naoki Takata, and Makoto Kobashi, 16th International Conference on Aluminum Alloys, 398834, 19 June 2018
4. “Effect of joining temperature history on lap shear strength of directly joined A5052/Polyamide-6 via porous layer” Chapter 4
Seung-Gwang Kim, Asuka Suzuki, Naoki Takata, and Makoto Kobashi, 14th International Aluminium Conference, O7-1, 13 November 2019

【Acknowledgements】

Foremost, I deeply grateful to my academic advisor Prof. Makoto Kobashi for his continuous supports, enthusiasm and patience. I also owe very important debt to Assoc. Prof. Naoki Takata and Asst. Prof. Asuka Suzuki whose guidance and advice were invaluable for my research and writing of Ph.D. thesis. Insightful comments and hard questions given by my thesis committee, Prof. Noritaka Usami, Assoc. Prof. Takashi Itoh, and Dr. Naoki Omura (AIST), have been a great help in completing my thesis.

My sincere gratitude also goes to Mr. Tomohiro Maeda for offering to use the experiment devices in his company. I can hardly imagine completing my research without his supports.

I appreciate my lab members, Mr. Kenta Kurumatani, Mr. Rui Katou, and Mr. Keiichiro Iwata for the constructive discussions and for all the time we have had. I cannot forget the time we were working together. Also, I thank competent secretaries, Kazuko Nomura and Yoko Mizuno for their tremendous support.

Lastly, I would like to express the deepest appreciation to my family for their patience and supporting me spiritually throughout my life.